Remote Sensing Laboratories – RSL
Department of Geography, University of Zurich, Switzerland

GEO 511 – Master Thesis

Relating Snow Wetness Information Gained from the Intercantonal Measurement and Information System Stations in Switzerland to Envisat ASAR Backscatter

30 September 2014

submitted by

Christoph Rohner
08-735-268

Supervised by

Dr. David Small
Remote Sensing Laboratories – RSL
Department of Geography
University of Zurich
Winterthurerstrasse 190
8057 Zurich
david.small@geo.uzh.ch

Dr. Tobias Jonas
WSL Institute for Snow and Avalanche Research SLF
Flüelastrasse 11
7260 Davos Dorf
jonas@slf.ch

Faculty member
Prof. Dr. Michael Schaepman

Summary

As seasonal snow is an important parameter in the hydrological cycle of mountainous regions, information about snow cover distribution and the snow's state can be used for flood forecasting and the management of lakes and reservoirs. To determine the spatially highly variable snow covered area, a high spatial and temporal resolution is required, for which remote sensing offers an ideal tool. With several studies showing the feasibility of wet snow detection using C-band Synthetic Aperture Radar (SAR) and swath widths of about 400 km, Envisat ASAR and RADARSAT-2 offer the possibility to image all of Switzerland in a single scene with high temporal and spatial resolutions. This thesis aims to investigate the accuracy of the wet snow detection in mountainous terrain using a local resolution weighting method as well as analyze the sensitivity of the SAR backscatter on the melting process.

The thesis was based on a total of 330 co-polarized Envisat ASAR C-band (5.331 GHz) images between 2007 and 2012 with a pixel spacing of 100 m and four co-/cross-polarized RADARSAT-2 C-band (5.405 GHz) scenes from 2010 and 2012, respectively, with a pixel spacing of 25 m. Based on the radiometrically terrain corrected scenes from both sensors, composite images were calculated using the local resolution weighting (LRW) approach to improve the local resolution in areas with foreshortening, shadowing, or layover. By applying a wet snow detection algorithm based on the backscatter differences between dry and wet snow conditions, it was possible to determine the areas covered by wet snow. These results were compared with ground reference data provided by the WSL Institute for Snow and Avalanche Research SLF, consisting of hourly measured/modeled snow and meteorological parameters for 114 stations of the Intercantonal Measurement and Information System (IMIS), distributed throughout the Swiss Alps as well as snow cover products from optical sensors.

The correspondence between the optical snow cover extent data sets and the SAR LRW composites was carried out on a pixel-by-pixel basis and showed high user's accuracy values. This thesis highlights the importance of a small temporal lag between the SAR scenes included in an LRW composite and demonstrates the additional gain in accuracy when integrating different orbit configurations. The classification results were further assessed regarding the influence of external factors on the accuracy of the wet snow detection. Furthermore, the sensitivity of the SAR backscatter on the melting process was analyzed using layered liquid water volume information calculated for IMIS station locations. The statistical analysis showed a negative – albeit moderate – correlation for all different integration depths of wet snow layers investigated, indicating a small sensitivity for the total liquid water volume of the snow pack.

Contents

List of Figures

List of Tables

List of Abbreviations

ASAR Advanced Synthetic Aperture Radar

AVHRR Advanced Very High Resolution Radiometer

CoReH$_2$O Cold Regions Hydrology High-resolution Observatory

CORINE Coordination of Information on the Environment

CSA Canadian Space Agency

DEM Digital Elevation Model

DN Digital Number

ERS European Remote Sensing Satellite

ESA European Space Agency

FSC Fractional Snow Cover

GTC Geocoded Terrain Corrected

IMIS Intercantonal Measurement and Information System

LIDAR Light Detection And Ranging

LIM Local Incidence Angle Mask

LRW Local Resolution Weighting

LS 7 Landsat 7

LWC Liquid Water Content

LWV Liquid Water Volume

MeteoSwiss Federal Office of Meteorology and Climatology

MODIS Moderate-Resolution Imaging Spectroradiometer

NDSI Normalized Difference Snow Index

OSHD Operational Snow-hydrological Service

RS-2 RADARSAT-2

RSL Remote Sensing Laboratory

RTC Radiometrically Terrain Corrected

SAR Synthetic Aperture Radar

SCF Slope Correction Factor

SLF WSL Institute for Snow and Avalanche Research

SWE Snow Water Equivalent

swisstopo Federal Office of Topography

WSM Wide Swath Mode

1. Introduction

As snow constitutes an important part of the hydrological cycle in mountainous regions, knowledge of the distribution, state, and water content of seasonal snow cover is not only of importance for avalanche warning, but also for flood forecasting and the management of lakes and reservoirs. As a result of the spatial variability of snow, information with a high spatial and temporal resolution are required. In Switzerland, the WSL Institute for Snow and Avalanche Research (SLF) operates the Intercantonal Measurement and Information System (IMIS), consisting of more than 100 automated measurement stations throughout the Swiss Alps providing information regarding meteorological as well as snow parameters (Jonas, 2012; Lehning et al., 1999). The data from these measurement stations is used for avalanche and flood forecasting by SLF's avalanche warning service and Operational Snow-hydrological Service (OSHD) (Jonas, 2012; Swiss Federal Institute for Forest, Snow and Landscape Research, 2013). These point measurements are not able to fully represent the spatial distribution and properties of snow. Remotely sensed data – from both optical and SAR systems – offer improved robustness and opens up new applications (Bernier, 1991). A relatively small number of SAR systems were active as in July 2014. The SAR approach offers all-weather and day/night imaging capabilities (Curlander & McDonough, 1991). In addition, the incident electromagnetic waves of SAR systems penetrate into the surface and interact with the subsurface snow, primarily governed by the radar wavelength and the snow's properties (Stiles & Ulaby, 1981). It is therefore of interest for flood forecasting and water management to know more about the usability of remotely sensed data as a source of information regarding the distribution, state, and water content of seasonal snow cover.

As SAR is highly responsive to liquid water within the snow pack, scientific investigations regarding its potential for wet snow cover monitoring date back as far as 1980 (Rees, 2006) and has since been described by a variety of authors (e.g. Mätzler, 1987; Bernier, 1991; Fily et al., 1995). But while wet snow cover monitoring works well for flat terrain such as Québec (Canada) (Bernier, 1991; Baghdadi et al., 1997), geometric distortions such as foreshortening and layover proved to be a challenge using SAR for snow cover monitoring in mountainous areas, until the introduction of a new radiometric correction algorithm by Small et al. (2010).

In contrast to the wet snow cover detection, retrieval of snow parameters such as Liquid Water Content (LWC) or Snow Water Equivalent (SWE) are a bigger challenge. They would have even greater utility to snow-hydrological applications. Early work was carried out by Shi et al. (1993) using airborne C-band SAR with two polarizations (VV/HH) to retrieve the LWC of the snow pack, while later works combined dual-polarization C-band SAR data with a meteorological model (Longépé et al., 2009). But since these techniques cannot be trivially applied on a large scale as they need a-priori information, passive microwave radiometry remains the only spaceborne technique with proven ability to extract SWE data, although at a coarse resolution of 25 km (Rees, 2006; König et al., 2001; Rott et al., 2010, 2011; Luojus et al., 2009). In recent

years, a new approach using multi-frequency and multi-polarization SAR sensors such as the Cold Regions Hydrology High-resolution Observatory ($CoReH_2O$) was proposed, using the differences in signal attenuation between the X- and Ku-band as well as between polarizations (Rott et al., 2010, 2012b). However, as the $CoReH_2O$ mission was not selected by European Space Agency (ESA), the lack of large scale information regarding operational SWE products with both, high spatial and temporal resolution, remains.

1.1. Aim

This thesis aims to answer questions regarding the sensitivity as well as the accuracy of wet snow retrieval using C-band SAR data sets from Envisat's Advanced Synthetic Aperture Radar (ASAR) as well as RADARSAT-2 (RS-2) in combination with measured and modeled parameters at IMIS stations located throughout the Swiss Alps. In addition, the influence of the snow melt process on the retrieved SAR backscatter values is investigated.
The thesis' research questions are as follows:

1. What different ways of retrieving snow wetness information from satellite radar data are there and how do they differ
   a) in terms of accuracy?
   b) in terms of complexity?
   c) in terms of inputs?
2. Which parameters influence the SAR based wet snow retrieval and what is the relative sensitivity to each?
3. Is it possible to retrieve information about the sensitivity of the SAR backscatter to snow pack based information on the locally known depth of the melting process?

1.2. Structure of the thesis

The concepts of SAR, the necessary image processing steps, and the physical properties of snow are introduced in section 2, before the different data sets and the software packages used are described in section 3. The workflow is presented in section 4. The findings of the methods used in the thesis are described in section 5. In section 6, the findings are discussed, followed by a presentation of conclusions and an outlook in sections 7 and 8.

2. Theory

This chapter provides an overview of physical properties of radar remote sensing in general and SAR in particular, followed by a description of the necessary image processing steps. The chapter concludes with a description of the physical properties of snow and its interaction with electromagnetic radiation.

2.1. Physical properties of Radar Remote Sensing

While passive optical imaging systems rely on the availability of sunlight, in Radar Remote Sensing, radars emit short bursts (pulses) of electromagnetic radiation with wavelengths between 1 mm and 1 m, which then interact with the illuminated targets and are (partly) scattered back towards the illuminating system. By measuring the echoes from the illuminated targets, information regarding the target's position and its properties can be retrieved.

2.1.1. Electromagnetic radiation

Electromagnetic radiation can be considered as the "means by which information is transmitted from an object to a sensor" (Elachi & van Zyl, 2006). It consists of oscillating magnetic and electric force field that are perpendicular to one another. The electromagnetic waves propagate at the speed of light c (299 792 458 $^{m}/_{s}$) at varying frequencies (f) and wavelengths (λ), following equation 2.1

$$c = \lambda \cdot f \tag{2.1}$$

The electromagnetic spectrum is divided into different types of radiation (see figure 2.1). While the electromagnetic waves with wavelengths of less than 1 cm can be affected strongly by absorption or scattering caused by atmospheric constituents, wavelengths above 1 cm can penetrate the atmosphere almost without any disturbance (Elachi & van Zyl, 2006). As a result of the absence of atmospheric absorption features in the microwave region, radar imaging systems have an all-weather imaging capability, otherwise often a limiting factor in remote sensing. The microwave spectrum is further subdivided into the bands shown in table 2.1 on the following page (Reddy, 2008).

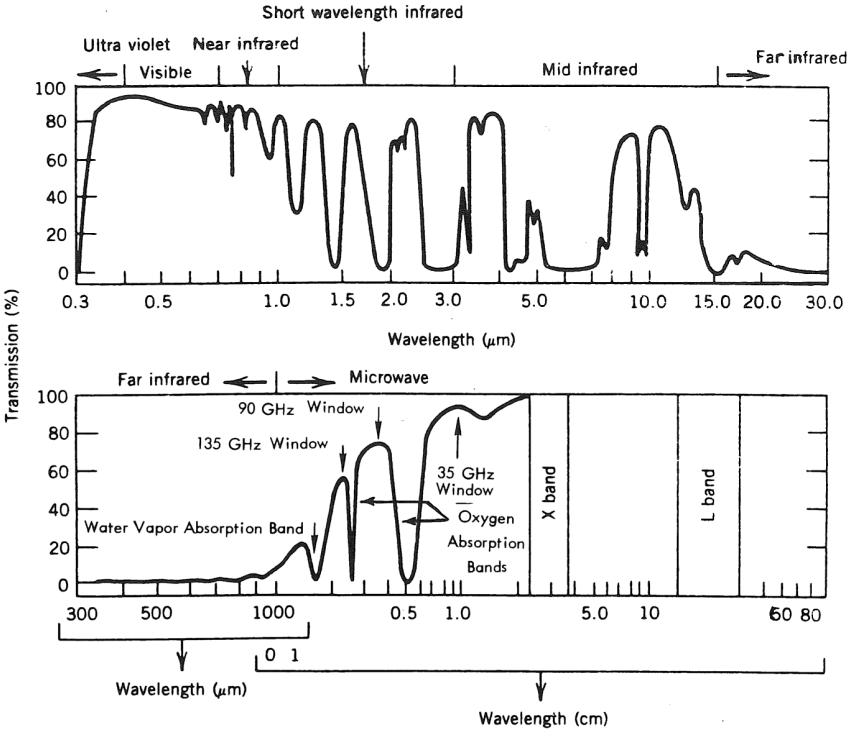

Figure 2.1: Electromagnetic spectrum with atmospheric transmission percentage (Curlander & McDonough, 1991)

Table 2.1: Definition of radar bands (Reddy, 2008)

Band	Frequency [GHz]	Wavelength [cm]
P	0.3 – 1	30 – 100
L	1 – 2	15 – 30
S	2 – 4	7.5 – 15
C	4 – 8	3.75 – 7.5
X	8 – 12	2.5 – 3.75
Ku	12 – 18	1.667 – 2.5
K	18 – 27	1.111 – 1.667
Ka	27 – 40	0.75 – 1.111

2.1.2. Dielectric properties

In addition to the all-weather and day/night imaging capability, the interaction of the electromagnetic waves with the target is one of the key features of radar systems. This interaction is influenced by the target medium's complex dielectric constant that can be described as a

material's ability to store the electric potential under the influence of an electric field. It is defined as

$$\epsilon_r = \epsilon' + i\epsilon'' \tag{2.2}$$

where ϵ' describes the permittivity and ϵ'' the loss factor (Elachi & van Zyl, 2006; Linlor, 1980; Bernier, 1991). With respect to snow, ϵ_r is quite low for dry snow conditions, while the volumetric liquid water content of the snow pack (V_w) causes an increase in ϵ_r due to a higher dielectric constant of water compared to ice (Stiles & Ulaby, 1981). In addition to V_w, grain size, temperature, and frequency influence ϵ_r as well.

2.1.3. Penetration and polarization of microwaves

Interaction with the target leads to a penetration of the wave into the medium, with the penetration depth being governed by the dielectric properties of the medium. The penetration depth is defined as the depth at which the refracted portion of the wave is attenuated by $1/e$ ($\sim$37%), following equation 2.3 given by Ulaby et al. (1986)

$$L_p \approx \frac{\lambda\sqrt{\epsilon'}}{(2\pi\epsilon'')} \tag{2.3}$$

insofar as $\epsilon''/\epsilon' < 0.1$. Accordingly, longer wavelengths (and thus lower frequencies) penetrate deeper into the medium (Curlander & McDonough, 1991), while higher moisture content tends to decrease the penetration depth (see figure 2.2).

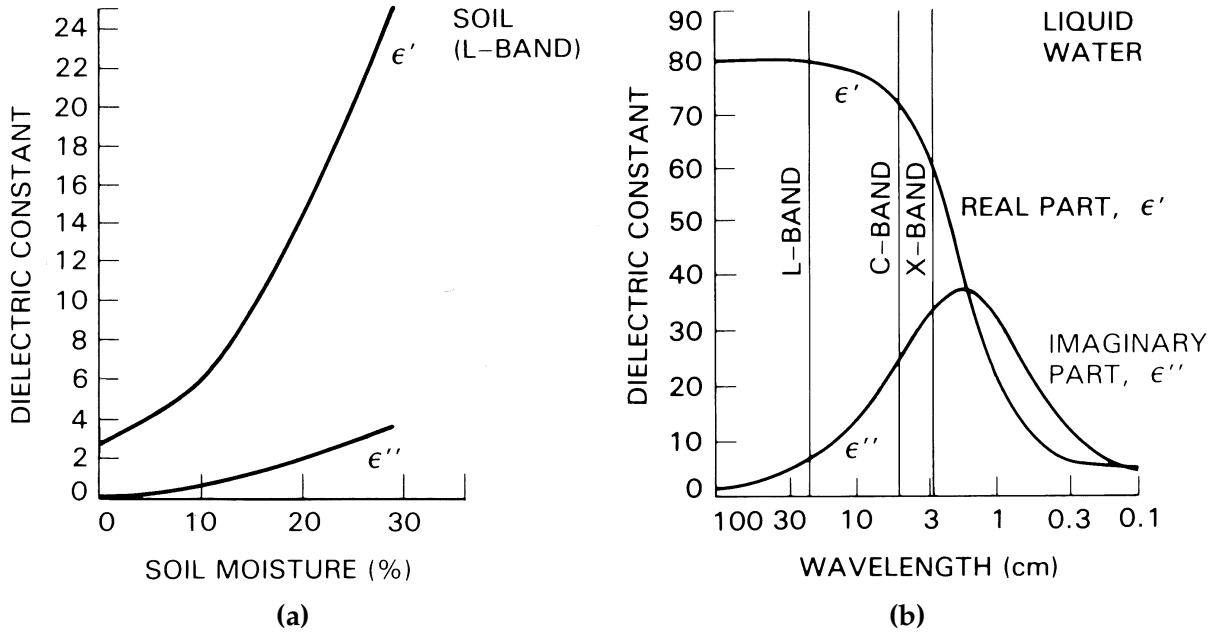

Figure 2.2: Dependence of dielectric constant on (a) soil moisture at L-Band and (b) Radar wavelength (Ulaby et al., 1982)

As a result of the transverse nature of electromagnetic waves, the orientation in which the oscillations take place can be controlled. This property is known as polarization (Woodhouse, 2006). Depending on the orientation of the electric field's oscillations, an electromagnetic wave is said to be horizontally polarized if the displacement takes place parallel to the Earth's surface, or vertically polarized if the plane is perpendicular to the Earth's surface. Depending on the their polarizability, structures respond differently to polarized waves, returning information in addition to the standard backscatter measurements of a radar (Woodhouse, 2006).

2.1.4. Scattering mechanisms

Interaction of the electromagnetic wave and the target can be described using different scattering mechanisms. These can be divided into surface and volume scattering. After Curlander & McDonough (1991), surface scattering is the scattering mechanism from the interface between two different media, while volume scattering results from particles within a non-homogeneous medium.

Surface scattering: Three types of surface scattering mechanisms are distinguished, namely *Fresnel* and *Bragg scattering* as well as *double bounce* (see figure 2.3a). The first two scattering mechanisms

are controlled by the surface roughness. A surface is defined as smooth by the Fraunhofer criterion proposed by Ulaby et al. (1982) if

$$h < \frac{\lambda}{32 \cos \theta} \tag{2.4}$$

where

h = standard deviation of the surface roughness
λ = wavelength
θ = local incident angle

Fresnel scattering applies to smooth surfaces that reflect waves almost entirely (appearing dark in the scene) with incident angles other than zero, the second one applies to slightly rough surfaces with a root mean square of less than $\lambda/8$ (Curlander & McDonough, 1991). Due to the roughness of a surface with *Bragg scattering*, the waves are scattered into a number of different directions, of which a part of the incoming electromagnetic radiation is reflected back towards the sensor, leading to brighter pixels in the radar image compared to the *Fresnel scattering* case (Woodhouse, 2006). The third mechanism called *double bounce* describes a case where the incoming wave is not only reflected by a smooth horizontal surface (e.g. the grass or water), but then hits a vertical object (e.g. a wall or tree trunk), resulting in a large return signal towards the source and thus leading to distinctive, very bright signatures in the radar image that can be used for calibration purposes or ground control points (Woodhouse, 2006).
Volume scattering: Many natural objects have an inhomogeneous nature, whose scattering mechanism cannot be described by surface scattering alone, but needs the addition of the volume scattering mechanism. In this case, the incoming radiation penetrates the uppermost surface of the medium (e.g. leafs or snow), before being scattered and/or reflected off the embedded inhomogeneities.

2.2. SAR image processing

When receiving the return signals scattered by the mechanisms described in section 2.1.4, the uncompressed raw data consisting of the amplitude (A) and phase (φ) information needs to be processed to generate a SAR image. This process chain is generally known as SAR focusing and consists of the three operations shown in figure 2.4 and explained in detail by Curlander & McDonough (1991), Massonnet & Souyris (2008) and Stebler et al. (2008). Following the SAR image processing, the image's geometric and radiometric distortions caused by terrain variations can be addressed in the post-processing (Small, 2011). The post-processing steps, namely geocoding and radiometric calibration, aim to provide a calibrated data base for further analyses

as well as comparisons of data sets (Stebler et al., 2008). In this section, the abovementioned post-processing steps are explained in order to create a mutual understanding of the steps applied to the ASAR and RS-2 scenes used in this study.

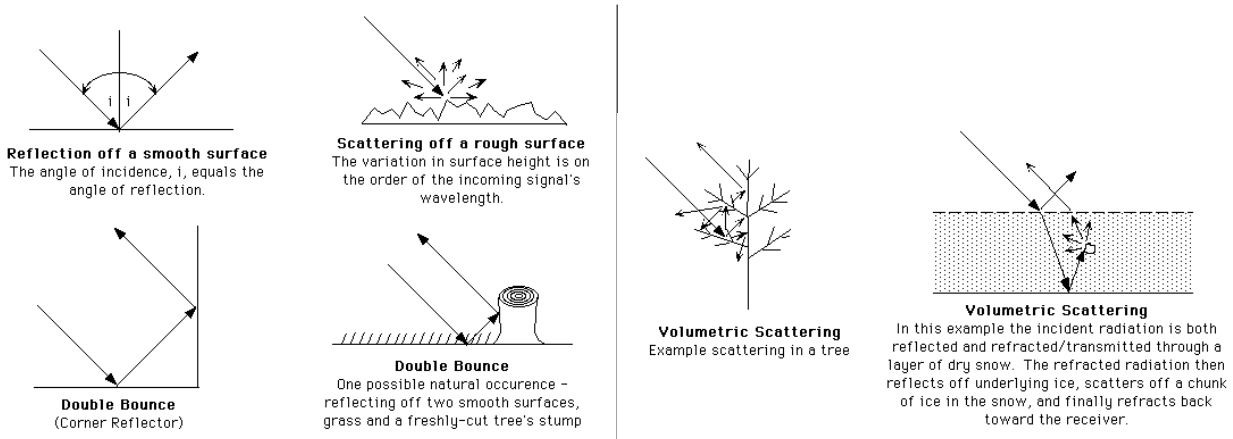

(a) Surface Scattering **(b)** Volumetric Scattering

Figure 2.3: Radar scattering mechanisms (European Space Agency, 2014d)

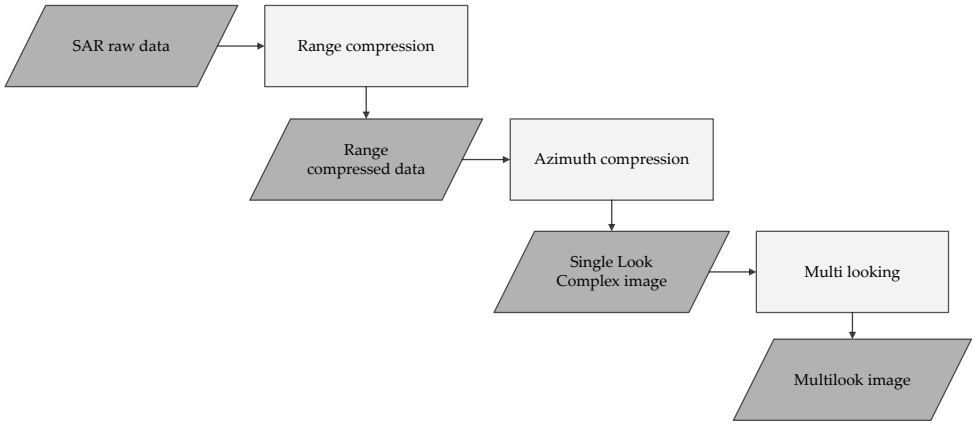

Figure 2.4: SAR image processing steps (adapted from Stebler et al., 2008)

2.2.1. Geocoding

The geocoding processing step aims to find the corresponding location on the Earth's surface for each pixel in the scene, mathematically connecting the observed objects (3D) with the digital representation (2D). This is achieved using either ellipsoidal heights or a Digital Elevation Model

(DEM) with the rigorous Range-Doppler approach, taking topographic effects into account topographic effects as well as the sensor's state vectors (Meier, 1989; Stebler et al., 2008).

2.2.2. Radiometric calibration

For meaningful multi-sensor or time series intercomparisons, a common normalization of the SAR backscatter values is needed (Small, 2011). Therefore, a definition of the term *backscatter* is necessary. According to Small (2011), *backscatter* β is defined as the "ratio between the scattered power P_s and incident power P_i at ground level", hence

$$\beta = {}^{P_s}/_{P_i} \tag{2.5}$$

Since the assumption of point targets is not usually valid, there is a need for an areal normalization of β, returning a so called backscatter *coefficient* (Ulaby et al., 1982). Depending on the reference area and the terrain model chosen (see figure 2.5) the resulting backscatter coefficients return different information (Small, 2011):

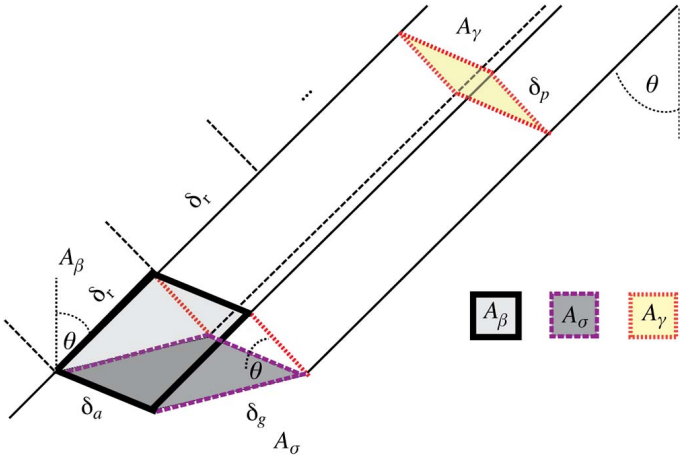

Figure 2.5: Reference areas for SAR backscatter (Small, 2011)

– *Beta naught (β^0):* The solid rectangle A_β lies in the slant range plane; the resulting backscatter is known as radar brightness and is generally defined as

$$\beta^0 = \frac{\beta}{A_\beta} \tag{2.6}$$

In case of the ASAR system, Rosich & Meadows (2004) defined the relationship between radar brightness (β^0) and the value of the image pixels ("Digital Number (DN)") as follows

$$\beta^0_{i,j} = \frac{DN^2_{i,j}}{K} \tag{2.7}$$

where

K = absolute calibration constant; derived from measurements over precision transponders
$DN^2_{i,j}$ = pixel intensity value at image line and column i,j

– *Sigma naught (σ^0):* When the ground area A_σ is chosen as reference area, the resulting backscatter coefficient is calculated using an ellipsoidal Earth model (denoted with a subscript E), in order to be able to gain knowledge of the incident angle θ_E (Small, 2011). The formula is as follows

$$\sigma^0_E = \beta^0 \cdot \frac{A_\beta}{A_\sigma} = \beta^0 \cdot \sin\theta_E \tag{2.8}$$

– *Gamma naught (γ^0):* This third backscatter coefficient uses the plane perpendicular to the line of sight (A_γ) as the reference area for the normalization and applies the following formula

$$\gamma^0_E = \beta^0 \cdot \frac{A_\beta}{A_\gamma} = \beta^0 \cdot \tan\theta_E \tag{2.9}$$

As the A_γ area is closest to the actual amount of ground "visible" to the radar, its use is preferred (Small, 2011).

Geocoded Terrain Correction (GTC)

When the SAR scene's σ^0_E and γ^0_E values are calculated using an ellipsoidal Earth model and terrain-geocoded using a DEM, the output is a Geocoded Terrain Corrected (GTC) product (Small, 2011). While the flat-earth assumption is valid for regions with flat terrain, it doesn't hold true for rugged, mountainous regions, where the backscatter information mixes terrain-induced as well as thematic effects (Small et al., 2007).

Radoimetrically Terrain Corrected (RTC)

As mentioned in the last section, rugged, mountainous terrain requires additional calibration steps in order to remove changes of the recorded brightness values caused by changes in the local scattering area and changing scattering mechanisms due to different incident angles. Additionally, the target surface's slope and aspect can cause significant changes to the scattering area within neighboring resolution cells due to shadowing, foreshortening and layover effects,

leading to uncertainties critical for quantitative image analysis (Loew & Mauser, 2007; Small, 2011). In order to overcome these uncertainties, the ellipsoid model is replaced by a DEM, based on which a Local Incidence Angle Mask (LIM) can be calculated. In connection with the local incident angle θ_E, a Slope Correction Factor (SCF) can be calculated as follows (Kellndorfer et al., 1998)

$$\sigma_T^0 = \beta^0 \cdot \frac{A_\beta}{A_\sigma} = \sigma_E^0 \cdot \frac{\sin\theta_{LIM}}{\sin\theta_E} \tag{2.10}$$

The σ_T^0 normalization (the T denoting the use of a terrain model) is referred to as "NORLIM" by Small (2011). In order to overcome the angular methods' inaccurate modeling of layover and foreshortening, Small (2011) stresses the need for a backscatter normalization that uses a reference DEM to spatially integrate all local illuminated areas (A_γ) at each radar geometry position before using this local reference area in the normalization process as follows

$$\gamma_{T_{i,j}}^0 = \beta_{i,j}^0 \cdot \frac{A_\beta}{\int\limits_{DHM} A_{\gamma_{i,j}}} \tag{2.11}$$

The difference between a GTC and a Radiometrically Terrain Corrected (RTC) scene is presented in figure 2.6 on the next page, showing considerable improvements for thematic interpretations of the RTC scene such as wet snow cover. A summary of the SAR backscatter normalization conventions is given in table 2.2.

Table 2.2: SAR backscatter normalization conventions (modified from Small, 2011)

Convention	1	2	3	4	5
Symbol	β^0	σ_E^0	γ_E^0	σ_T^0	β_T^0
Earth Model	None	Ellipsoid	Ellipsoid	Terrain	Terrain
Reference Area	A_β	$\underline{A}_\beta$	$\underline{A}_\gamma$	$\underline{A}_\sigma$	A_γ
Normalization	$\beta^0 = \frac{\beta}{A_\beta}$	$\sigma_E^0 = \beta^0 \cdot \frac{A_\beta}{A_\sigma}$ $= \beta^0 \cdot \sin\theta_E$	$\gamma_E^0 = \beta^0 \cdot \frac{A_\beta}{A_\gamma}$ $= \beta^0 \cdot \tan\theta_E$	$\sigma_T^0 = \beta^0 \cdot \frac{A_\beta}{A_\sigma}$ $= \sigma_E^0 \cdot \frac{\sin\theta_{LIM}}{\sin\theta_E}$	$\gamma_T^0 = \beta^0 \cdot \frac{A_\beta}{\int_{DHM} A_\gamma}$
Product		GTC		NORLIM	RTC

2.3. Physical properties of snow

In order to understand the factors influencing the SAR backscatter from a snow pack, knowledge about its physical properties is vital. This chapter gives an overview of relevant physical properties and characteristics of snow with regard to microwave remote sensing as well as the techniques used to derive information about the state of the snow pack, based mainly on the

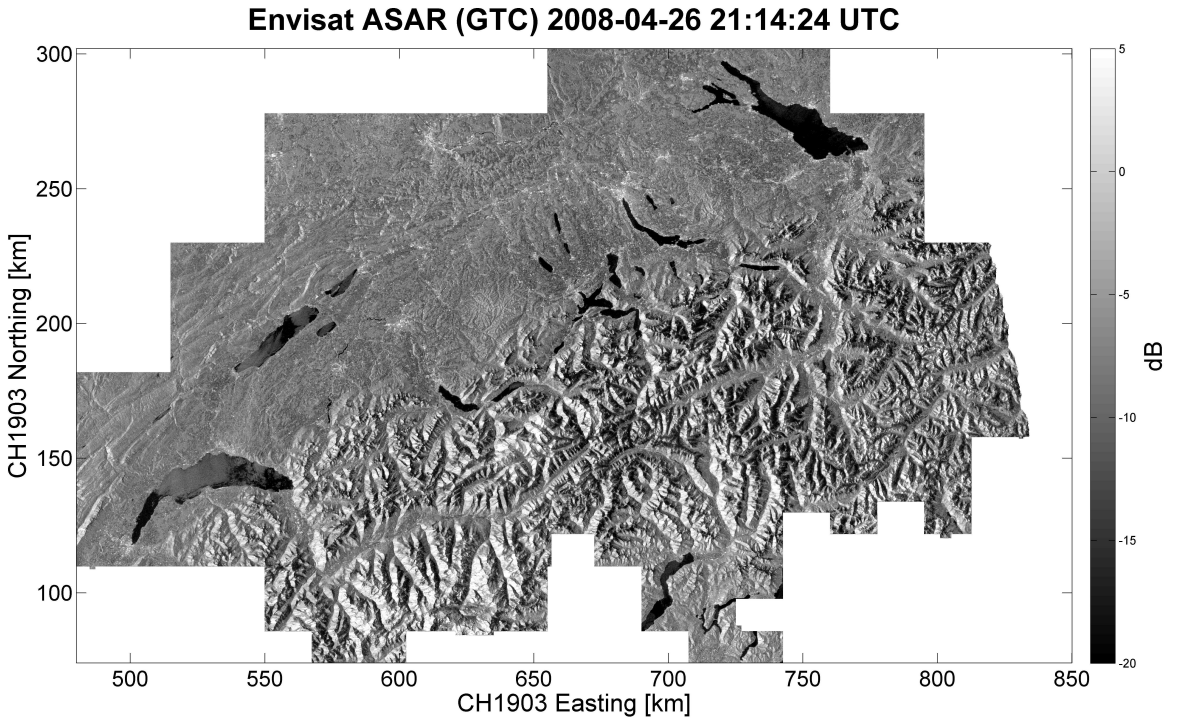

(a) GTC image (γ_E^0)

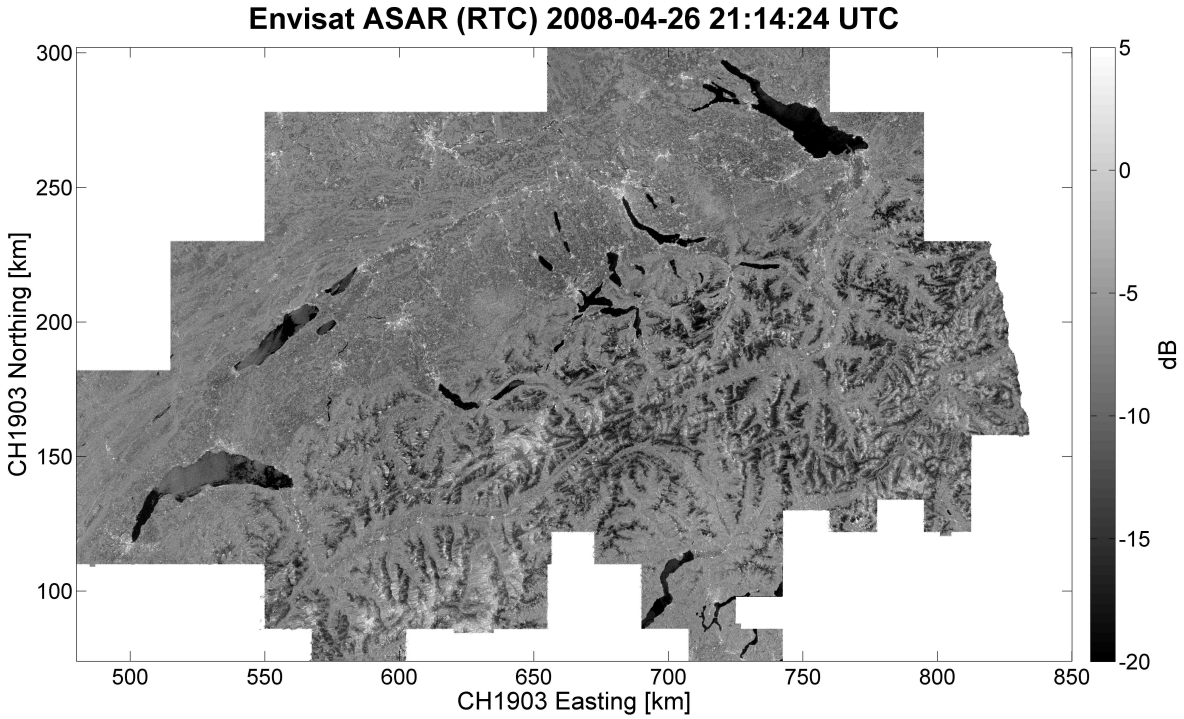

(b) RTC image (γ_T^0)

Figure 2.6: Differences between GTC and RTC

publications from Rees (2006), DeWalle & Rango (2008), Singh & Singh (2001), and Seidel & Martinec (2004).

2.3.1. Description of snow and snow pack

A snow pack's most basic physical parameter is its density ρ_s, a value normally ranging between 1 g/cm^3 for freshly fallen snow and 6 g/cm^3 for one-year-old snow (although in very cold conditions, the density of the fresh snow can be as low as 0.01 g/cm^3). The increase in snow pack density results from the compaction process induced by wind, gravity, and thermal metamorphism. Regarding the snow pack's internal structure, the most important parameter is *grain size*. It is generally defined as the ice crystal's mean radius, with some definitions taking its form and orientation into account as well. Even though grain sizes of 0.01 mm have been reported for new, low-density snow, the grain size typically lies between 0.1 and 3 mm. As a result of melting and refreezing, the crystals can merge together, forming macroscopic inclusions of solid ice.
The third parameter often used to characterize the snow pack is defined by the snow's *wetness w*, often referred to as LWC. This unit is defined as the availability of water content in the form of liquid in a snow pack, not only including the capillary water between the snow crystals, but also the gravitational water moving downward within the snow pack. LWC is usually expressed as a volumetric percentage, sometimes as a mass percentage. The volumetric LWC values normally range between 0% for snow packs with temperatures below 0°C up to around 10% for temperate snow packs. The upper limit is defined by the snow's ability to hold liquid water in its pores; higher volumetric LWC values lead to drainage of the liquid water at the bottom of the snow pack. Since the LWC does not say anything about the absolute amount of melt water within a snow pack, this parameter is described by the SWE d_w. It is defined as the depth (e.g. in meters) of all liquid water that would be released upon complete melting of the snow pack. It can be calculated as follows

$$\mathrm{SWE} = \frac{\rho_s}{\rho_w} \cdot d \tag{2.12}$$

where

SWE	=	snow water equivalent [m]
ρ_s	=	snow pack density [kg/m^3]
ρ_w	=	density of liquid water, approx. 1 000 kg/m^3
d	=	snow pack depth [m]

According to Rees (2006), SWE will typically be about a third of the snow pack's depth, although with low-density snow this value can be much lower.
Not only the the snow pack's internal properties influence the interaction of the electromagnetic radiation with the snow pack, but also the surface geometry, represented by the *surface roughness*

(at larger scales this becomes *surface topography*) (Rees, 2006; DeWalle & Rango, 2008; Singh & Singh, 2001).

2.3.2. Dielectric properties of snow

According to Bernier (1991), snow can be considered as a mixture of ice, air, and water. Therefore, the dielectric properties of the snow pack depend on its density, the size of the ice crystals, as well as the dielectric constant of ice, air, and water. As the dielectric constant changes considerably between water (extremely high dielectric values) and ice (extremely low dielectric values), two cases have to be considered: *dry* and *wet snow* conditions (Woodhouse, 2006).

Dry snow

As dry snow consists of closely-spaced ice needles where the host medium is simply air, the extremely high dielectric constant of water does not need to be considered. Therefore, the overall low dielectric constant of dry snow is a result of an extremely low dielectric constant of ice in combination with the one of air (according to Rees (2006), air can be assumed to be free space with a dielectric constant of 1), the microwaves do not interact greatly with the dry snow pack, resulting in a penetration depth L_p of more than 10 m for C-band (Piesbergen, 2001; Bernier, 1991; Woodhouse, 2006; Rees, 2006).

Wet snow

As opposed to dry snow, wet snow includes droplets of water between the ice particles. Due to the extremely high dielectric constant of liquid water, it has a very strong effect on absorption, resulting in a penetration depth L_p for a snow pack with an LWC of 2% of only a few centimeters.

2.3.3. Backscatter properties of snow

The backscatter signature of a snow pack is a mixture of the geometric structure as well as the electromagnetic properties of ice, air, water vapor, and the liquid water. As dry snow is transparent to a C-band microwave sensor, the backscatter signal for a snow pack of 1–3 m is approximately equal to the surface scattering of the underlying soil, since the surface scattering at the air/snow interface can be ignored for incident angles above 45° (Piesbergen, 2001; Bernier, 1991; Strozzi, 1996). According to Rees (2006), the volumetric scattering from the irregularities within the bulk of the medium (i.e. snow pack) can be neglected as well, unless the snow pack is too deep.
In the case of wet snow, the backscatter processes are different, as the dielectric constant of

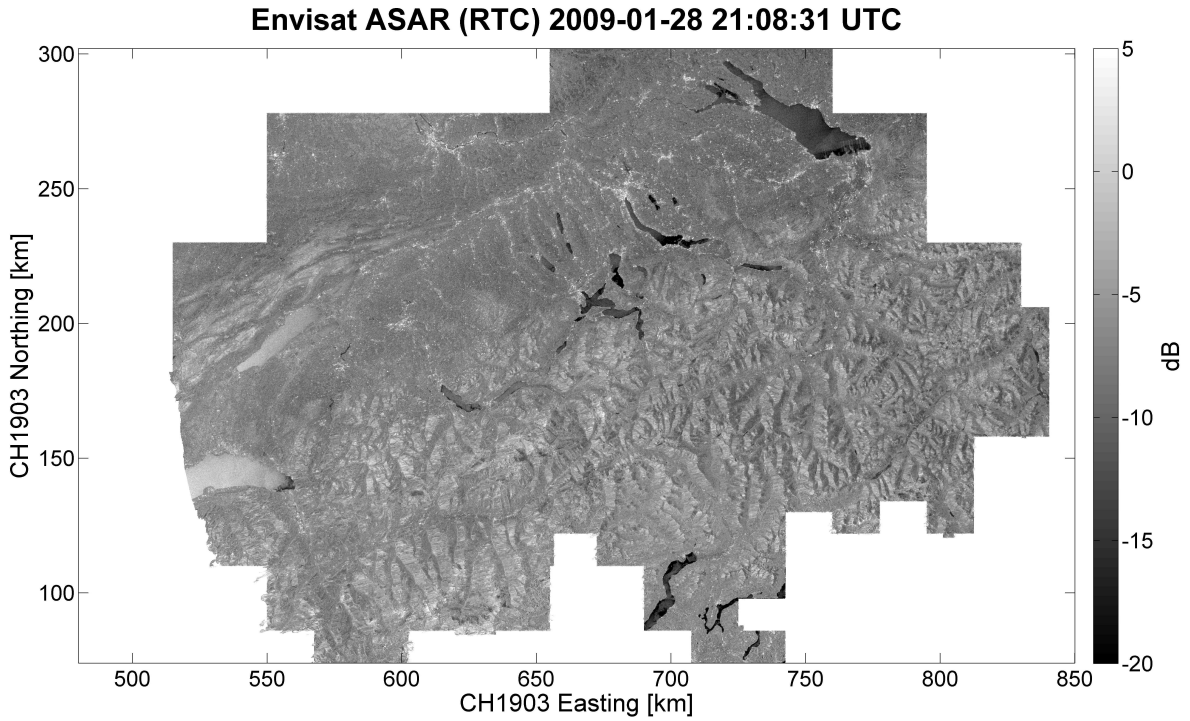

(a) Dry snow

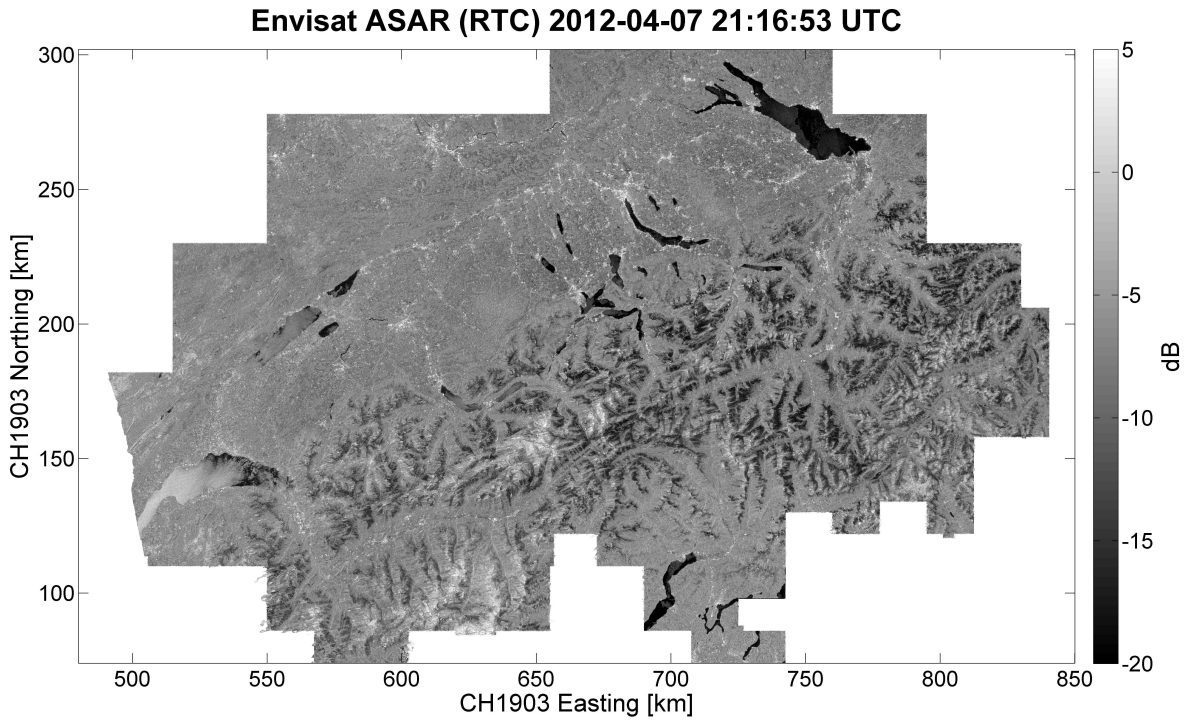

(b) Wet snow

Figure 2.7: Backscatter differences between dry and wet snow conditions

wet snow (ϵ'', see section 2.3.2 on page 14) is much higher than in the dry snow case. This increase in ϵ'' leads to an increased scattering at the air/snow interface as well as a decrease in penetration depth L_p, thus surface scattering becomes the main contributor to the backscattered signal, which itself is governed by frequency, polarization, incident angle, and surface roughness (Bernier, 1991; Rees, 2006).

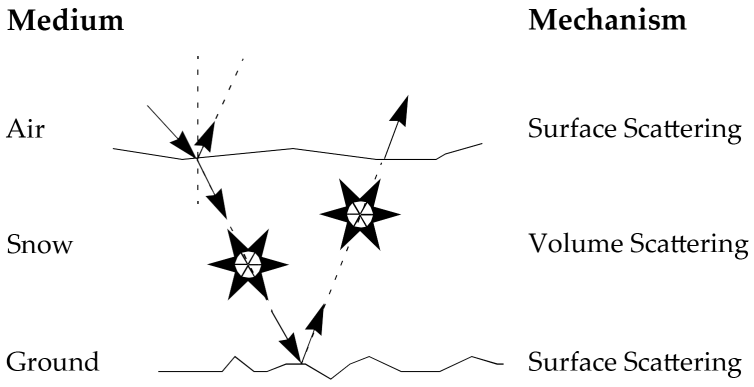

Figure 2.8: Microwave backscattering from snow (based on Piesbergen, 2001)

3. Data

The data sets used for this thesis can be divided into five categories that are discussed in detail in the following chapter. The SAR data sets included data from both ASAR and RS-2. There were also data sets from optical remote sensing, ground measurements provided by SLF, meteorological data from both SLF and Federal Office of Meteorology and Climatology (MeteoSwiss), as well as auxiliary data sets from a multitude of sources. At the end of this chapter, the software used for data processing is described.

3.1. SAR

3.1.1. Envisat ASAR

Envisat was launched with an Ariane 5 rocket from the *Centre spatial guyanais* in Kourou (French Guiana) on 1 March 2002, carrying ten remote-sensing instruments, including the Advanced Synthetic Aperture Radar (ASAR) used in this thesis (European Space Agency, 2014a). Envisat orbited the Earth in a sun-synchronous polar orbit of about 800 km altitude, passing the equator at 10:00/22:00 mean local time in descending/ascending orbit. With 501 orbits in cycle and an orbit period of 100.59 minutes, Envisat had a repeat cycle of 35 days (European Space Agency, 2014a).
The data set used for this thesis comprised a total of 330 scenes from the beginning of 2007 until the contact to the satellite was lost on 8 April 2012 (European Space Agency, 2012). The scenes were acquired in the Wide Swath Mode (WSM) with ASAR's C-band SAR, centered at 5.331 GHz. The use of this imaging mode with a resolution of 150 m and a pixel spacing of 100 m at a swath width of 405 km offered the possibility of covering Switzerland's whole area in single scene (European Space Agency, 2007). Although ASAR acquired the scenes in both VV and HH polarization, only six scenes in 2011 were available in HH polarization for this thesis.
The data set's temporal resolution was on average one scene every six days between 2007 – 2011, and one scene every two days for 2012 (see figure 3.1 on the next page). The image acquisitions took place around 09:45 UTC (descending orbit) and 21:15 UTC (ascending orbit).
For every acquisition, four data sets were used as input. These were a Geocoded Terrain Corrected (GTC), as well as an Radiometrically Terrain Corrected (RTC), a Local Incidence Angle Mask (LIM) and an Area data set, of which the latter two were needed for the RTC processing (see section 2.2.2). All these data sets were geocoded using the Swiss national grid coordinates (CH1903). All had the same pixel spacing of 100 m as well as identical extents.
As the data sets were acquired with different incidence angles as well as different orbit configurations, the use of RTC scenes was preferred over GTC scenes (see chapter 2.2.2 on page 10).

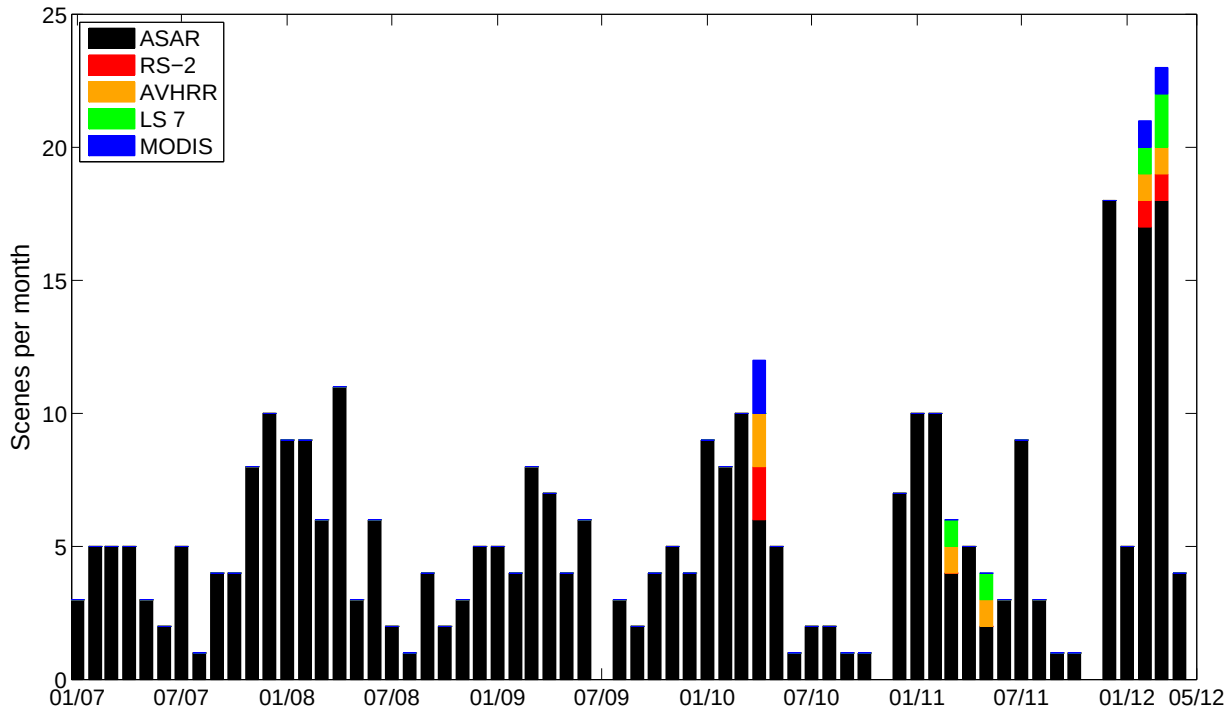

Figure 3.1: Distribution of scenes per month (2007 – 2012)

The Area data set was used for the derivation of Local Resolution Weighting (LRW) composites (see 4.3 on page 33) and the selection of suitable IMIS stations (see section 4.1 on page 29), while the LIM rasters were used for the derivation of the RTC representations.

3.1.2. RADARSAT-2

In addition to the ASAR data sets, four RADARSAT-2 (RS-2) scenes were used. RS-2 is a collaboration between MacDonald, Dettwiler and Associates Ltd. (MDA) and the Canadian Space Agency (CSA) and was launched on 14 December 2007 on a SOYUZ-FG rocket from Baikonur (Kazakhstan) (Hillman et al., 2009). The satellite orbits the Earth in a sun-synchronous polar orbit of 798 km altitude, passing the equator at 06:00/18:00 mean local time in descending/ascending orbit. Its orbit duration is 100.7 minutes, resulting in a repeat cycle of 24 days (Hillman et al., 2009; MacDonald, Dettwiler and Associates Ltd., 2011, 2014).
The images were acquired using the sensor's ScanSAR Narrow beam mode, providing a swath width of 300 km with a resolution of 50 m using a C-band SAR centered at 5.405 GHz (MacDonald, Dettwiler and Associates Ltd., 2011, 2014). The four scenes were acquired in 2010 and 2012 and are available in both VV and VH polarization for all four dates, covering around 90% of Switzerland's area (see figure 3.1 and table 3.1 on the next page). For compatibility reasons, all

were available as well with a 100 m pixel spacing in order to match the ASAR scenes. As for the ASAR scenes, each acquisition was available as an Area, LIM, GTC, and RTC representation. As mentioned in the description of the Envisat ASAR data set, the use of RTC scenes was preferred over GTC representations. As a result of the limited data set, the Area data set was only used with the scenes acquired on 26 April 2012 and 27 April 2012 in order to calculate a LRW composite. As mentioned previously, the LIM rasters were not used directly.

Table 3.1: RS-2 image characteristics

Date	Orbit	Areal coverage of CH
2010-04-26 17:23:36 UTC	Ascending	89%
2010-04-27 05:33:21 UTC	Descending	94%
2012-02-28 05:33:37 UTC	Descending	94%
2012-03-23 05:33:37 UTC	Descending	94%

3.2. Optical remote sensing

For the validation of the wet snow classification using SAR scenes (see section 4.2 on page 30), optical data sets stemming from the AVHRR, Landsat 7 (LS 7), and the MODIS were used. As shown in figure 3.1 on the preceding page and table 3.2, the acquisitions were from 2010 to 2012.

Table 3.2: Availability of optical remote sensing scenes for comparisons

	AVHRR	LS 7	MODIS
2010-04-26	✓	×	✓
2010-04-27	✓	×	✓
2011-03-20	×	✓	×
2011-03-28	✓	×	×
2011-03-29	×	✓	×
2011-05-28	✓	×	×
2011-05-30	×	✓	×
2012-02-28	✓	✓	✓
2012-03-22	×	✓	×
2012-03-23	✓	×	✓
2012-03-24	×	✓	×

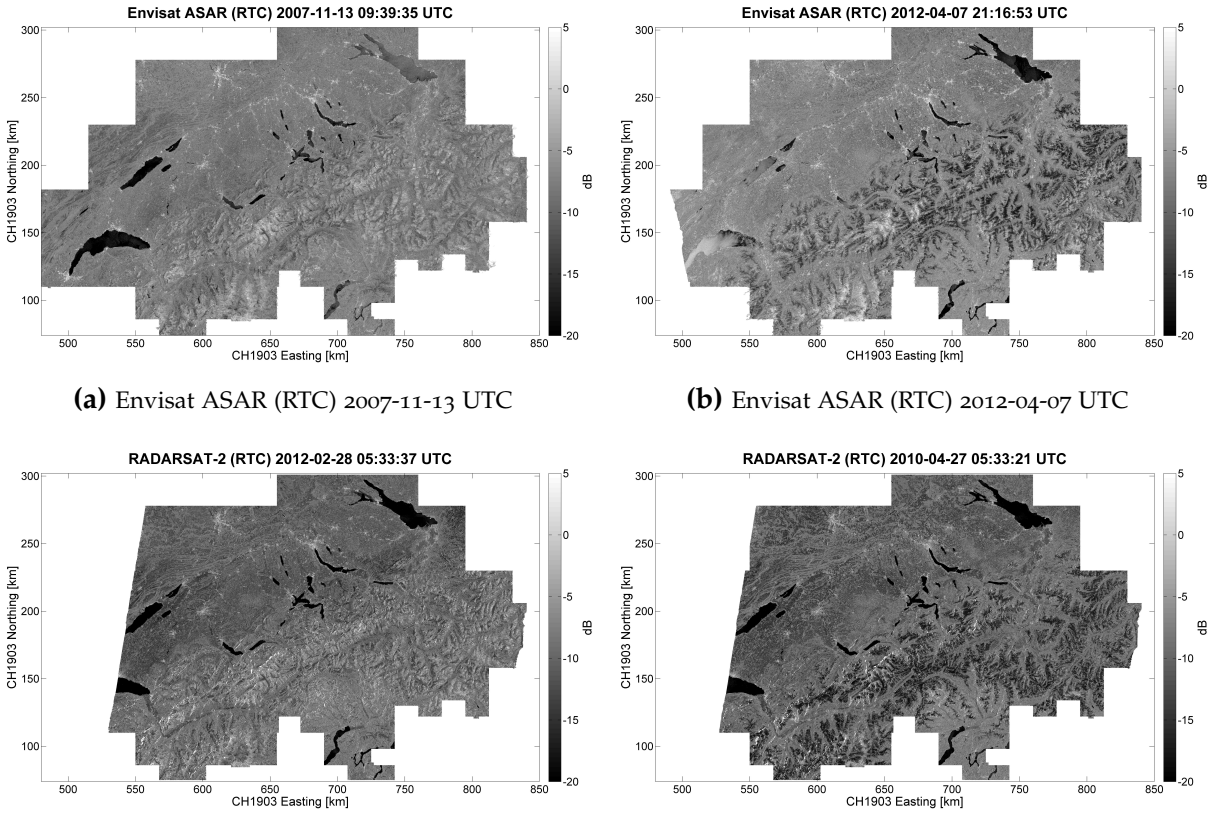

(a) Envisat ASAR (RTC) 2007-11-13 UTC

(b) Envisat ASAR (RTC) 2012-04-07 UTC

(c) RADARSAT-2 (RTC) 2012-02-28 UTC

(d) RADARSAT-2 (RTC) 2010-04-27 UTC

Figure 3.2: Dry/wet snow conditions in Envisat ASAR/RADARSAT-2 RTC scenes

3.2.1. AVHRR Snow Extent

The six AVHRR snow extent products were produced and provided by the Remote Sensing Research Group from the University of Bern, distributed evenly across the years 2010, 2011, and 2012. The scenes were available in both single path as well as daily maximum composites, both in WGS84 projection and with a spatial resolution of 0.01°. In order to be able to use the data with both the ASAR and the RS-2 scenes, the projection was changed to CH1903 and the pixels resampled to 100 m/25 m using the nearest neighbor approach. The AVHRR snow extent product was classed into five discrete values, shown in table 3.3. As the daily maximum composites incorporated a maximum of 2–3 overpasses per day (Hüsler et al., 2014), they were used for validation purposes.

The AVHRR snow extent product was the only optical product including information on the cloud cover of each scene.

Table 3.3: Classification scheme of the AVHRR snow extent product

Pixel value	Cover type
0	No snow
100	Snow
200	Water
250	Cloud
255	No data

Table 3.4: Areal statistics for the AVHRR snow extent scenes (Hüsler et al., 2014)

Scene	Areal cover of CH [%]	Areal snow cover of CH [%]	Areal cloud cover of CH [%]	Areal No Data cover of CH [%]
2010-04-26	100.00%	16.83%	71.12%	0.00%
2010-04-27	100.00%	16.12%	58.08%	0.00%
2011-03-28	100.00%	13.69%	78.46%	0.00%
2011-05-28	54.94%	8.32%	10.26%	45.06%
2012-02-28	100.00%	42.33%	41.08%	0.00%
2012-03-23	68.24%	19.64%	0.16%	31.76%

3.2.2. Landsat 7

The LS 7 scenes consisted of a total of nine acquisitions on six days in the years 2011 and 2012. They had a spatial resolution of 30 m and were processed and provided by Dr. Hendrik Wulf from the Remote Sensing Laboratory (RSL) at the University of Zurich. As with the AVHRR snow extent data set, the LS 7 data set was resampled and projected to match the ASAR and RS-2 scenes.

The snow classification for the scenes was made using the Normalized Difference Snow Index (NDSI) algorithm, described by Seidel & Martinec (2004) as follows:

$$NDSI = \frac{TM2 - TM5}{TM2 + TM5} \approx \frac{MODIS4 - MODIS6}{MODIS4 + MODIS6} \tag{3.1}$$

where

$TM2$ = LS 7 Enhanced Thematic Mapper Plus (ETM+) band 2 (525–605nm)
$TM5$ = LS 7 Enhanced Thematic Mapper Plus (ETM+) band 2 (1 550–1 750nm)
$MODIS4$ = MODIS band 4 (545–565nm)
$MODIS6$ = MODIS band 4 (1 628–1 652nm)

The values returned were then converted to FSC, with values >0.4 indicating the presence of snow (Hendrik Wulf, 2014-09-11, personal communication). As there are multiple scenes per

day covering different areas of Switzerland, these same-day acquisitions were further combined into one single scene. The same procedure was used to combine the scenes from 22 March 2012 and 24 March 2012. As can be seen in figure 3.3, the product shows striping effects due to the failure of Landsat's Scan Line Corrector (SLC). A 'no data' flag was applied to all affected pixels. As opposed to the aforementioned AVHRR snow extent product, this data set did *not* include information regarding the cloud cover, since only the FSC values and no data values were stored.

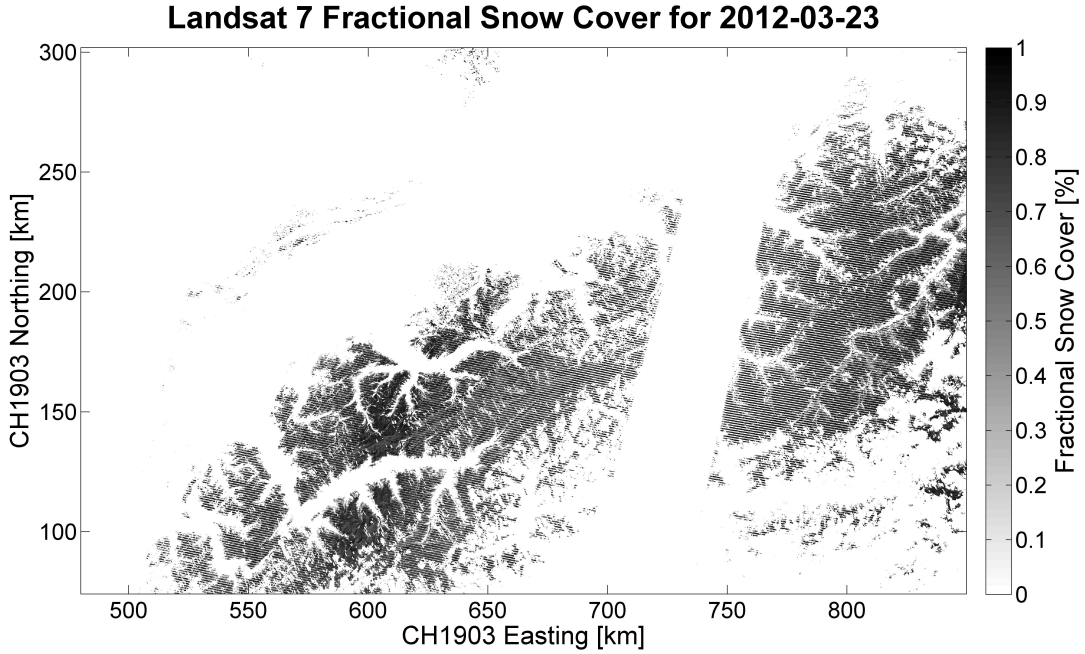

Figure 3.3: Landsat 7 FSC for 2012-03-23

3.2.3. MODIS Aqua/Terra

The third snow cover data set was based on the MODIS/Terra Snow Cover Daily L3 Global 500 m Grid (MOD10A1) data set, providing daily FSC values ranging from 0–100 (Hall et al., 2006). The gaps in the MOD10A1 FSC product caused by cloud cover were interpolated by Dr. Hendrik Wulf using data from the Aqua and Terra satellites (Hendrik Wulf, 2014-09-11, personal communication). Cloud cover was not specifically flagged, but a value of 0 was attributed to such pixels. The 2.74% *No Data* values stemmed from the water bodies that have been masked out of the final product. The spatial resolution of the original four scenes was approximately 460 m, later resampled to 100 m/25 m using ArcMap 10.2.1.

Table 3.5: Areal statistics for the Landsat 7 scenes

Scene	Areal cover of CH [%]	Areal snow cover of CH [%]	Areal No Data cover of CH [%]
2011-03-20	17.36%	8.17%	82.64%
2011-03-29	17.91%	2.42%	82.09%
2011-05-30	10.27%	0.03%	89.73%
2012-02-28	32.72%	20.29%	67.28%
2012-03-22	43.96%	12.41%	56.04%
2012-03-24	10.32%	7.30%	89.68%

Table 3.6: Areal statistics for the MODIS Aqua/Terra scenes

Scene	Areal cover of CH [%]	Areal snow cover of CH [%]	Areal No Data cover of CH [%]
2010-04-26	97.26%	23.44%	2.74%
2010-04-27	97.26%	22.90%	2.74%
2012-02-28	97.26%	53.70%	2.74%
2012-03-23	97.26%	39.64%	2.74%

3.3. Ground measurements

The ground measurement data used for this thesis originated from the IMIS network operated by SLF. This measurement network consists of 114 automated measurement stations throughout the Swiss Alps (see table A.1) providing information regarding meteorological as well as snow parameters. The point measurements were made once every 30 minutes and transmitted to SLF on an hourly basis (Lehning et al., 1999). The parameters measured at IMIS snow stations are listed in table 3.7 on the next page. Due to the remote locations of the stations, the electrical power supply is ensured by a battery charged using a solar panel. Therefore, the sensors cannot be heated or ventilated, leading to the possibility of measurement errors as well as data gaps (Lehning et al., 1999).
However, these stations do not measure the SWE or the amount of fresh snow directly. Therefore, a physical snow pack model is used at SLF to estimate additional parameters (Jonas, 2012; Lehning et al., 2002, 1999).

3.3.1. SNOWPACK output

SNOWPACK is a finite-element based physical snow pack model, developed and run by SLF to provide additional information for avalanche forecasting (Lehning et al., 1999). It models

Table 3.7: Parameters measured at IMIS stations (Lehning et al., 1999)

Abbrev.	Description	Measurement units
HS1	Snow depth	[cm]
TA	Air temperature	[° C]
TSS	Temperature of snow surface	[° C]
TS1/TS2/TS3	Temperature of snow at 25/50/100 cm	[° C]
TS0	Ground temperature	[° C]
RSWR	Reflected short-wave radiation	[W/m^2]
RH	Relative humidity	[%]
	Wind speed (average/peak)	[m/s]
	Wind direction	[°]

snow as a three-phase porous medium (ice, water, and air), characterized by each phase's volumetric content as well as micro-structural parameters derived from the network of IMIS stations (Lehning et al., 1999, 2002).
Since point measurements, as realized with the IMIS network or manually dug snow pits, are not able to capture to snow's high spatial variability, the parameter outputs from the SNOWPACK model were used in this thesis to derive continuous information regarding the state of the snow pack. From the multitude of parameters only few were used for this thesis. These parameters were layered information on LWC, snow pack density, and snow temperature. The layered nature of the aforementioned parameters included the value of snow height for every measurement intrinsically.

3.4. Meteorological data

In addition to the meteorological values measured at the IMIS stations (see section 3.3), two data sets provided by MeteoSwiss were used. As a source of point measurements with a high temporal resolution (up to one measurement every 10 minutes) the CLIMAP-net database from MeteoSwiss was utilized. Out of the many parameters available, precipitation, air temperature and wind speed/direction information were chosen to identify possible reference scenes for the wet snow detection process. In addition to the CLIMAP-net point measurements, the gridded data sets from MeteoSwiss provided regularly spaced areal representations of meteorological parameters such as temperature, precipitation, and sunshine duration at daily/monthly/yearly intervals. The grids were generated using advanced interpolation techniques based on measurements from CLIMAP-net stations and had a spatial sample interval of 0.02083 degrees, equaling approximately 2.3 km the in West-East direction, and 1.6 km in the North-South direction (MeteoSwiss, 2011).

Figure 3.4: Example of an IMIS station (Hinterrhein–Unter Surettasee, see table A.1; courtesy of Dr. Tobias Jonas)

3.5. Auxiliary data sets

Additional geodata were used to investigate influencing factors of the SAR backscatter as well as for illustration purposes. These data sets originated from the Federal Office of Topography (swisstopo) as well as from the Federal Statistical Office (BFS).

- *Federal Office of Topography (swisstopo)*
  - DHM25: For extraction of elevation, slope, and aspect information, this DEM with a spatial resolution of 25 m was used. It covered all of Switzerland as well as small parts of the neighboring countries (Swiss Federal Office of Topography, 2004).
  - swissBoundaries^{3D}: For illustration purposes, the national/municipal boundaries derived from the municipal boundary data set were used. The boundaries represent the state as per 2013 (Swiss Federal Office of Topography, 2013b).

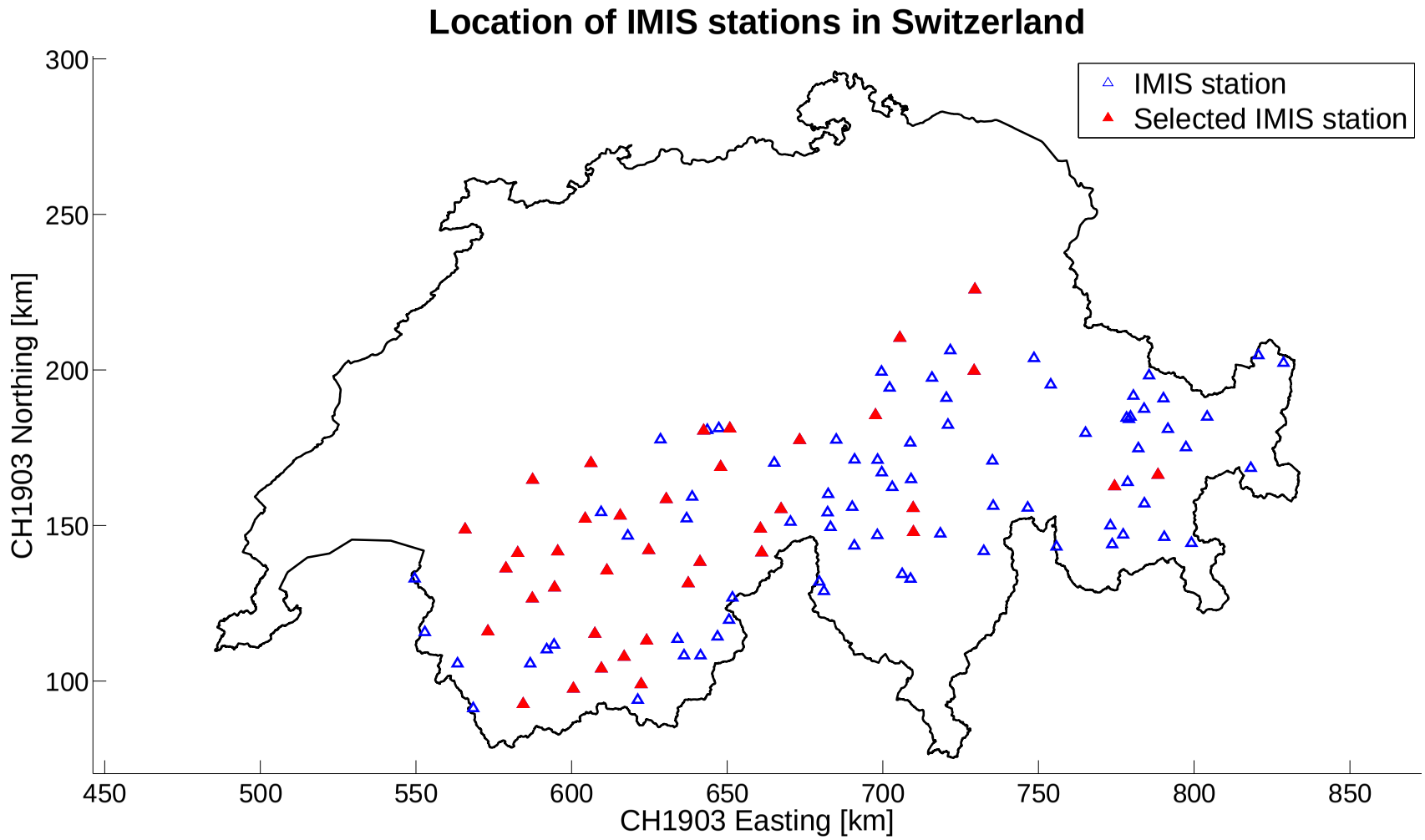

Figure 3.5: Location of IMIS stations. Red triangles denominate IMIS stations that were selected for this thesis, while blue triangles denominate other IMIS stations not considered in for the study due to problematic topography or the presence of unrelated features in the scene (see section 4.1)

- swissALTI^{3D}: For the geolocation of the IMIS stations, the high resolution DEM with a spatial resolution of 2 m was used. The DEM was created using both Light Detection And Ranging (LIDAR) and stereo correlation techniques (Swiss Federal Office of Topography, 2013a).
- SWISSIMAGE: The orthophoto mosaic with a spatial resolution of 0.25 m was used for the geolocation of the IMIS stations as well as for illustration purposes (Swiss Federal Office of Topography, 2010).
- VECTOR25: To mask out the influence of water bodies from the analysis, the vector data set from swisstopo was used (Swiss Federal Office of Topography, 2007). The lake mask included every lake – natural or artificial – larger than 0.4 km². The underlying soil cover information was also extracted from the VECTOR25 data set. Therefore, multiple categories were merged into the classes *bedrock*, *detritus*, and *glacier* as shown in table 3.8.

Table 3.8: Merged categories from the VECTOR25 data set to derive soil cover information

Bedrock	Detritus	Glacier
Z_Fels (Bedrock)	Z_GerGeb (Detritus with shrubbery) Z_GerGle (Detritus on glacier) Z_Geroel (Detritus) Z_GerWaO (Detritus in open woodland)	Z_Glet (Glacier)

- *European Environment Agency (EEA):* In order to be able to mask out the agricultural areas from the wet snow map (see section 4.2.3 on page 32), the Coordination of Information on the Environment (CORINE) data set from 2006 was used (European Environment Agency, 2007).
- *Federal Statistical Office (BFS):* To investigate the influence of forest cover in connection with the SAR backscatter of wet snow, the forest type classification (*Waldmischungsgrad 1992*, short: WMG1992) was used. The data set represents the state as of 1992 and differentiates between five forest types and the forest free case (Swiss Federal Statistical Office, 2004). The appropriate spatial resolution (25 m/100 m) was used, for the pixel spacing of each satellite data set.

3.6. Developed Software

Almost all the data processing and calculation steps as well as the plots and charts created by the author were programmed and executed in Matlab (R2012a/R2012b) from The MathWorks,

Inc., while most of the geoprocessing (e.g. image resampling operations, two-dimensional transformations) were scripted in Python 2.7, using ESRI's ArcPython interface for ArcMap Versions 10.1/10.2.1. Additionally, ArcMap was used to resample/project/calculate the aspect/slope as well as the lake and agriculture masks described in section 3.5.

4. Methods

The workflow of the thesis is presented in this chapter. A delineation of the selection process of IMIS stations is first presented, followed by a description of the wet snow retrieval algorithm based on the paper from Nagler & Rott (2000). The criteria used to define dry reference scenes are then explained and the masks are developed. The second part of this chapter presents the theory behind as well as the application of the LRW image processing approach, before concluding with the accuracy assessment methodology of the wet snow detection. In the third part, the steps concerning the isolation of external influencing factors are described.

4.1. Selection of suitable IMIS stations

As the IMIS stations are located in a mountainous environment, not all stations were suitable for analysis of the SAR backscatter, partly due to rough terrain (steep slopes prone to foreshortening and layover) or features within the scene (e.g. small water bodies, buildings, shrubs/forests or streets), as shown in figure 4.1. Additionally, the coordinates of certain stations were only available with an accuracy of ± 50 m. In order to prevent errors induced by inaccurate coordinates or terrain/features on the results of this thesis, each station's coordinates were geolocated using the SWISSIMAGE and swissALTI^{3D} data sets from swisstopo and shifted, before the selection process was run. The main goal of the selection process was to find representative stations with a

(a) Station Taminatal–Schaftäli **(b)** Station Hinterrhein–Unter Surettasee

Figure 4.1: Examples of the surrounding terrain for two IMIS stations. The footprints of 3×3 pixels around the station's location are shown in blue (RS-2) and red (ASAR)

surrounding perimeter of 300 m (3×3 pixels of ASAR), undisturbed by the influences of terrain,

vegetation or man-made objects. Additionally, the station's altitude was taken into account, in order to ensure a distribution over diverse height bands. The subset of stations suitable for this thesis consisted of 38 stations, distributed representatively throughout the Swiss Alps (see figure 3.5 on page 26 and table A.1 on page 98). The stations were distributed over the height bands shown in table 4.1.

Table 4.1: Height distribution of selected IMIS stations

Height band [m]	Number of stations
$< 1\,700$	6
1 700 - 2 099	8
2 100 - 2 399	8
2 400 - 2 699	9
$\geq 2\,700$	7

4.2. Discrimination of wet snow

Radar-based discrimination of wet snow from dry snow is typically based on the difference in dielectric properties caused by the liquid water within the snow pack (see section 2.3.2) and was described by Nagler & Rott (2000). The discrimination between wet and dry snow is of importance for this thesis, since it provides information regarding the state of the snow pack.

4.2.1. Algorithm

The algorithm presented by Nagler & Rott (2000) and Piesbergen et al. (1995) was developed for the application on C-band European Remote Sensing Satellite (ERS) 1/2 and RADARSAT imagery, and proved to be feasible as well for scenes from ASAR as shown by Nagler & Rott (2005).
As a first step, feasible dry reference images need to be defined. According to Nagler & Rott (2000, 2005) these consist of either snow free summer images, or images acquired in winter with dry snow. In both of these cases, surface scattering from the snow-ground interface dominates, in contrast to the snow melt case (see section 2.3.3 on page 14). If possible, dry reference scenes should be temporally as close as possible to the scenes they are compared with. Additionally, the incident angle should agree as good as possible.
Once the reference scenes have been selected, the wet snow mapping algorithm can be applied

pixel by pixel as follows (after Nagler & Rott, 2000):

Data: Dry reference scene, wet snow scene, LIM

Result: Binary wet snow mask

if $(pixel == Layover\ or\ pixel == Shadowing\ or\ \theta_i < 17^\circ\ or\ \theta_i > 78^\circ)$ **then**
| $WetSnowMask == NaN \longrightarrow$ snow mapping not possible

else if $pixel_{ws}\text{-}pixel_{ref} < TR$ **then**
| $WetSnowMask == 1 \longrightarrow$ wet snow

else
| $WetSnowMask == 0 \longrightarrow$ dry snow/snow free

end

Algorithm 1: Wet snow classification algorithm (Nagler & Rott, 2000)

As a value for TR, Nagler & Rott (2000) found a threshold of -3 dB to be appropriate for ERS 1/2 and RADARSAT scenes, which holds true as well for the Envisat ASAR case (Nagler & Rott, 2005). As visible in the algorithm, Nagler & Rott (2000) defined a lower and upper boundary for incidence angles θ_i of 17° and 78°. This condition was investigated for all 330 ASAR scenes over flat areas of 1 km² (see table 4.2). As can be seen in figure 4.2, the ASAR scenes fulfill the condition of the algorithm. Additionally, the areas with layover or shadowing in the GTC and RTC scenes were reclassed to NaN in Matlab, thus having no impact on the final result, as $\mathbb{R} - NaN = NaN$ and $NaN - \mathbb{R} = NaN$.

Table 4.2: Reference areas for retrieval of θ_i (coordinates in CH1903)

Place name	Coordinates UL corner [m]	Coordinates LR corner [m]
Utzensdorf North	610 000/222 100	611 000/221 100
Linthebene	714 400/228 600	715 400/227 600
Piano di Magadino	717 000/114 000	718 000/113 000
Plaine de l'Orbe	531 000/171 000	532 000/170 000
Gürbetal	606 000/185 000	607 000/184 000
Chablais	559 000/134 000	560 000/133 000
Altstätten (SG)	762 000/250 000	763 000/249 000
Ober Vinschgau	837 000/179 500	838 000/178 500

4.2.2. Identification of reference scenes

In order to find suitable dry reference scenes, the criteria mentioned in section 4.2.1 on the preceding page were taken into account as were meteorological data. A dry reference scene was selected for each year, giving a reasonably small temporal difference. To address the similarity of the orbit parameters, a reference scene was attributed to all scenes with the same track. If there was no suitable reference for a given track, a dry scene with the smallest difference in

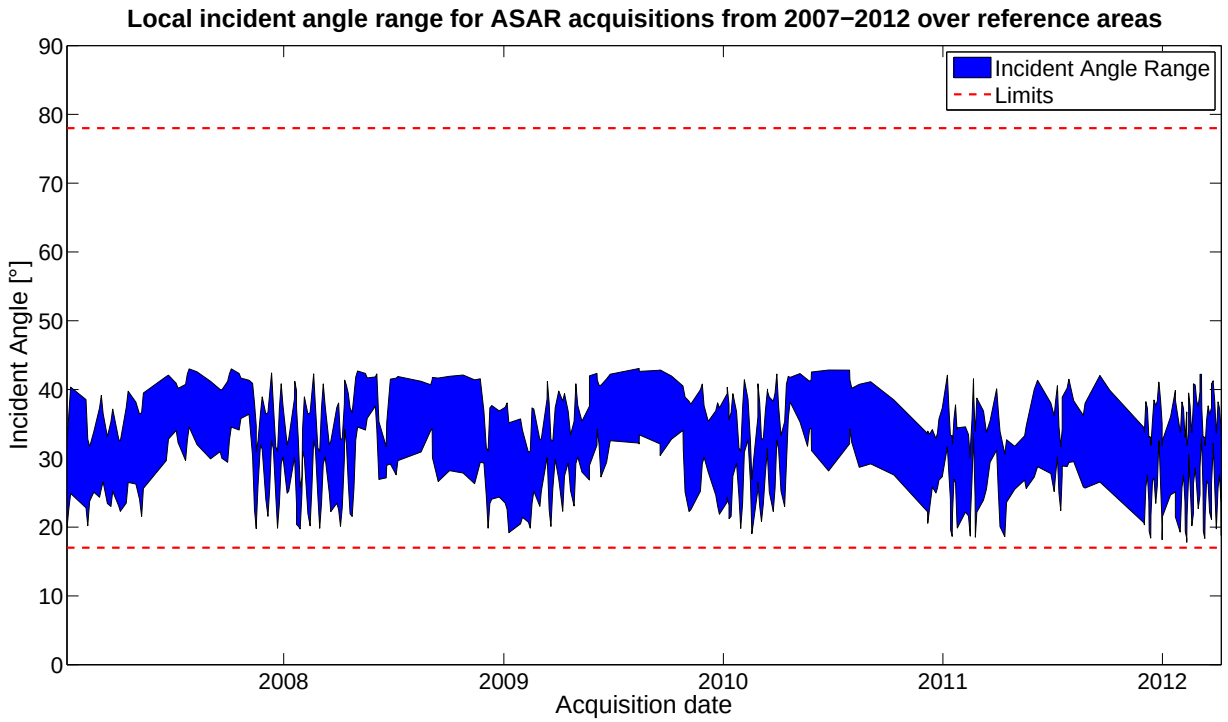

Figure 4.2: Incident angle range over reference areas for ASAR scenes from 2007–2012

orbital parameters (based on the incident angles gained over the reference areas described in table 4.2) was selected. In order to ensure dry conditions, the temperature profile during the course of a year was investigated for different regions (see figure 4.3) and height levels. For extended periods of time, when the temperature was below 0° C, the corresponding scenes were inspected visually regarding their usability as a dry reference. A sample plot for the canton Grisons (region 4) is shown in figure 4.5.

4.2.3. Masking

As shown by Veitinger (2010), a post-processing of the result is necessary for better results due to unrelated changes in backscatter. Therefore, water bodies as well as agricultural and residential areas were masked out of the resulting wet snow product. The water bodies mask was extracted from the VECTOR25 data set (including bodies of water with a surface >0.4 km²), as was the mask for residential areas. Since changes in backscatter can also be caused by e.g. agricultural areas (Caves et al., 1999), a mask was created using the 2006 CORINE data set, merging together all eleven types of agricultural surface (see section 3.5 on page 25). The possibility of wet snow detection in forests is covered extensively in the literature (e.g. Baghdadi et al., 1997; Caves et al., 1999; Piesbergen, 2001), unanimously stating that a detection of wet snow is not possible in areas

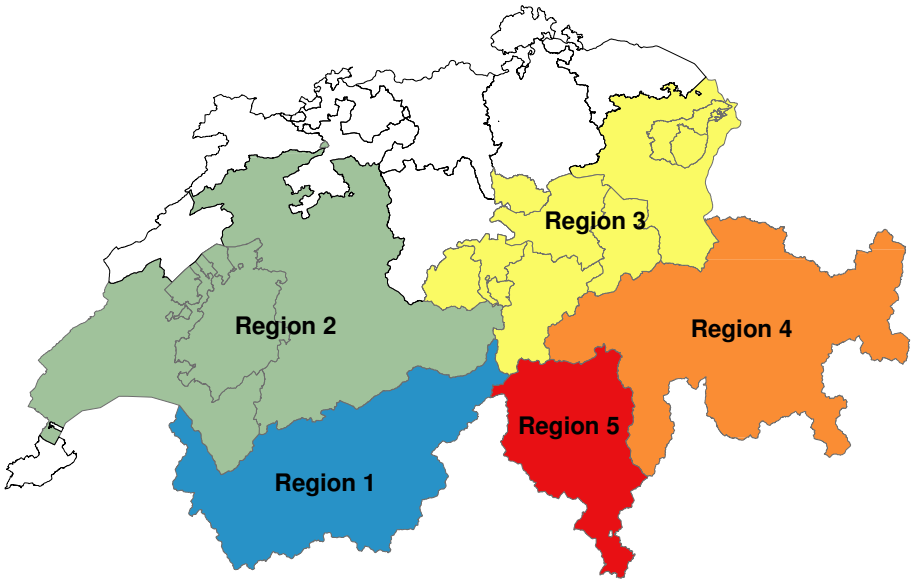

Figure 4.3: Allocation of regions in Switzerland

with dense forest cover, even though a proposition has been made by Koskinen & Hallikainen (1997) to overcome this problem. Since this algorithm is difficult to apply due to the high number of reference images needed (Malnes & Guneriussen, 2002), forested areas were masked out as well, using the forest type classification data set from the Federal Statistical Office (BFS). All four masks were binary (0/1): they only excluded data, leaving the rest of the data unchanged.

4.2.4. Algorithm application

The application of the wet snow mapping algorithm presented on page 31 as well as the masking was scripted and carried out in MATLAB. The algorithm results were saved in two different forms: firstly as a binary wet snow mask, using the -3 dB threshold given in Nagler & Rott (2000) and secondly in a continuous form, with the resulting dB difference stored as pixel values. The latter was done in order to retain the additional information within the exact values as well as to be able to redefine the threshold value during the course of the analysis.

4.3. Local Resolution Weighting (LRW)

Although areas suffering from layover and shadowing effects did not influence the result of the wet snow classification as a result of the *NaN* classification mentioned in section 4.2, there is an interest to not only address the above-mentioned effects, but also to reduce noise within the

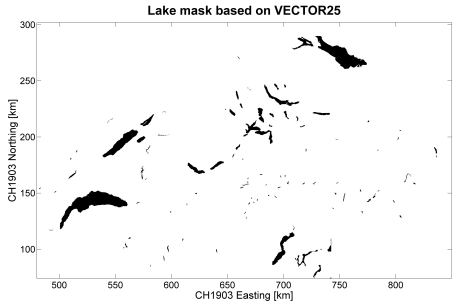

(a) Lake mask based on VECTOR25 data set

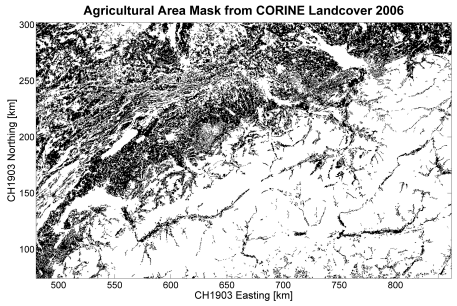

(b) Agriculture mask based on CORINE Landcover 2006

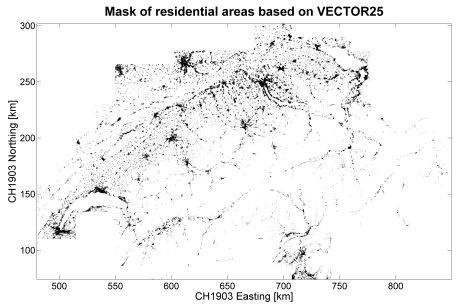

(c) Mask for residential areas based on VECTOR25 data set

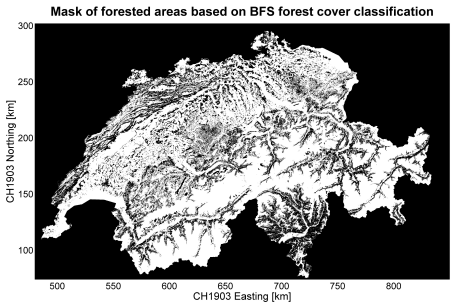

(d) Mask for forested areas based on the BFS forest type classification

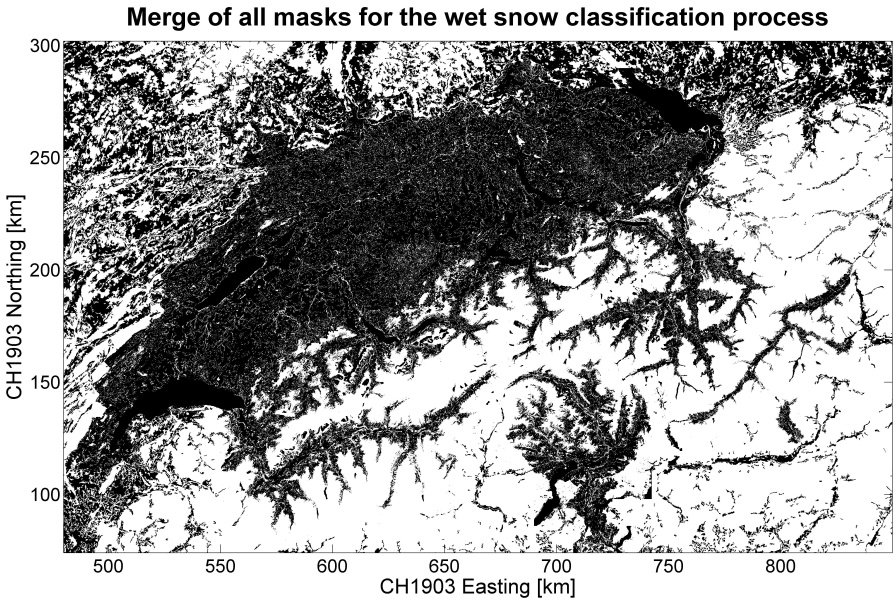

(e) Merge of all masks applied on wet snow detection algorithm

Figure 4.4: Masks applied to wet snow detection algorithm (black areas excluded from result)

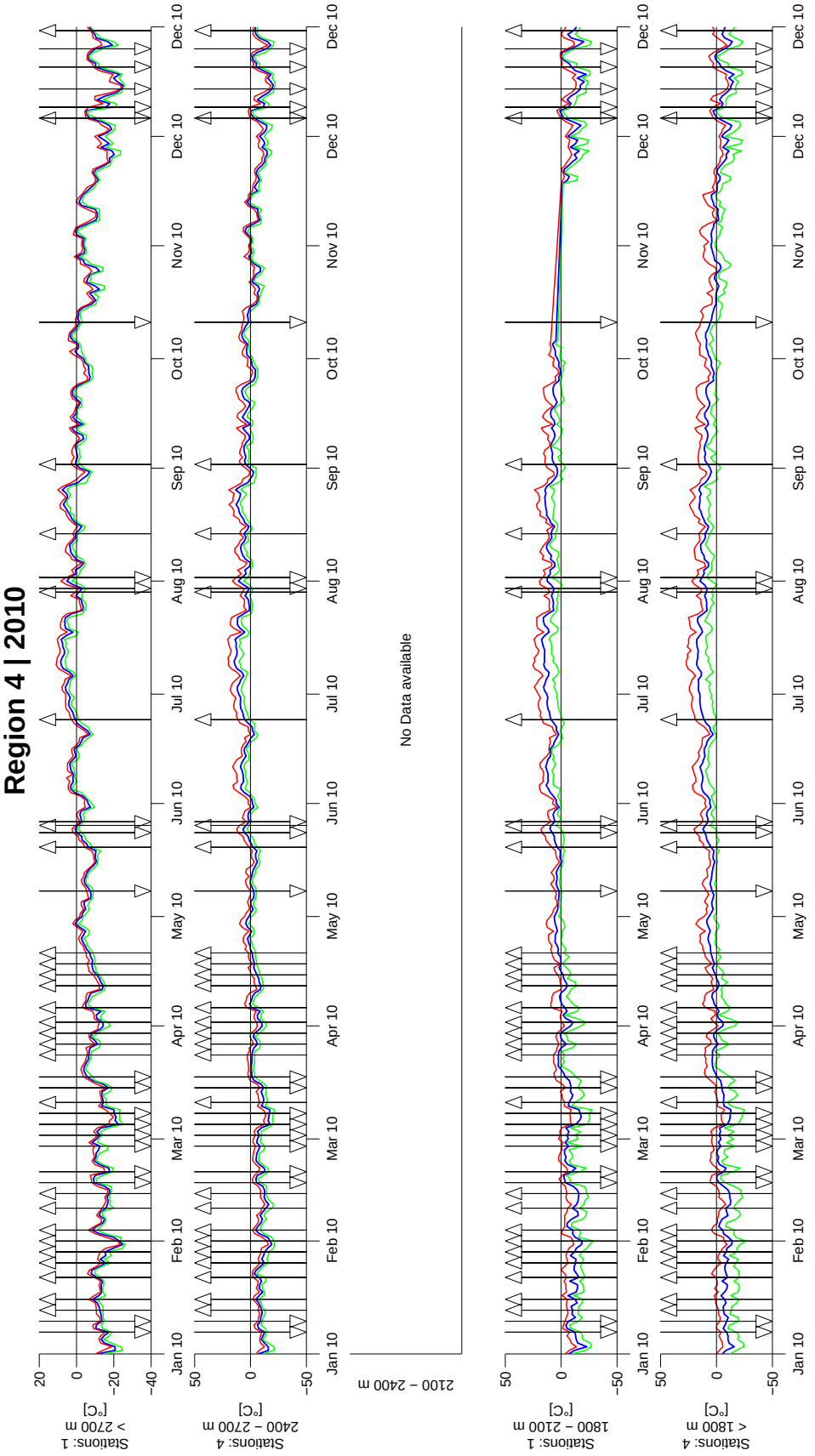

Figure 4.5: Temperature plot for the canton of Grisons in 2010. The temperature data was retrieved from the Climap-net database. The arrows mark ASAR image acquisitions with the arrow direction denoting the orbit configuration (up→ascending, down→descending). The green/blue/red lines mark the daily minimum/mean/maximum temperatures.

scene. A first approach is the so called Optimal Resolution Approach (ORA) that combines SAR data from two crossing orbits of the same day, choosing each pixel on the basis of the highest available resolution (Small et al., 2004; Piesbergen et al., 1997). This approach was extended by Small et al. (2004) by exchanging the boolean pixel choice to fuzzy set theory, using the inverse local resolution as a weight for each pixel when compared to the other available images in the subset (Small et al., 2010). This process, called Local Resolution Weighting (LRW), results in a much more homogeneous spatial resolution without applying masks; only areas affected by shadowing are not considered (Small et al., 2010). In order for the LRW approach to be feasible, the temporal resolution of the SAR scenes need to be sufficiently high, otherwise the differences between the scenes will cause a temporal blurring of the composite image.

4.3.1. Theory

As mentioned above, a subset of RTC images with a high temporal resolution and diverse incidence angles are required for the LRW approach. Ideally, the orbit configuration differs (ascending/descending) within the selected subset to minimize the areas with shadowing, foreshortening or layover (Small et al., 2010). Since the illuminated *area* per pixel is known for each RTC image, and it is inversely proportional to the local *resolution*, its value can be used as a weighting coefficient. As areas in radar shadow do not have a value for illuminated area, the respective pixel value will have a weight of 0 and will thus not influence the LRW image. According to Small et al. (2004) the formula for each grid location with n scenes is as follows:

$$W_i = \frac{1}{A_i} \Big/ \sum_{j=1}^{n} \frac{1}{A_j}; \qquad \gamma_c^0 = \sum_{i=1}^{n} W_i \cdot \gamma_i^0 \tag{4.1}$$

where

W_i = Weight for image i
A_i = Illuminated area for image i
γ_c^0 = Composite backscatter value
γ_i^0 = Backscatter value for image i

Even though the LRW approach comes with trade-offs – a decrease in temporal resolution, as multiple images are required for a single composite image – the result is an image with normalized backscatter as well as an optimal spatial resolution, allowing better thematic interpretation compared to single GTC or RTC products (Small et al., 2004, 2010; Small, 2012).

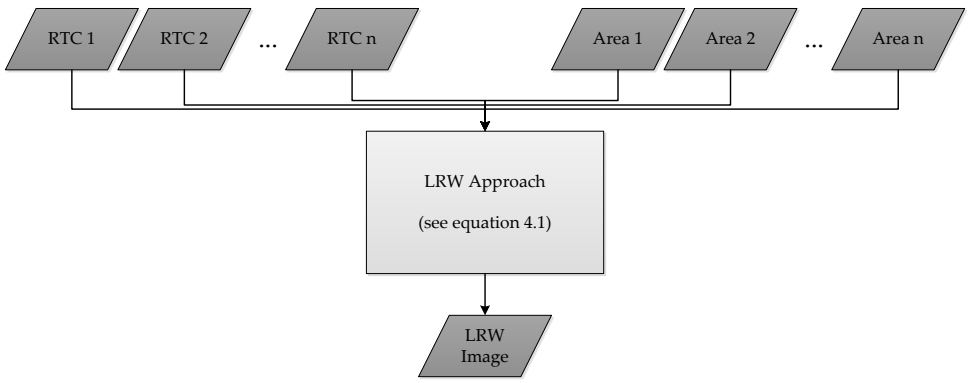

Figure 4.6: LRW image processing steps (adapted from Schaub, 2011)

4.3.2. Wet snow detection with LRW images

The optimized spatial resolution of the LRW image makes it well suited to detect wet snow cover using the algorithm from Nagler & Rott (2000) presented in section 4.2, given a small temporal difference of the image subset used for LRW calculation. In order to find suitable temporal windows for the generation of LRW composites, image statistics for multiple temporal windows were calculated and compared with one another. The goal was to achieve an optimal balance between a high number of images in the subset (if possible with a big areal overlap between ascending and descending image acquisitions) and a small time difference between the scenes. As can be seen in figures B.1a to B.1g on pages 103–109, these requirements could not be fulfilled simultaneously for most of the ASAR time series: with a small time difference, there were usually only few scenes available for the LRW calculation and thus there was no areal overlap available to minimize shadowing, foreshortening or layover. Even with a temporal window of 30 days, there were gaps in the availability of LRW composites with a high areal overlap, and since the snow melt period is normally short-lived, the upper limit for the LRW's temporal baseline was limited to two weeks, since otherwise there would be a mixture of different wetness levels. A careful selection of LRW composites with big areal overlaps was thus necessary for the accuracy assessment described in the following section.

4.4. Accuracy assessment

The SAR wet snow classification accuracy was investigated using both the spaceborne optical imagery (see section 3.2) as well as the measured/modeled parameters gained through IMIS/SNOWPACK (see section 3.3). The assessment was carried out for LRW composites with a

temporal tolerance of five, seven, ten, and fourteen days in order to investigate the influences of temporal baseline and image availability.

4.4.1. Comparison of SAR wet snow classification with optical remote sensing imagery

The LRW composites were compared to the available optical snow cover products on a pixel-by-pixel basis. Due to the differences in classification between the optical snow cover products, the values were recoded according to the scheme shown in tables 4.3, 4.4, and 4.5. As SAR differentiates between the presence and absence of wet snow, but cannot determine the presence of dry snow solely based on the SAR data (see section 6.1.2), only the user's accuracy could be assessed for all comparisons using the following formula (Lillesand et al., 2008):

$$\textit{User's accuracy} = \frac{SAR_{ws} \cap O_s}{(SAR_{ws} \cap O_s) \cup (SAR_{ws} \cap O_{ns})} \tag{4.2}$$

where

SAR_{ws} = Pixels classified as *wet snow* in SAR image
O_s = Pixels classified as *snow* in optical remote sensing image
O_{ns} = Pixels classified as *no snow* in optical remote sensing image

The classification accuracy was assessed for the five, seven, ten, and fourteen day LRW composites. Since the extents of both the optical as well as the SAR scenes differed within the variety of image acquisitions, the user's accuracy was calculated not only for the comparison of a single LRW composite against an optical satellite image, but also for all of the available composites within the given time frame.

Table 4.3: Recoding scheme of the AVHRR snow cover product

Original value	Cover type	Recoded value
0	No snow	0
100	Snow	1
200	Water	NaN
250	Cloud	NaN
255	No data	NaN

Table 4.4: Recoding scheme of the Landsat 7 snow cover product

Original value	Cover type	Recoded value
0-0.399	FSC < 40%	0
0.40-1	FSC $\geq$ 40%	1
No data	Cloud/No data	NaN

Table 4.5: Recoding scheme of the MODIS snow cover product

Original value	Cover type	Recoded value
0-39.9	FSC < 40%	0
40-100	FSC $\geq$ 40%	1
No data	Cloud/No data	NaN

4.4.2. Investigation of external influencing factors

In addition to the accuracy assessments described above, differences in the distribution of three environmental variables between the wet snow classification using LRW composites and the optical reference scenes have been assessed. Therefore, the distribution of the characteristics of different variables was calculated for both products (see table 4.6). The formula used to calculate the distribution differences followed:

$$Distribution\ Var_{x,y_{Reference}} = \frac{SAR_{ws} \cap (O_{ns} \cup O_s) \cap Var_{x,y}}{SAR_{ws} \cap (O_{ns} \cup O_s)} \tag{4.3}$$

$$Distribution\ Var_{x,y_{SAR}} = \frac{SAR_{ws} \cap O_{ns} \cap Var_{x,y}}{SAR_{ws} \cap O_{ns}} \tag{4.4}$$

$$Distribution_{Difference} = Distribution\ Var_{x,y_{Reference}} - Distribution\ Var_{x,y_{SAR}} \tag{4.5}$$

where

$Var_{x,y_{Reference/SAR}}$	=	Variable x with characteristic y in the reference/SAR scene (see table 4.6)
SAR_{ws}	=	Pixels classified as *wet snow* in SAR image
O_s	=	Pixels classified as *snow* in optical remote sensing image
O_{ns}	=	Pixels classified as *no snow* in optical remote sensing image

Table 4.6: Assessed environmental influencing factors on wet snow detection

Variable	Characteristics								
Aspect	N (315°-45°)		E (45°-135°)		S (135°-225°)		W (225°-315°)		Flat
Slope [°]	0-10	10-20	20-30	30-40	40-50	50-60	60-70	70-80	80-90
Ground Cover	Bedrock		Detritus		Glacier		Other		

4.4.3. Analysis of the relationship between liquid water within the snow pack and SAR backscatter

As the SAR backscatter signal is strongly influenced by the presence of liquid water within the snow pack (see figure 2.7), the relation between the liquid water and the radar backscatter was investigated. As described in section 3.3.1, layered information on the LWC were provided for the subset of 38 stations in the Swiss Alps. Since LWC values are provided as a percentage, the value itself does not describe the *amount* of liquid water in the snow pack. In combination with information about the snow pack's density, the SWE could be calculated, although SWE values describe the combined amount of water from snow as well as liquid water within the snow pack. In order to retrieve an absolute number describing the liquid water in the snow pack, a new quantity dubbed Liquid Water Volume (LWV) was calculated using the information given by the layered LWC data set. The point modelings of LWC were therefore assumed to have taken place over an area of 1 m². As the layer thickness and the LWC were known, the LWV could be calculated using the formula

$$LWV_i = 100 \cdot 100 \cdot LH_i \cdot LWC_i \; [cm^3] \tag{4.6}$$

where

LWV_i = LWV of layer i [cm³]
LH_i = Height of layer i [cm]
LWC_i = LWC of layer i [%]

The SAR backscatter values were retrieved for each station and scene (VV for ASAR, VV and VH for RS-2), averaging the backscatter values over different window sizes (1×1, 3×3, 5×5, and 7×7 pixels). Regarding the LRW composites, the temporal tolerance was varied between 5 and 14 days. In addition to the satellite data, snow height and multiple LWV values were retrieved, such as the snow pack's total LWV and the LWV sum for the uppermost 10/20/30/40/50/60/70/80/90 cm of snow with an LWC>0%. The relationship between LWV and the backscattered signal was then assessed by calculating the correlation coefficient as well as executing a regression analysis for the different combinations of the variables. For the regression analysis, a linear regression

was executed using MATLAB to model the relationship between the dependent variable *SAR backscatter* and the explanatory variable *LWV*. For the correlation coefficient *Spearman's rho* was used due to the non-normal distribution of both, the dependent and the explanatory variable.

4.4.4. Comparison of SAR wet snow classification with IMIS station data

As a second accuracy assessment, the SAR wet snow classification was compared against the IMIS station parameters snow height and LWC. To account for possible errors induced by noise in the SAR wet snow classification, the assessment was carried out with differently sized windows surrounding the 38 selected stations at altitudes between 1 600 and 3 000 meters above sea level (see figure 3.5/table A.1). While the comparison against snow height values allowed a plausibility check of the wet snow detection algorithm (if a pixel was classified as wet snow, the snow height had to be >0 cm at the time of image acquisition), the layered information about the LWC within the snow pack could be used to verify the wet snow classification using SAR imagery.

For the accuracy assessment of the wet snow mapping algorithm, a confusion matrix was calculated including the two possible cases *wet* and *dry/no snow* for the SAR derived classification, and *snow-covered* as well as *snow free* for the snow height values. For the comparison against the LWC values derived from the SNOWPACK model, the SAR based wet snow classification was compared against the maximum LWC value for the whole depth of the snow pack. These analyses returned user's, producer's or overall accuracy, depending on the differentiation ability between dry and wet conditions in the reference. The latter two statistical values were calculated according to the following formulae (Lillesand et al., 2008):

$$\textit{Producer's accuracy} = \frac{SAR_{ws} \cap Ref_{ns}}{(SAR_{ws} \cap Ref_{ns}) \cup (SAR_{ns} \cap Ref_{ns})} \tag{4.7}$$

$$\textit{Overall accuracy} = \frac{(SAR_{ws} \cap Ref_{ws}) \cup (SAR_{ns} \cap Ref_{ns})}{SAR_{ws} \cup SAR_{ns} \cup Ref_{ws} \cup Ref_{ns})} \tag{4.8}$$

where

SAR_{ws} = Pixels classified as *wet snow* in SAR image
SAR_{ns} = Pixels classified as *no/dry snow* in SAR image
Ref_{ws} = Pixels classified as *wet snow* in reference
Ref_{ns} = Pixels classified as *no snow* in reference

As in section 4.4.3 on page 40 the comparisons were carried out for LRWs with temporal differences of 5, 7, 10, and 14 days, as well as for different areas surrounding the IMIS stations (1×1, 3×3, 5×5, and 7×7 pixels).

5. Results

This section presents the results of the analyses made with the different methods described in section 4 with the scope of answering the research questions. In section 5.1, the classification accuracy of the wet snow discrimination algorithm of Nagler & Rott (2000) are compared against different optical snow cover products. In section 5.2 the classification results presented in section 5.1 are controlled for systematic biases regarding the influence of slope, terrain aspect, and underlying soil cover with the data sets described in section 3.5 using the methodology presented in section 4.4.2. Section 5.3 covers the plausibility of the SAR wet snow cover classification by comparing it to the IMIS station measurement and model output values, before investigating the SAR backscatter dependency in relation to snow wetness values derived from IMIS stations.

5.1. Classification accuracy assessment of SAR wet snow mapping against optical products

In the following subsections, the classification accuracy of both ASAR and RS-2 LRW composites as well as single RS-2 scenes in comparison with snow cover products from AVHRR, LS 7, and MODIS (see figure 3.1) is presented.

5.1.1. ASAR wet snow maps

For the comparison of the ASAR LRW wet snow maps with the optical snow cover products the pixel spacing of the latter was adjusted to match the 100 m pixel spacing of the ASAR LRW composites. The user's accuracy values were calculated using formula 4.2 on page 38.

Figures 5.1, 5.2 and 5.3 illustrate the performance of the ASAR wet snow maps against AVHRR, LS 7 and MODIS snow products respectively. In each figure, the solid lines show the mean accuracy of all scenes with a given temporal window while the dashed lines denominate the lowest/highest classification accuracy respectively. Since some scenes only had a small number of pixels that were classified in both the ASAR LRW as well as the optical reference product resulting in outliers, only classifications with a total of more than 30 000 pixels were used to define the minimum/maximum values.

Comparison against AVHRR snow cover

The classification accuracy of ASAR LRW composites with different temporal windows against AVHRR snow cover products (see table 3.4) is shown in figure 5.1 on the following page.

The overall user's accuracy for the ASAR LRWs with an areal overlap between the ascending and descending scenes (solid red line) was highest for the 7 day LRW with an accuracy of 95.4% and lowest for the 10 day LRW with 92.13%. The 5 day LRW had a user's accuracy almost as high as for the 7 day composite with 94.73%, while the 14 day LRW composite was only marginally higher than the one with a temporal window of 10 days with a user's accuracy of 92.77%. The highest user's accuracies for the different temporal windows consistently reached values of >94% and peaking out at 96.48% for the 14 day composite, whereas the lowest accuracies dropped down to around 88% for the 10 and 14 day ASAR LRWs after reaching accuracies >94% for the 5 and 7 day composites.
Overall user's accuracy values for ASAR LRWs without an areal overlap were constantly lower when compared to the overlapping case. The classification accuracy for the 5 day ASAR LRW was 89.81%, before decreasing to 85.59% when comparing the 7 day composite to the AVHRR snow cover product. With 87.66% and 86.02% the values for the 10 and 14 day ASAR LRWs were almost equal. The individual maxima for the composites without an areal overlap lay between 94.47% (10 day ASAR LRW) and 99.58% (14 day composite), whereas the lowest accuracies for the non-overlapping case were around 85% for the 5 and 7 day LRWs and 85% for the 10 and 14 day cases.

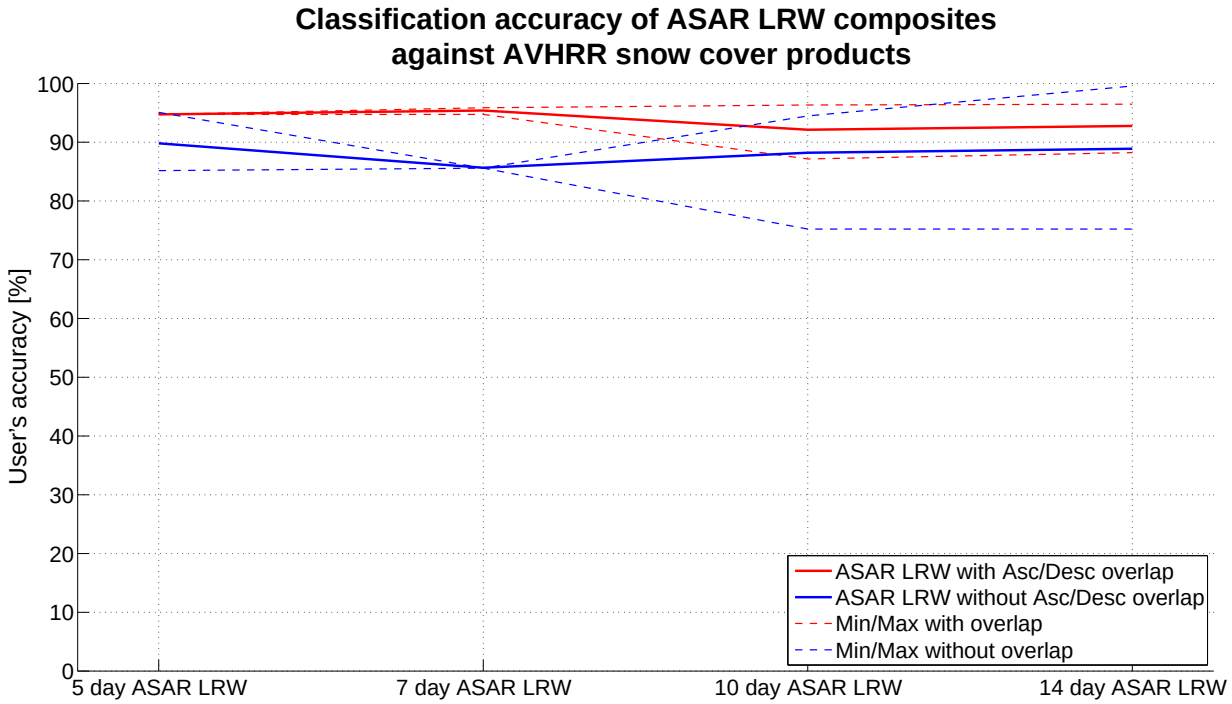

Figure 5.1: Classification accuracy of ASAR LRW composites compared with AVHRR snow cover products

Comparison against LS 7 fractional snow cover

Figure 5.2 on the next page shows the classification accuracies for different temporal windows of ASAR LRW composites in comparison with LS 7 FSC products (see table 3.5).
The overall user's accuracy for the ASAR LRW composites with an areal overlap of ascending/descending scenes had a minimum of 86.46% for the 7 day composite and a maximum with a temporal window of 5 days and a value of 90.01%, with the values for the 10 and 14 day ASAR LRWs lying in between with accuracies of 86.60% and 87.24% respectively. When comparing the individual ASAR LRW composites with an areal overlap to LS 7 FSC products for each temporal window, the maxima showed constant values of 90-91%, whereas the minima exhibited a slightly deceasing tendency in classification accuracy, dropping from 90.01% (5 day LRW) to 85.50% (7 day LRW), before plateauing at around 85%.
As was already the case when comparing the ASAR LRWs to AVHRR, the composites without an areal overlap exhibited slightly lower user's accuracies when compared to those with an overlap between ascending and descending scenes. The values ranged from 76.30% (14 day LRW) to 84.23% (7 day LRW), with the 5/10 day composites' values at 83.53% and 81.52%. Regarding the individual maxima for each temporal window, the accuracy was 85.06% for the 5 day ASAR LRW and then reached 85.58% and 86.57% for the 7 and 10 day composites. Since only small regions were covered with non-overlapping LRWs, no maxima and minima could be defined for the 14 day LRW with a sample size of >30 000 pixels. The remaining individual minima of the user's accuracy ranged from 82.18% in case of the 10 day ASAR LRW to 85.58% for the 7 day composite scene. This was the same value as for the individual maximum, as it was the only scene with more than 30 000 classified pixels and a temporal window of 7 days. As is visible in figure 5.2 on the following page, the individual minima were partly higher compared to the overall accuracies. This is due to the 30 000 pixel restriction, since only one out of three ASAR LRW scenes surpassed this number, whereas the other two scenes were all contributing to the overall accuracy.

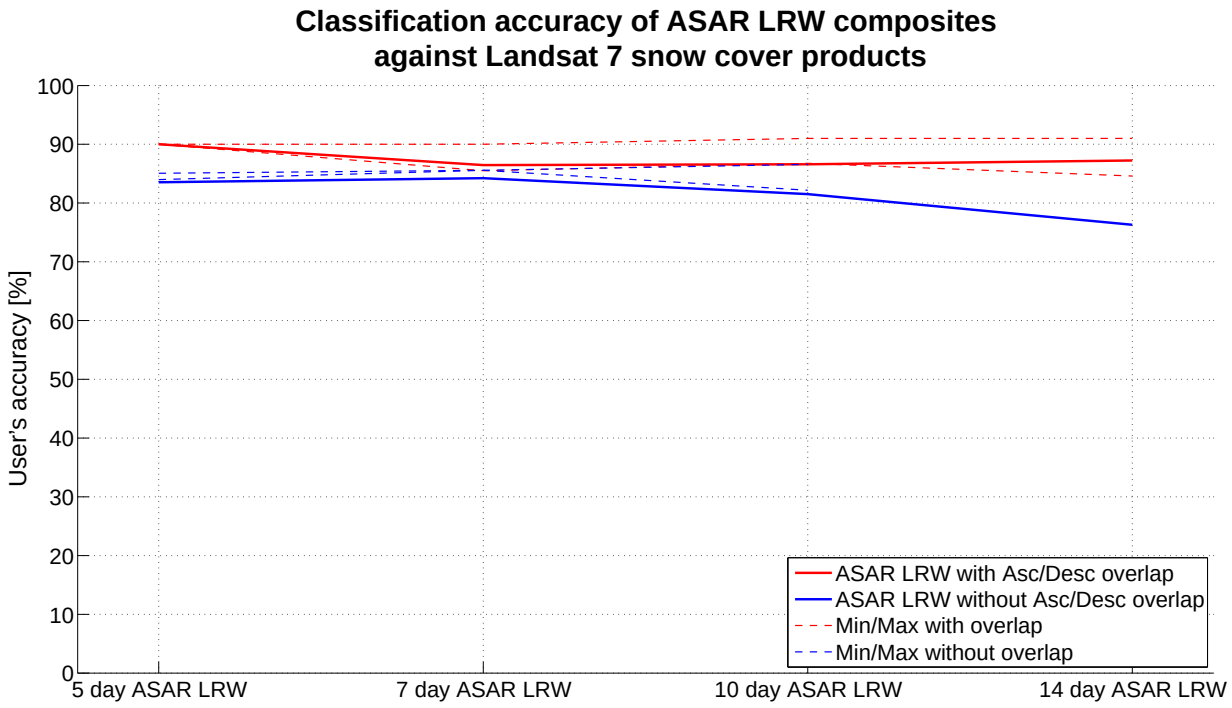

Figure 5.2: Classification accuracy of ASAR LRW composites compared with Landsat 7 fractional snow cover products

Comparison against MODIS fractional snow cover

The classification accuracy of ASAR LRW composites with different temporal windows against MODIS snow cover products (see table 3.6) is shown in figure 5.3 on the next page.

The overall user's accuracy for ASAR LRWs with an areal overlap of the contributing ascending and descending scenes could only be calculated for the 7, 10, and 14 day LRWs, as there was no constellation of ASAR scenes with both ascending and descending orbits within the defined 5 day time frame. Therefore, also individual minima and maxima were inexistent for LRW composites with an areal overlap. The remaining temporal windows exhibited classification accuracies of 87.38%/90.35%/90.67% for the 7/10/14 day case. The individual maxima for the available three temporal windows were close to the overall user's accuracies, with a maximum at 92.95% for the 14 days LRW. As for the maxima, the minima deviated only slightly from the overall accuracies, with values ranging from 86.74% to 87.38%, with the latter equaling the overall and individual maximum of the 7 day composite, since its overall user's accuracy was only calculated from a single LRW.

For the ASAR LRWs without areal overlap there were scenes available for all four temporal windows. The overall user's accuracy was generally lower compared to the areal overlapping case. The 5 and 7 day composites had the highest accuracy with 87.57% and 87.53% respectively, whereas the 10 day ASAR LRWs had a small decrease in terms of classification accuracy with

81.31%. The lowest value was calculated for the 14 day composite with 75.84% user's accuracy. In terms of individual scenes, the maxima only showed small differences for the different temporal windows with values ranging from a low of 83.76% (10 day LRW) to a maximum of 89.57% (temporal window of 7 days). The individual minima showed a strong decrease in classification accuracy between the 5 day ASAR LRW with an accuracy of 85.65% and the 7 day composite (56.16%), before plateauing at 54.63% user's accuracy for both, the 10 and 14 day temporal windows.

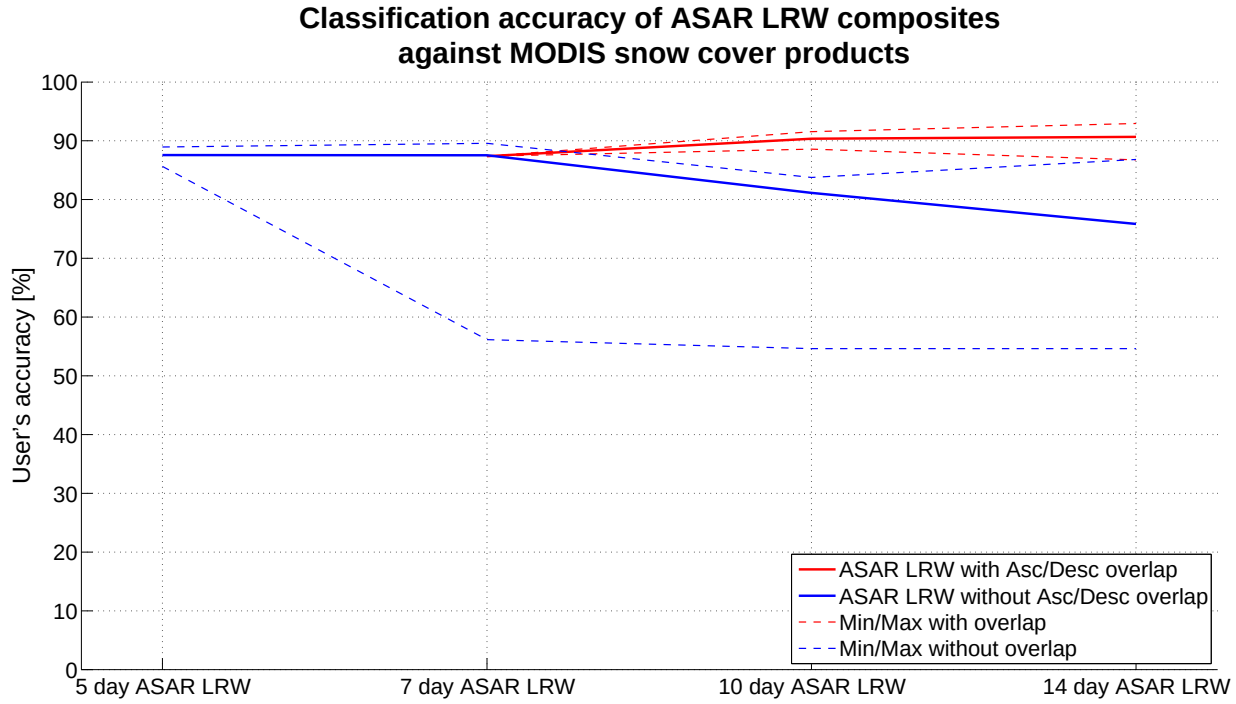

Figure 5.3: Classification accuracy of ASAR LRW composites compared with MODIS fractional snow cover products

5.1.2. RS-2 wet snow maps

With its high resolution, the classification accuracy of RS-2 scenes against the optical remote sensing snow cover products was of particular interest for this study, even though the number of possible comparisons was limited due to the number of available RS-2 scenes (see section 3.1.2). The number of available scenes was further reduced as a result of the snow classification algorithm's need for a dry reference scene (2012-02-28) and the creation of an LRW composite for the two scenes from 2010-04-26/2010-04-27. Therefore, the creation of diagrams as in section 5.1.1 on page 43 was not feasible. The confusion matrices will be presented instead. The data shown was based on an intersection of the classification results from both, VV and VH polarizations,

thus only those pixels were flagged as *wet snow* where both polarizations were classified as *wet snow*.

Comparison against AVHRR snow cover

The comparison of RS-2 wet snow classifications with AVHRR snow cover products showed only minor differences in user's accuracy between the years 2010 and 2012. As visible in tables 5.1 to 5.3, the accuracy was highest for the comparison of the RS-2 LRW wet snow mask (based on the two scenes from April 2010) with the 2010-04-26 AVHRR scene with an accuracy of 93.64%. The agreement with the AVHRR snow cover product from 2010-04-27 (one day later) was lower with 89.24%, possibly since the former AVHRR scene had higher cloud cover (see table 3.4), thus increasing the number of *NaN* pixels. The comparison of the RS-2 wet snow mask from 2012-03-23 to the AVHRR snow cover product of the same date showed a slightly higher user's accuracy compared to the 2010-04-27 case with 90.75%. This AVHRR scene had almost no cloud cover, while the areal cover of Switzerland dropped from 100% for the 2010-04-26/2010-04-27 scenes to 68.24% in March 2012.

Table 5.1: Confusion matrix for the comparison of RS2 LRW WSM (2010-04-26/2010-04-27) with AVHRR Snow Cover (2010-04-26)

		AVHRR Snow Cover 2010-04-26		
RS2 LRW WSM 2010-04-26/27		Snow	No Snow	*NaN*
	Wet snow	9 436 720	641 015	14 319 151
	No/dry Snow	5 444 276	2 883 854	26 437 720
	NaN	6 518 153	9 744 326	59 550 785
	User's Accuracy		93.64%	

Table 5.2: Confusion matrix for the comparison of RS-2 LRW WSM (2010-04-26/27) with AVHRR Snow Cover (2010-04-27)

		AVHRR Snow Cover 2010-04-27		
RS-2 LRW WSM 2010-04-26/27		Snow	No Snow	*NaN*
	Wet snow	8 556 080	1 031 304	11 987 424
	No/dry Snow	3 538 089	3 043 736	15 231 775
	NaN	5 505 830	22 273 702	91 027 259
	User's Accuracy		89.24%	

Table 5.3: Confusion matrix for the comparison of RS-2 WSM (2012-03-23) with AVHRR Snow Cover (2012-03-23)

		AVHRR Snow Cover 2012-03-23		
RS-2 WSM 2012-03-23		Snow	No Snow	*NaN*
	Wet snow	1 912 592	194 858	1 588 794
	No/dry Snow	11 986 663	10 232 878	17 472 623
	NaN	6 665 995	51 279 885	33 641 712
	User's Accuracy		90.75%	

Comparison against LS 7 fractional snow cover

Only one comparison could be carried out against the LS 7 FSC product, as there were only two LS 7 FSC products within a few days to an available RS-2 scene, namely on 2012-03-22 and 2012-03-24. As mentioned in section 3.1.2 on page 18, these two FSC products were merged into a single scene, dubbed *2012-03-23* (see table 3.5). The lack of further matches between RS-2 and LS 7 acquisitions is highly unfortunate, as the available pixel resolution were high for both products with a 25 m pixel spacing for RS-2 and 30 m for LS 7.
As shown in table 5.4, the user's accuracy for the comparison of the SAR and the merged LS 7 FSC scenes was 89.27% with approximately 2 000 000 pixels classified as *wet snow* in the RS-2 scene and either *snow* or *no snow* in the MODIS FSC product.

Table 5.4: Confusion matrix for the comparison of RS-2 WSM (2012-03-23) with Landsat 7 FSC (2012-03-23)

		LS 7 FSC 2012-03-23		
RS-2 WSM 2012-03-23		Snow	No Snow	*NaN*
	Wet snow	1 775 105	213 458	1 707 681
	No/dry Snow	12 906 706	7 645 217	19 140 241
	NaN	7 625 255	37 291 674	46 670 663
	User's Accuracy		89.27%	

Comparison against MODIS fractional snow cover

From the MODIS instrument, three FSC scenes that coincide with RS-2 acquisition dates were available, namely 2010-04-26, 2010-04-27, and 2012-03-23. This provided the possibility to assess the wet snow detection algorithm three times, twice against the RS-2 LRW described in section 5.1.2 and once against a wet snow mask derived from the single 2012-03-23 scene.
As shown in tables 5.5 to 5.7, the user's accuracy was low for both comparisons with the RS-2

LRW wet snow mask with 61.80% and 66.70% against the 2010-04-26 and 2010-04-27 MODIS FSC products. In both MODIS reference scenes, the number of pixels classified as *wet snow* in RS-2 and either *snow* or *no snow* in the MODIS scene was very high compared to the AVHRR and LS 7 accuracy assessments. The user's accuracy for the single RS-2 wet snow mask acquired on 2012-03-23 was at 93.80% with about 3 700 000 classified wet snow pixels in the SAR scene (see table 5.7).

Table 5.5: Confusion matrix for the comparison of RS-2 LRW WSM (2010-04-26/2010-04-27) with MODIS FSC (2010-04-26)

		MODIS FSC 2010-04-26		
RS-2 LRW WSM 2010-04-26/27		Snow	No Snow	*NaN*
	Wet snow	15 056 228	9 306 178	34 480
	No/dry Snow	6 359 434	28 339 198	67 218
	NaN	6 861 792	66 197 614	2 753 858
	User's Accuracy		61.80%	

Table 5.6: Confusion matrix for the comparison of RS-2 LRW WSM (2010-04-26/2010-04-27) with MODIS FSC (2010-04-27)

		MODIS FSC 2010-04-27		
RS-2 LRW WSM 2010-04-26/27		Snow	No Snow	*NaN*
	Wet snow	14 368 401	7 173 125	33 282
	No/dry Snow	5 753 832	16 000 394	59 374
	NaN	7 438 043	81 386 649	2 762 900
	User's Accuracy		66.70%	

5.2. Evaluation of external influencing factors on classification accuracy

As stated by Bernier (1991), Nagler & Rott (2000) or Koskinen et al. (2000), several external factors can influence the discrimination of wet snow from dry snow/snow free areas. While in section 5.1 we restricted our analysis to controlled external influence factors, we now want to investigate the influence of these factors on the algorithm's performance.
Positive cover percentage differences represent an underrepresentation of the specific variable's characteristic within the total of misclassified SAR pixels when compared to the distribution

Table 5.7: Confusion matrix for the comparison of RS-2 WSM (2010-03-23) with MODIS FSC (2012-03-23)

			MODIS FSC 2012-03-23		
RS-2 WSM 2012-03-23			Snow	No Snow	*NaN*
		Wet snow	3 465 424	229 064	1 756
		No/dry Snow	25 304 799	14 296 465	90 900
		NaN	17 510 396	71 314 296	2 762 900
		User's Accuracy		93.80%	

of the variable's characteristic over all pixels classified as *wet snow*. Negative cover percentage differences stand for an overrepresentation in the totality of misclassified pixels.

5.2.1. ASAR wet snow maps

In the following section, the influence of the aforementioned external environmental factors is described for the year of 2012. The focus was on 2012 in order to have a common baseline regarding the wet snow classification (i.e. the same dry reference scene used for all ASAR LRWs). Additionally, the dense time series for the spring melting season of 2012 offered an availability of LRWs composites outnumbering the other years.
The plots differed between LRWs with variable temporal windows as well as between LRWs with and without an areal overlap between ascending/descending orbits. As a result of the dense time series in 2012, the lowest areal overlap for the latter case was at 66.7%.

Slope

For the analysis regarding the slope of misclassified pixels (i.e. classified as wet snow in the ASAR LRW, but not within the snow cover extent of the optical reference scene), the terrain's slope was divided into classes with 10° intervals.
For all three different reference products, the curve progression was similar. The amount of pixels with slopes smaller than 10° was overrepresented in the LRW based classification by 0.5% to 20%, whereas slopes between 10° and 30° tended to be underrepresented by 2%–11%. For values from 30° to 70° steepness, the results show differences between the reference products from AVHRR and LS 7/MODIS. While the snow cover product from the former sensor showed an decreasing underrepresentation towards a slope of 70°, the latter two products had a slight tendency towards overrepresentation. The biggest range in cover percentage difference was be found in the ASAR LRW comparison against LS 7 FSC products (see figure 5.4b). For values above of 70° slope, all three comparisons tended towards a cover percentage difference of 0%,

signifying matching values between expected (see equation 4.3) and actual steepness distribution (see equation 4.4).

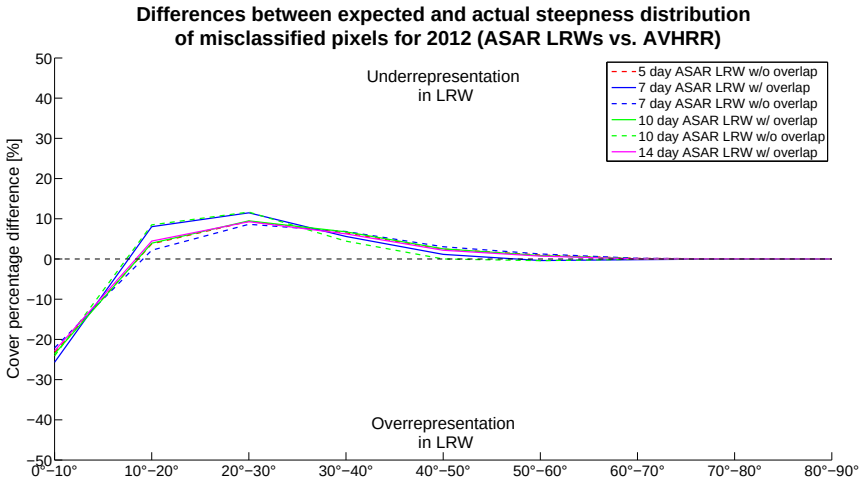

(a) ASAR LRW comparison against AVHRR

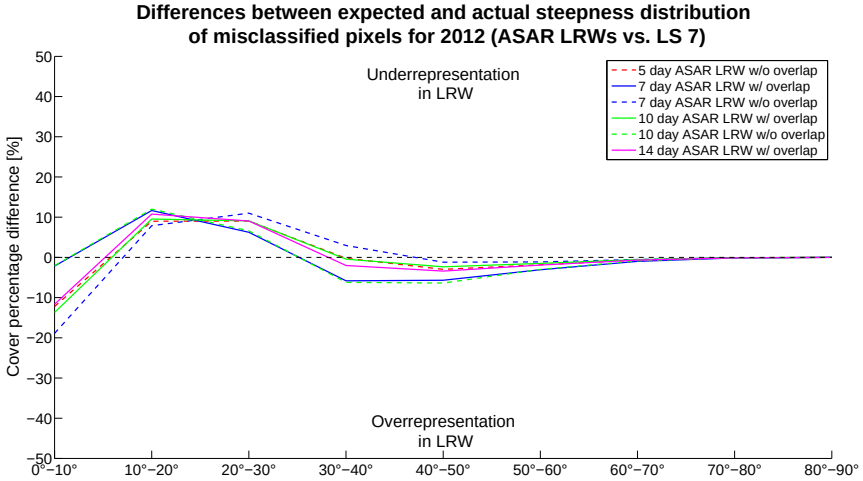

(b) ASAR LRW comparison against Landsat 7

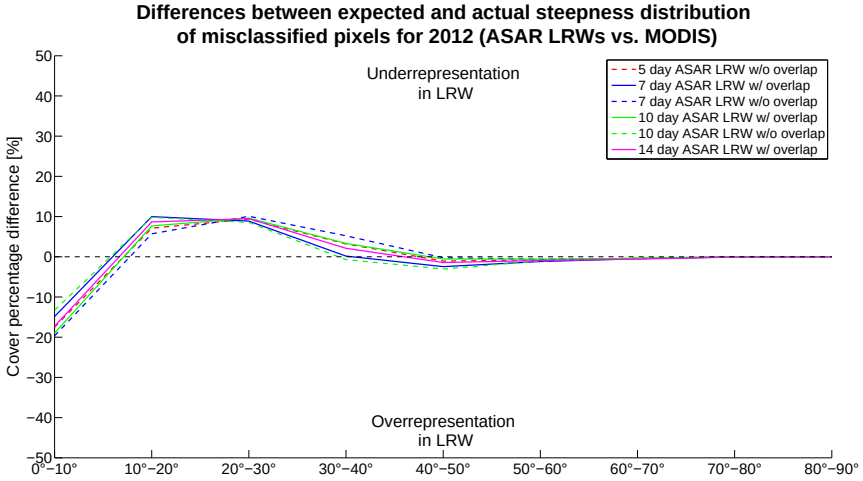

(c) ASAR LRW comparison against MODIS

Figure 5.4: ASAR LRW misclassification dependency on different slopes

Terrain aspect

Regarding the terrain aspect, the aspect values derived from swisstopo's DHM25 data set were grouped into five classes, namely: Flat areas without aspect, as well as northerly, easterly, southerly, and westerly exposed areas (see table 4.6). As was the case when comparing actual to expected slope distribution, the comparison of terrain aspect distribution seems to agree well between the LS 7 and MODIS FSC product, whereas for the AVHRR case there was only a partial agreement. In comparison to the former two snow cover products the ASAR LRWs trended towards an underrepresentation of pixels with a northerly exposition, while the comparison with AVHRR snow cover indicated an overrepresentation of between 1% to 7%. All three products agreed well by indicating an overrepresentation regarding the misclassified pixels with a easterly terrain aspect, exhibiting cover percentage differences between 5% and 14%. The same agreement was found with westerly facing pixels, although in this case the cover percentage difference indicated an underrepresentation for all three reference snow products, ranging from 3% to 16%. In case of a southerly exposition the comparisons did not agree between the three reference snow cover products: for AVHRR, the comparison resulted in an underrepresentation by 5% to 11%, while for LS 7, the values indicated an underrepresentation by approximately the same percentage. The cover percentage difference values for the comparison with MODIS FSC were grouped around 0% difference, indicating an equal distribution between the expected and actual distribution of misclassified pixels regarding terrain aspect (see equations 4.3 and 4.4). For flat surfaces, the resulting cover percentage difference was between -2% and 0.5% for all reference snow products.

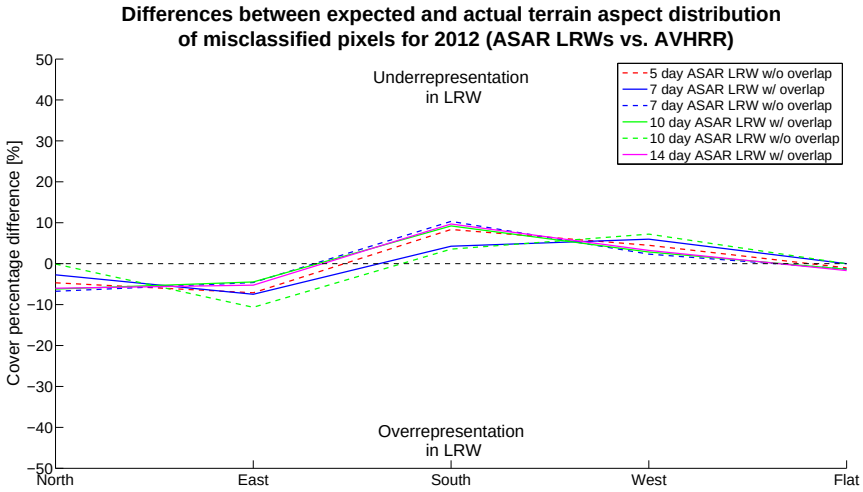

(a) ASAR LRW comparison against AVHRR

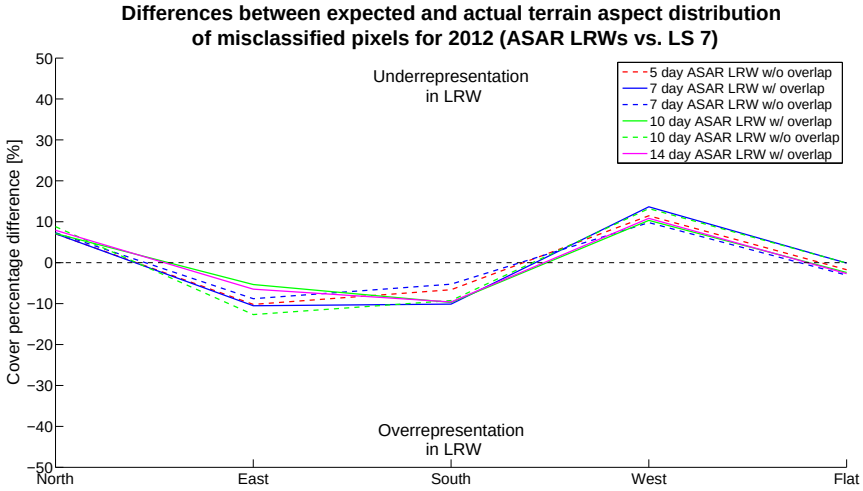

(b) ASAR LRW comparison against Landsat 7

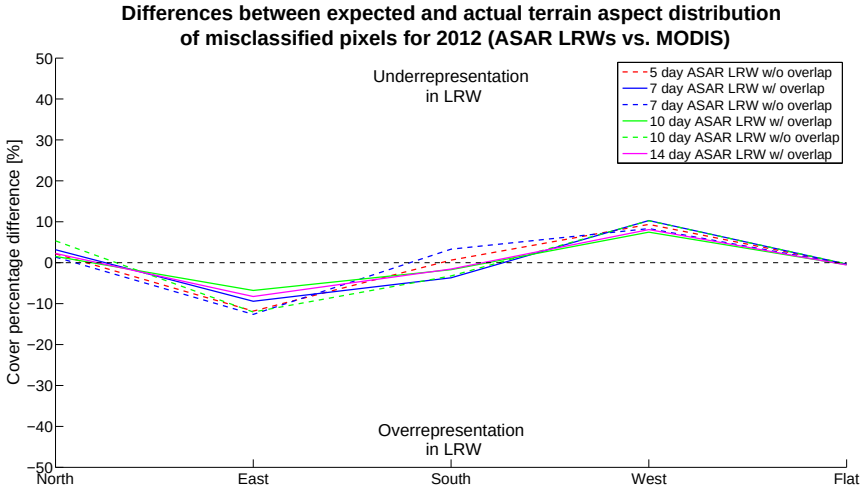

(c) ASAR LRW comparison against MODIS

Figure 5.5: ASAR LRW misclassification dependency on different terrain aspects

Underlying soil cover

The last external environmental factor assessed was the ground cover. Therefore, four classes were defined according to the scheme shown in table 3.8 on page 27: *Bedrock*, *detritus*, *glacier*, and *other*. As the class *other* consisted of a multitude of ground cover types, it was considered for the analysis.

The curve progression of the comparisons against all three optical snow cover products had a high similarity. There was a tendency towards an underrepresentation of bedrock as well as detritus covered ground within the misclassified pixels of the ASAR LRWs composites when compared to the reference products. With a cover percentage difference of 7%-11% (AVHRR) and 1%-8% (LS 7/MODIS), the difference for *bedrock* was slightly lower than for *detritus*, where the values reached approximately 10% for all three comparisons. Additionally, the range of cover percentage differences decreased as well. Regarding the ground cover class *glacier*, the cover percentage difference values decreased towards 2%-5%, independent of the chosen reference product.

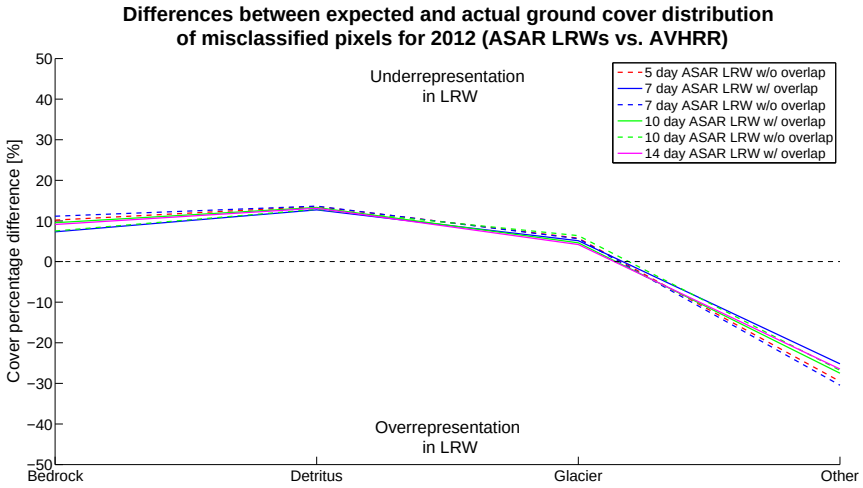

(a) ASAR LRW comparison against AVHRR

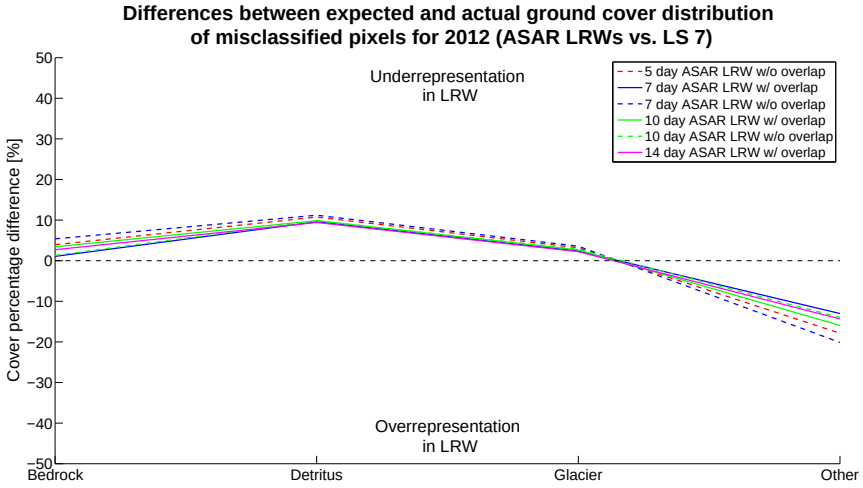

(b) ASAR LRW comparison against Landsat 7

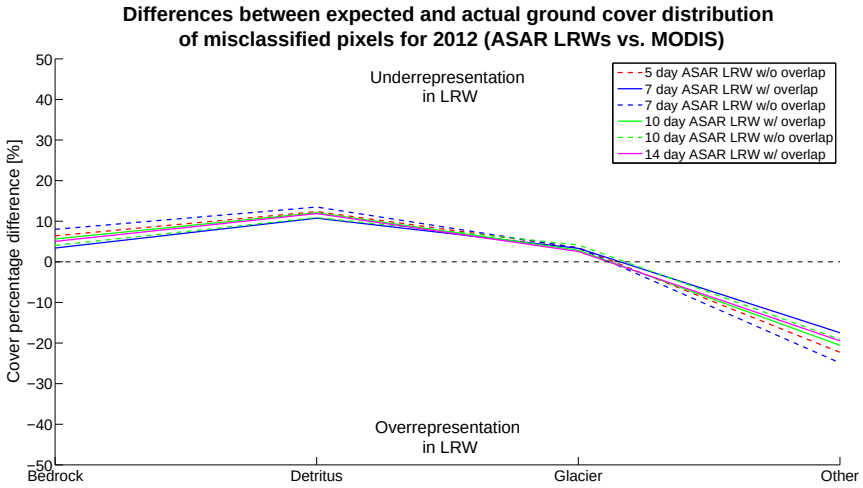

(c) ASAR LRW comparison against MODIS

Figure 5.6: ASAR LRW misclassification dependency on different soil cover types

5.2.2. RS-2 wet snow maps

In addition to the comparison between the optical snow cover products and the ASAR LRWs in section 5.2, the influence of environmental factors was investigated for the available RS-2 scenes as well. In difference to the comparison against ASAR scenes, scenes from both, 2010 (LRW composite with scenes from 2010-04-26 and 2010-04-27) and 2012 (single scene), were included into the comparison, as the RS-2 LRW from 2010-04-26/2010-04-27 had a very high areal overlap between ascending and descending scenes, with a temporal difference of only about twelve hours. As mentioned in section 5.1.2, only those pixels were flagged as *wet snow* where both polarizations (VV and VH) had *wet snow* as an output of the wet snow mapping algorithm.

Slope

When comparing the expected and actual distribution of terrain steepness (see equations 4.3 and 4.4), the curve progression was similar as for the ASAR case. Slopes between 0° and 10° were overrepresented in the RS-2 scenes/LRW composites as compared to the reference products. The cover percentage difference ranged from 15%-25% for the single scenes, for the two comparisons of the RS-2 LRW against the AVHRR and MODIS products, the values were at 10% (MODIS) and 37% (AVHRR). For slopes between 10° and 20°, the values for expected and actual slope distribution were relatively similar, resulting in cover percentage differences of in between -1.8% (overrepresentation in RS-2 scene) and +5% (underrepresentation in RS-2 scene) for both single scenes as well as LRW composites. Slopes between 20° and 40° were generally underrepresented within the RS-2 pixels classified as wet snow by the detection algorithm that were outside the optical product's snow extent. The cover percentage difference was highest for the comparison between the LRW composite and AVHRR with 14% and lowest for the LRW–MODIS comparison with about 2%. The cover percentage differences of single scene based comparisons were in between, with all values within a range of 5%. Slopes increasing towards 70° showed a decreasing underrepresentation of misclassified RS-2 pixels, whereas for slopes above 70° expected and actual steepness distribution were almost equal.
Generally, the variation of the comparisons based on LRW composites was higher than for comparisons based on single RS-2 scenes.

Terrain aspect

While the outcome regarding terrain steepness was similar between ASAR and RS-2, this was not true for the variable of terrain aspect. In contrast to the comparison shown in figure 5.5, misclassified pixels with a *northerly* terrain aspect were generally overrepresented by between 3% (comparison against LS 7 FSC) and 14% (AVHRR). The cover percentage difference regarding the RS-2 LRW composites were between -4% (vs. LS 7) and +2% (vs. MODIS). For *easterly* facing

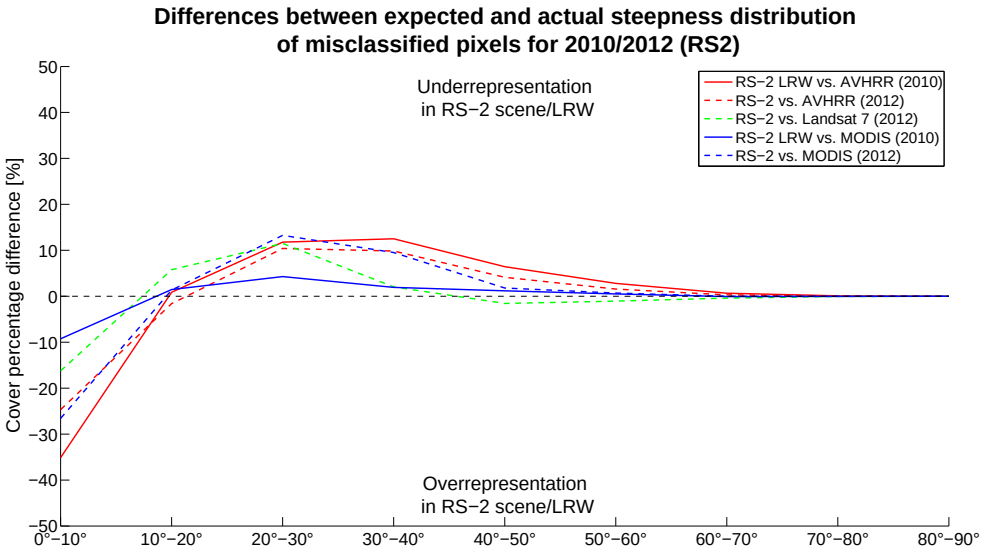

Figure 5.7: RS-2 misclassification dependency on different slopes

pixels, the misclassified pixels from the non-LRW comparisons against AVHRR and MODIS snow cover products had a trend towards an underrepresentation by up to 7%, whereas the LRW based comparisons as well as the comparison with LS 7 indicated an equal percentage of expected and actual distribution. For *southerly* exposures, the discrepancy between single scene and LRW based comparisons was accentuated with cover percentage differences of 14% and 17% for the single scene based comparisons against AVHRR and MODIS snow cover products, while the LRW based comparisons had cover percentage difference values of -1% and +3.5%. As for *easterly* facing pixels, the single scene-based comparison with the LS 7 FSC product seemed to agree more than with the LRW comparisons. The same situation could be seen for *westerly* exposed pixels, although with a trend towards an overrepresentation of this terrain aspect: both RS-2 LRW comparisons as well as the comparison with the LS 7 FSC product showed an overrepresentation by 2% to 4%, whereas the comparisons with MODIS and AVHRR had almost identical values with a 7% overrepresentation.

Underlying soil cover

Regarding the ground cover type, the curve progression showed a high degree of similarity to ASAR. Both, *bedrock* and *detritus* seemed to be underrepresented in the RS-2 scenes/LRWs, with the former's cover percentage differences ranging from 5% (RS-2 vs. LS 7) to 14% (RS-2 LRW vs. AVHRR), and the latter's from 11% (RS-2 vs. LS 7) to 26% (RS-2 LRW vs. AVHRR). Also pixels with the cover type *glacier* seem to be underrepresented within the totality of RS-2 wet snow pixels lying outside the snow cover extent of the optical reference products. For *glacier*, cover percentage difference values ranged from 2% (RS-2 vs. LS 7) to 12% (RS-2 LRW vs. AVHRR).

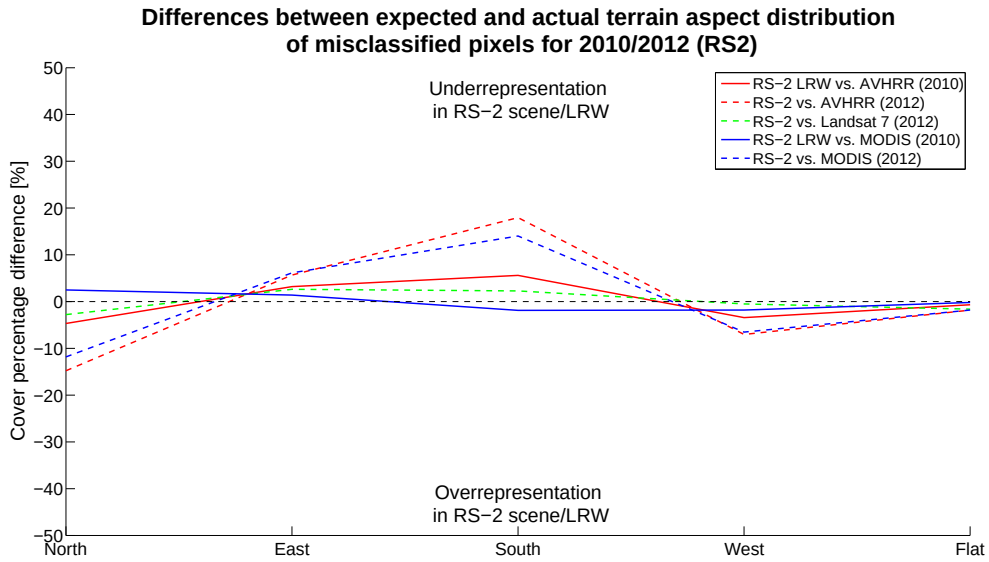

Figure 5.8: RS-2 misclassification dependency on different terrain aspects

5.3. Comparison of SAR wet snow mapping results against IMIS station data

In the following section, the results of the plausibility assessment using the SAR wet snow classification and the values derived from the IMIS stations are presented.

5.3.1. SAR wet snow mapping vs. snow height

Prior to the comparison of snow height derived from SNOWPACK, an accuracy assessment of the modeled values was carried out. Therefore, the snow height values measured directly by the IMIS stations were subtracted from the snow height values obtained from SLF's SNOWPACK model (see figure 5.10). The result based on 5 186 comparisons showed an average overestimation of the modeled snow height values by 8.38 cm, with a standard deviation of 10.39 cm. Based on these values, SNOWPACK snow heights <11 cm were assumed to be snow free, with the desirable side effect to also masking patchy snow covers of small depth.
As for the classification accuracy assessment of SAR wet snow mapping against optical products presented in section 5.1, only the user's wet snow classification accuracy could be calculated for the comparison against IMIS derived snow height information, as well as the producer's accuracy for snow free conditions according to SNOWPACK.

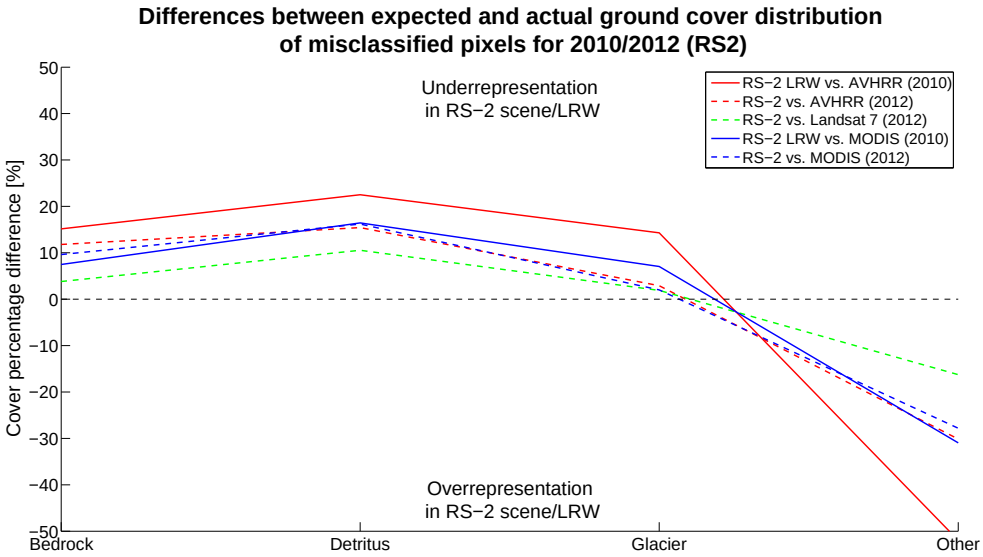

Figure 5.9: RS-2 misclassification dependency on different soil cover types

Envisat ASAR LRW

The user's and producer's accuracies for the individual combinations of LRW temporal tolerance and pixel area included around the IMIS stations are summarized in figure 5.11, the confusion matrices can be found in appendix C.1.

The user's accuracy for the different cases consistently reached values between 97% and 98%. The accuracy deteriorated with increasing temporal windows of the LRW composite, whereas increasing the number of included pixels to determine the snow's wetness state around the station improved the accuracy. Both findings agreed with the expectations: an increased temporal baseline of the LRW composites might have included multiple snow wetness states, thus influencing the classification. Increasing the number of pixels incorporated into the determination of the snow's state (*wet* or *dry*) might have canceled out errors due to noise in the backscattered signal, which would otherwise have caused misclassifications. However, the very high values for the user accuracies must be interpreted with care, since only about 4% of the situations had snow free conditions. The calculation of the producer's accuracy for *snow free* conditions according to the IMIS data is shown with the dashed lines in figure 5.11. The diagram shows again a trend towards a higher accuracy for bigger sized windows surrounding the station's position. The aforementioned tendency of smaller temporal baselines of the LRWs to higher accuracies cannot be seen anymore for the producer's accuracy.

RADARSAT-2

As a result of the small set of available wet snow classifications for RS-2 scenes, there were no situations where IMIS stations reported snow heights of less than 11 cm and could therefore

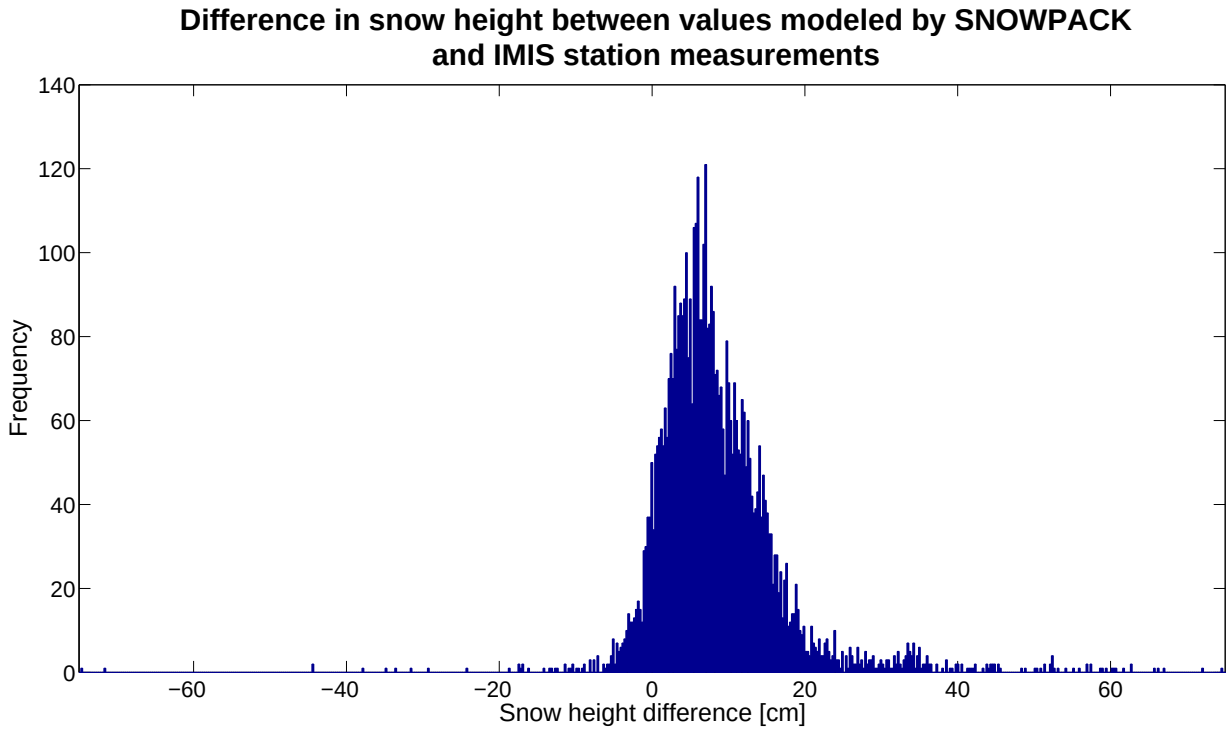

Figure 5.10: Histogram of snow height difference between modeled values from SNOWPACK and direct measurements at IMIS stations

be considered *snow free* (see tables C.5a to C.5d on page 115). Therefore, no conclusions could be drawn from the comparison of RS-2 scenes against SNOWPACK derived snow height information.

5.3.2. SAR wet snow mapping vs. IMIS LWC

As a second SNOWPACK derived parameter, LWC was compared against the SAR based wet snow classification. In order to be able to compare the binary wet snow classification, the LWC values were discretized into *wet* and *dry snow*. The limit was defined at the transition from the pendular (capillary forces dominate, water is kept between the grains) to the funicular regime (water will start to flow due to gravity), defined by Mitterer et al. (2013) as 3% LWC.
As the penetration depth L_p for C-band SAR is reduced quickly with LWCs above 0% (see section 2.3.2 on page 14), the presence of a layer with an LWC $\geq$3% was considered as sufficient for a classification of the snow pack as *wet* from the radar's perspective.

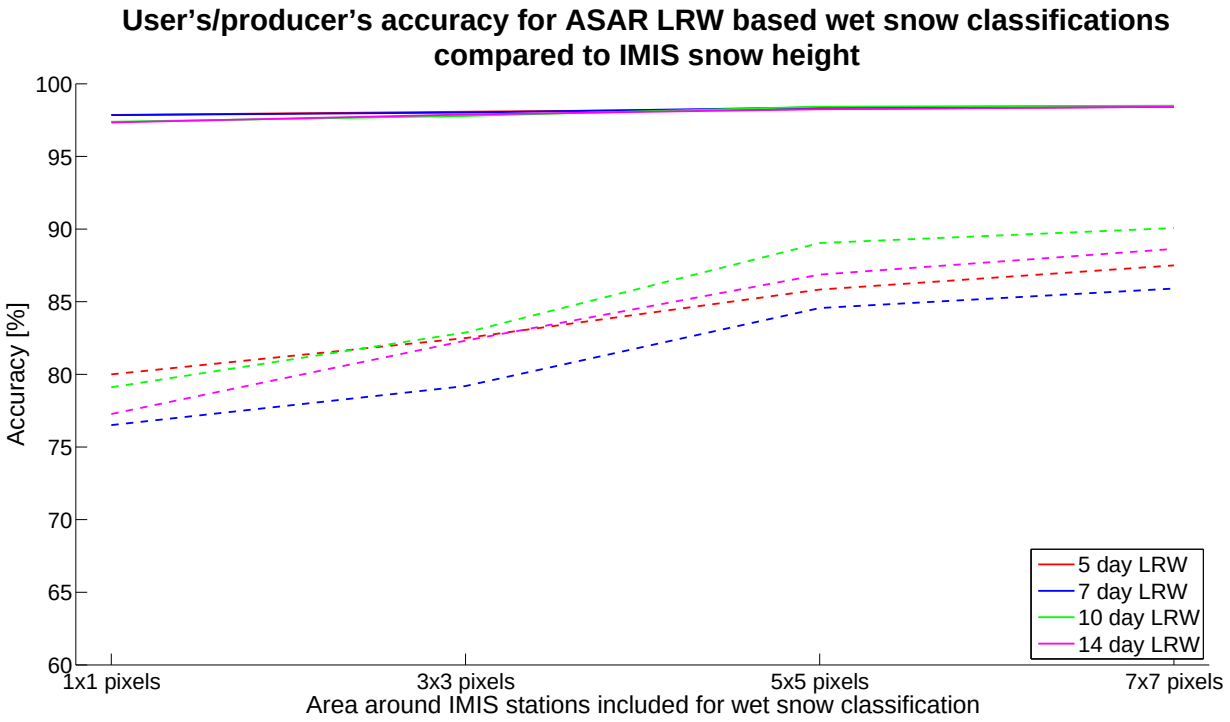

Figure 5.11: User's accuracy (solid lines) and producer's accuracy (dashed lines) for the comparison of ASAR LRWs with IMIS snow height information

Envisat ASAR LRW

As the parameter LWC allowed to differentiate between *wet* and *dry snow*, the overall accuracy could be calculated for every combination of LRW temporal tolerances and pixel windows surrounding the stations' coordinates.

In contrast to the user's accuracy for the comparison of the ASAR LRW based wet snow classification, the LRW composites with the smallest temporal baseline did not score the highest overall accuracies, it was rather the inverse of the results of the comparison against IMIS derived snow heights. Regarding the number of included pixels around the station coordinates, the results were as expected, with bigger areas reaching higher accuracies as compared to smaller areas. The overall accuracy values ranged from 70% (5 day LRW with a 1×1 pixel area) to a maximum of 76% for the 14 day LRW with 7×7 pixels included around the stations. The accuracy range over all pixel areas was higher for LRWs with a small temporal tolerance, even though the percentage differences never exceeded 3.5% for a LRW composite. The individual confusion matrices can be found in tables C.6a to C.9d on pages 116–119.

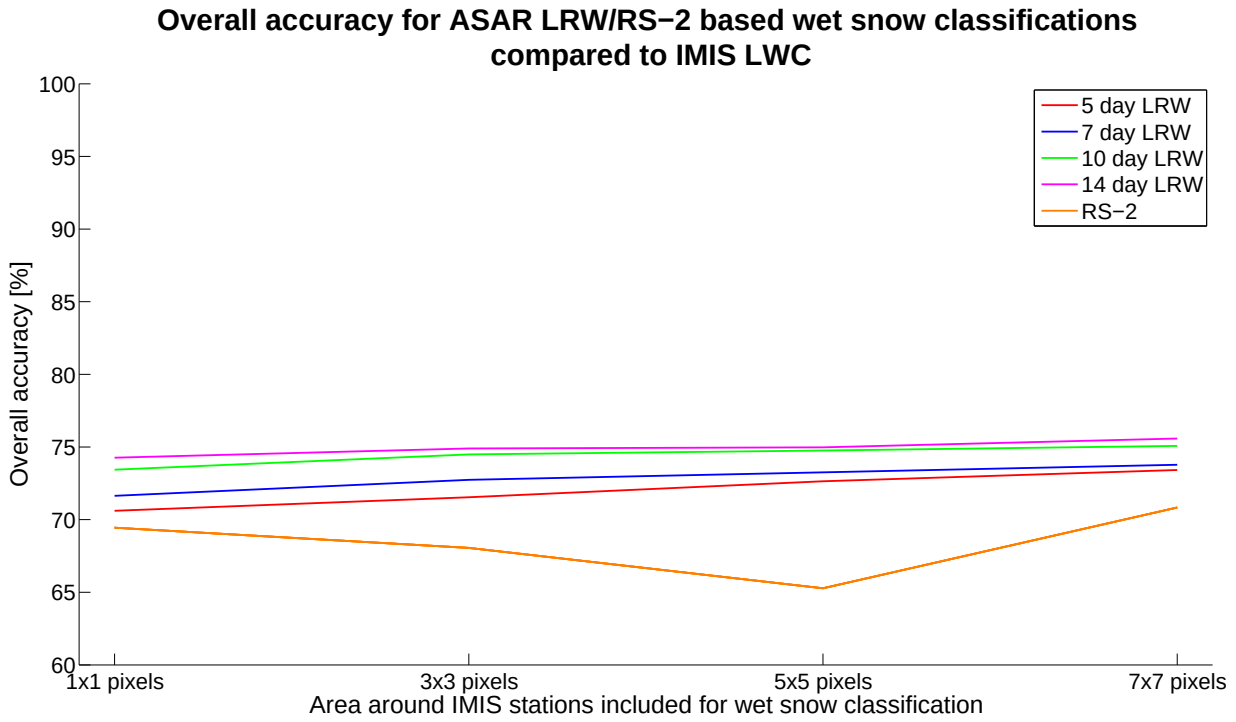

Figure 5.12: Overall accuracy for the comparison of ASAR LRWs with IMIS LWC values

RADARSAT-2

The overall accuracy for the comparison between SNOWPACK derived LWC values and wet snow classification for RS-2 was lower compared to the overall accuracies of ASAR LRW (see figure 5.12 and tables C.10a to C.10d). For the 1×1 pixel case the overall accuracy was at 69% and thus within 1% to 4% of the values reached by the different ASAR LRWs. Unlike the accuracies for ASAR LRW, the accuracy values deteriorated for the 3×3 (68%) and 5×5 (65%) pixel case, before increasing again for the 7×7 pixel case (71%).
Although the line progression was unexpected, the bad performance might have been caused by the small number of possible comparisons (n=72). A change of the overall accuracy by 5% could be induced by only four misclassified pixels/stations. Therefore, these values have to be interpreted with care.

5.4. Assessment of the influence of liquid water on SAR backscatter

This section describes the results of the analysis made regarding the influence of liquid water within the snow pack on the backscattered radar signal. Therefore, the LWC values modeled

by SLF's SNOWPACK at the location of the 38 selected IMIS stations were converted to LWV values according to formula 4.6 on page 40. A statistical analysis of regarding the correlation between radar backscatter and LWV was carried out by means of a correlation analysis and a regression analysis. The analysis was executed for different depths of wet snow layers at 10 cm intervals up to a depth of 90 cm as well as for the total LWV of the snow pack.

5.4.1. Influence of LWV on ASAR LRW composites

As mentioned in section 4.4.3, the three variables LWV, LRW temporal window, and the integration area for the backscattered signal were varied, resulting in a total of 160 different combinations with between 3 300 and 10 300 observations for 191 dates between 2007 and 2012. Since a presentation of all the results was not feasible and the results were highly consistent, only a representative selection is described in the following. The plots not shown in this section can be found in appendix D.

The correlation was overall weakest for the 5 day LRW case (see figure 5.13) with higher coefficients for bigger areas. A trend towards a higher coefficient could be detected with increasing integration depths of the LWV, although the values did not differ greatly. The lowest/highest correlation for the 1×1 pixel case were -0.37/-0.42, whereas they reached -0.42/-0.47 for the 7×7 pixel case. The values indicated a moderately negative correlation for all LWV depths, which was highly significant. Regarding the R^2 values for the 5 day ASAR LRW case, the same pattern could be seen with the lowest values for the 1×1 pixel area and the highest values for 7×7 pixels. While the values were again lowest for the LWV integrated over the whole depth as well as for small integration depths, the value culminated for an integration depth of 70 cm, although the differences were again of small magnitude. The extremes were reached with 14% for 1×1 pixels and the total LWV, and 22% for 7×7 pixels and 70 cm integration depth. These results were highly significant as well.

For the 14 day ASAR LRWs, the results were very similar, even though with slightly improved correlation coefficients as well as R^2 values (see 5.14). Regarding the former, the values ranged between -0.43 and -0.48 for the 1×1 pixel case and -0.47 and -0.53 for an averaging area of 7×7 pixels. The R^2 values ranged in between 18% and 23% for the smallest, and 22% and 28% for the largest averaging area around the stations. Again, all these values were highly statistically significant with $p<0.001$ and indicated a moderate correlation between LWV and the measured backscattered signal.

The described two cases mark the upper and lower limits for both Spearman's correlation coefficient as well as the R^2 values, with the 7 and 10 day LRW composites lying in between. As mentioned, the values show a statistically significant but moderate correlation between the

two variables, although the R² value indicates that a precise prediction of LWV based on SAR backscatter will generally not be possible.

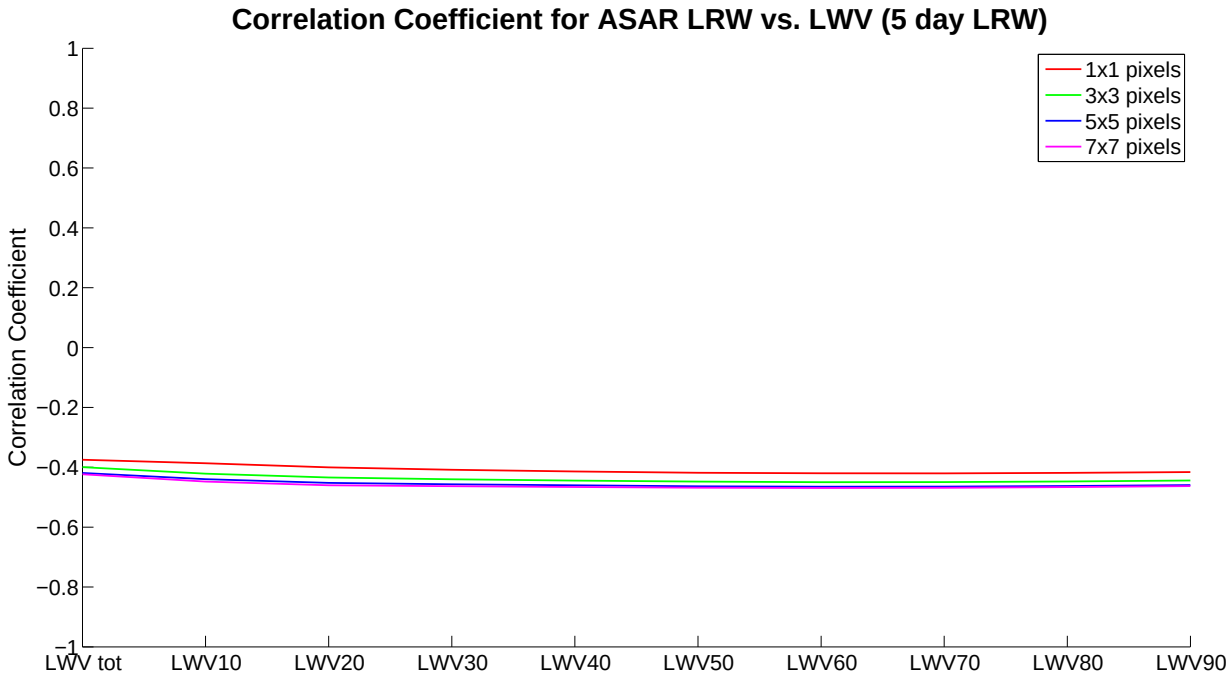

(a) Spearman's Rho

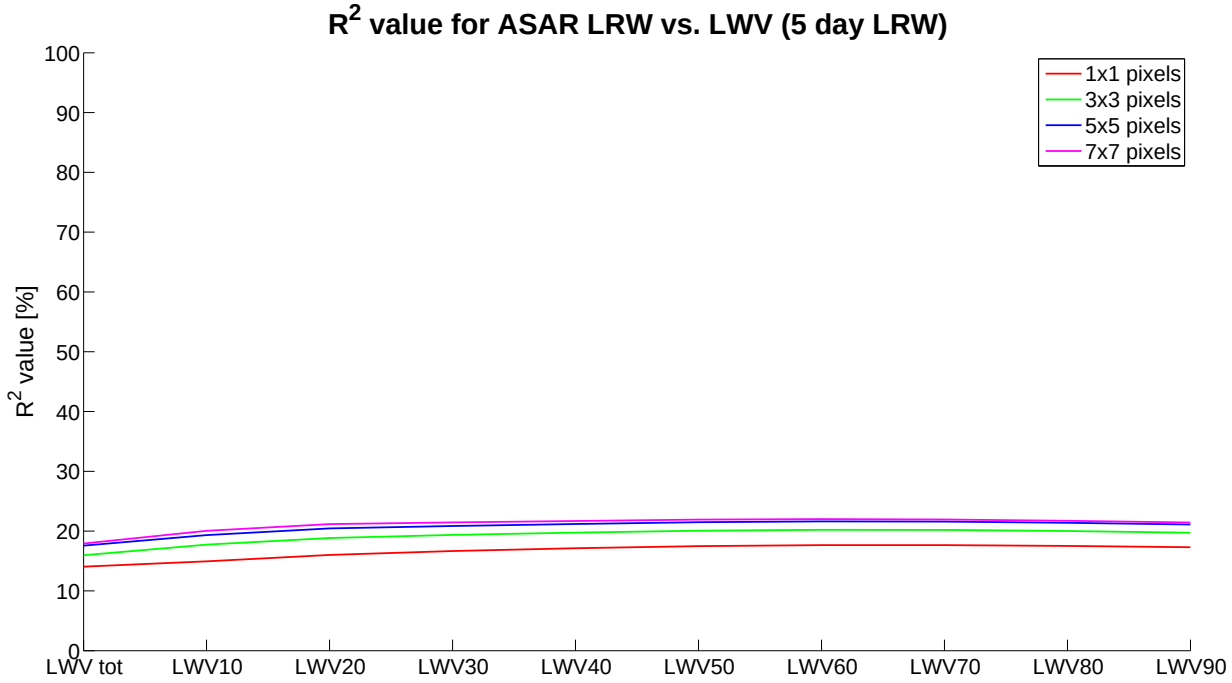

(b) R²

Figure 5.13: Correlation coefficient and R² for 5 day ASAR LRW

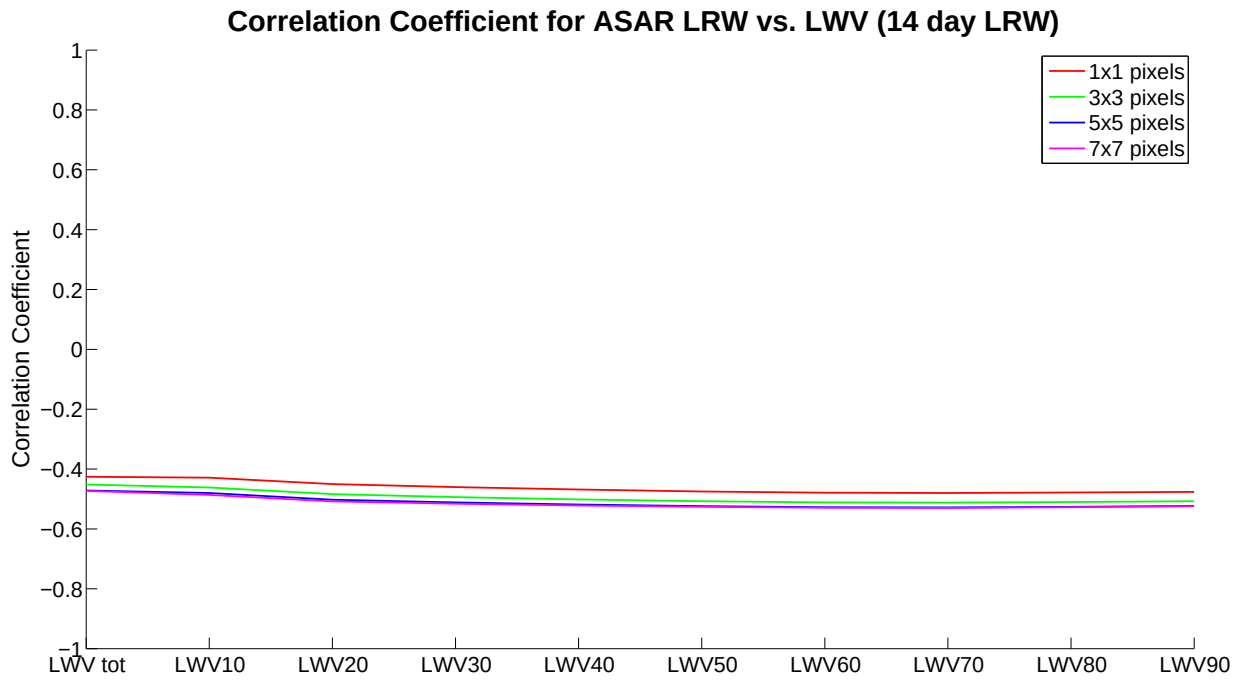

(a) Spearman's Rho

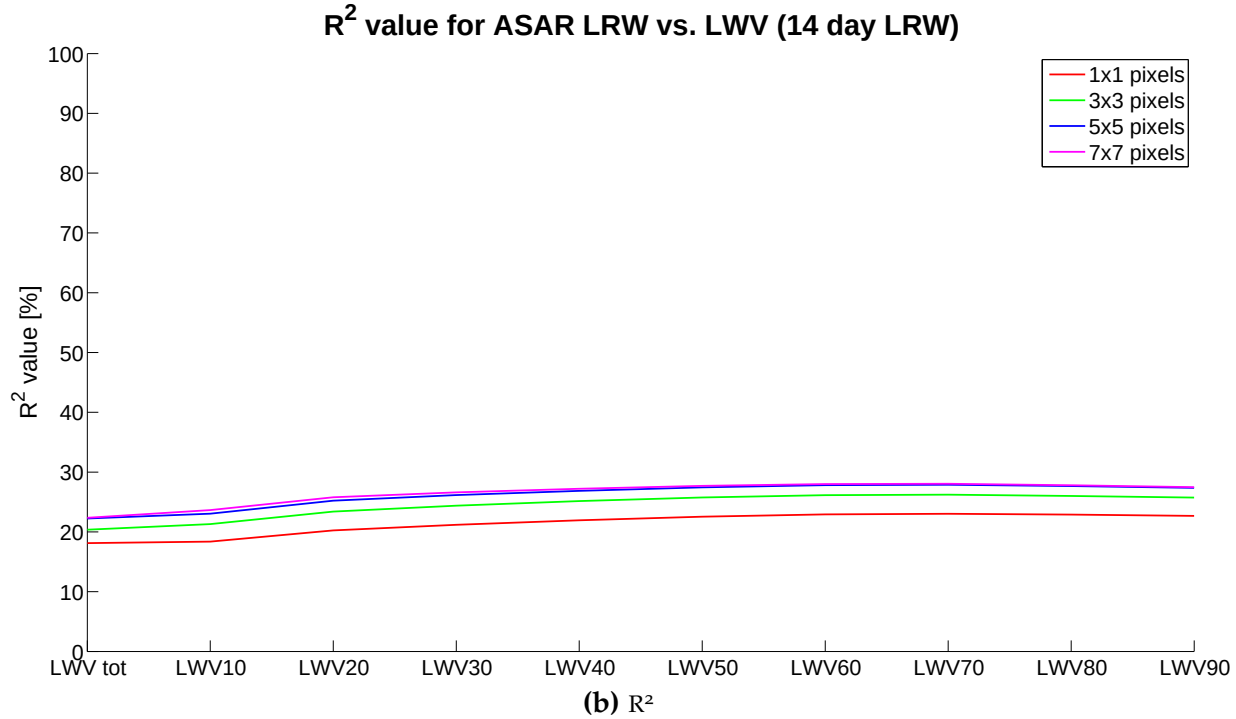

(b) R^2

Figure 5.14: Correlation coefficient and R^2 for 14 day ASAR LRW

5.4.2. Influence of LWV on RS-2 scenes

For the RS-2 scenes, the two polarizations (VV and VH) were analyzed statistically for relationships with LWV values, additionally the possibility of combining the two polarizations was looked into as well. As for the assessment of the ASAR scenes, the LWV values were calculated for depths between 10 cm and 90 cm at 10 cm intervals as well as the total LWV of the snow pack. Also the circumjacent number of pixels was kept as for the ASAR case. The plots not shown in this section can be found in appendix D.

As expected, the correlation for the VV polarization got stronger the more pixels were used for the determination of the backscatter, probably due to a smoothing effect of extreme values (see figure 5.15a). For the 1×1 pixel case the correlation coefficient was -0.18 for the total LWV of the snow pack and between -0.3 (LWV_{90}) and -0.35 (LWV_{20}) for different depths, showing a largely stable behavior over all depths up to 90 cm. Except for the 1×1 and 3×3 pixels cases with LWV_{tot}, all correlations were statistically significant (p-values <0.02).

A similar outcome can be seen for R_2 (see figure 5.15b): higher numbers of included pixels increased the R_2 value, although the curve progression differed between the cases. For the 1×1 pixel case, the value was lowest for the insignificant LWV_{tot} case (3%) and reached its maximum for LWV_{20} with 11%, before decreasing slightly with increasing LWV integration depths. For the 3×3, 5×5, and 7×7 pixel case, the curve progression was alike, with the lowest R_2 values for LWV_{tot} before exhibiting a maximum value for the LWV_{50} or LWV_{60} case. For greater LWV depths, the values remained within 0.5% of the maximum value. Except for the already mentioned LWV_{tot} case for 1×1 pixels, only the LWV_{tot}/3×3 pixel case was statistically insignificant.

Regarding the VH polarization, the findings were similar to the VV case, although the values for both, the correlation coefficient as well as R^2 deteriorated slightly. For the VH polarized RS-2 backscatter, the results were only significant for all integration areas at depths <20 cm, with the correlation coefficient and the R^2 value for LWV_{tot} being insignificant for all integration areas except 7×7 pixels.

As for the ASAR LRW composites, the general correlation between the RS-2 backscatter of either polarization and the amount of liquid water within the snow pack was moderately negative, with the R^2 values indicating that an accurate prediction of LWV based on the backscattered signal is generally not possible, even though high values in LWV will produce low backscatter and vice versa.

As a last analysis, the relationship between LWV and a combination of the two available polarizations RS-2 was investigated. Therefore, the backscatter of the two polarizations were either subtracted (VH-VV) or divided (VH/VV) by each other. Unfortunately, as a result of the high variance of the backscatter for given LWVs and almost parallel slopes of the regression lines for VH and VV, the results for both operations were either insignificant or exhibited lower R^2 values

than for the single polarization case, while lacking an improvement in correlation strength (see figures D.7 and D.8).

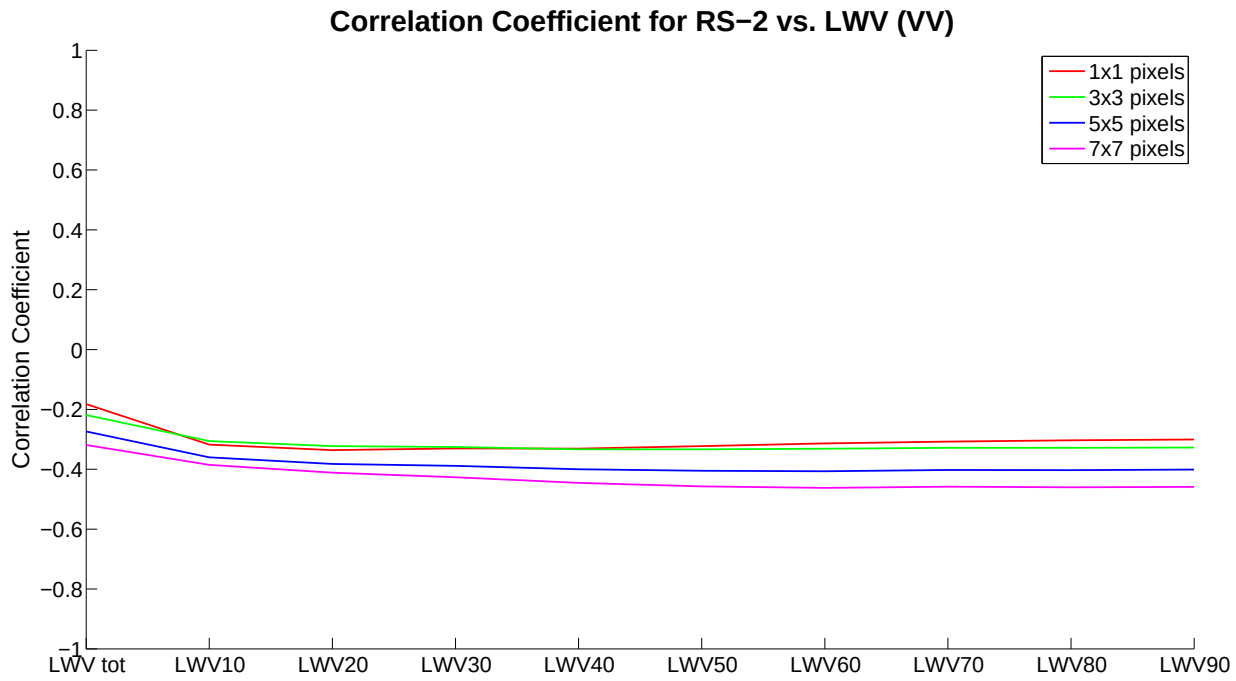

(a) Spearman's Rho

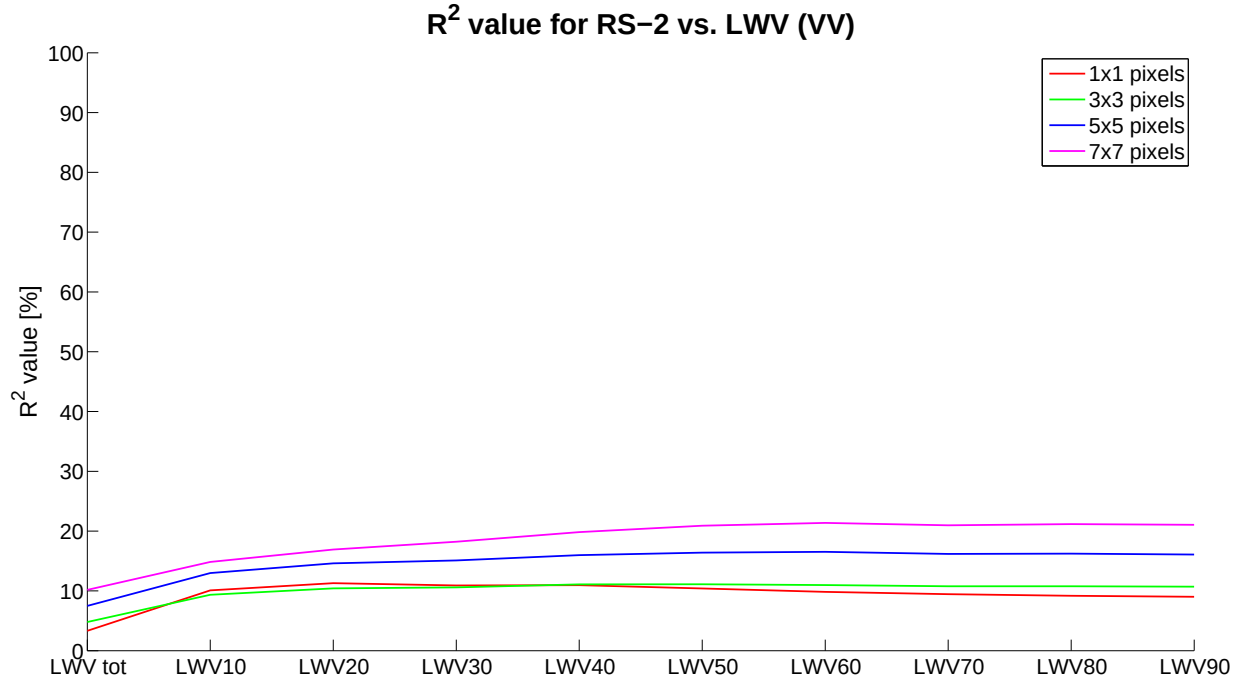

(b) R^2

Figure 5.15: Correlation coefficient and R^2 for RS-2 (VV)

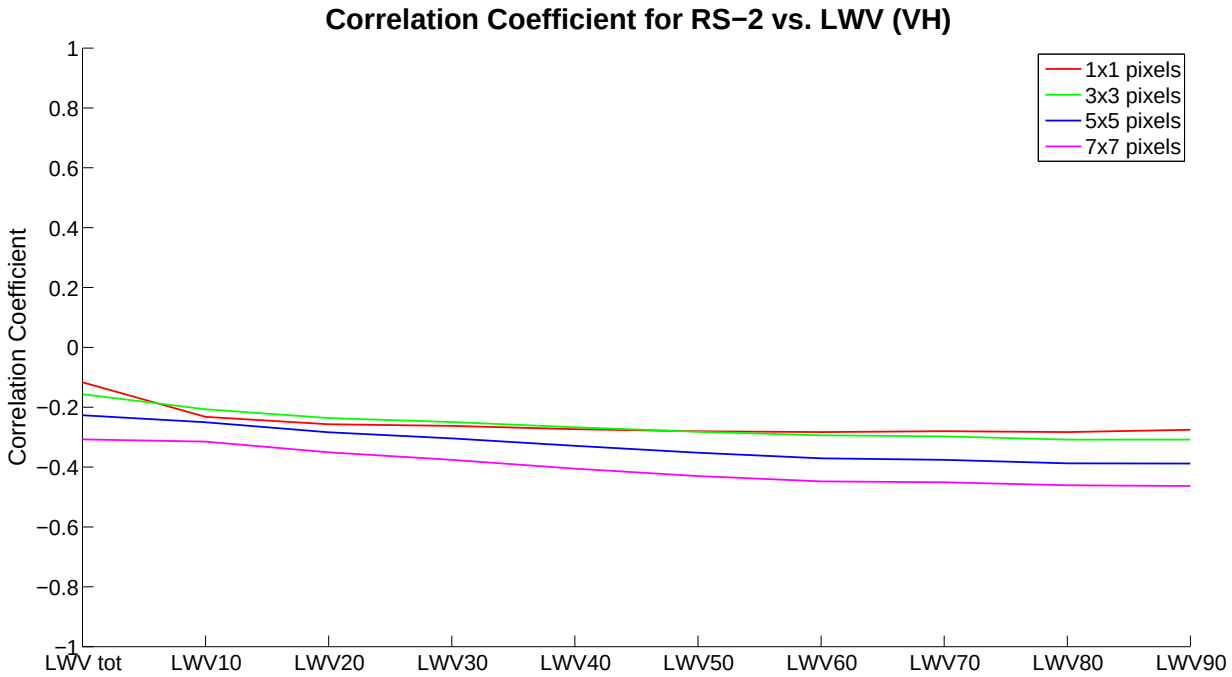

(a) Spearman's Rho

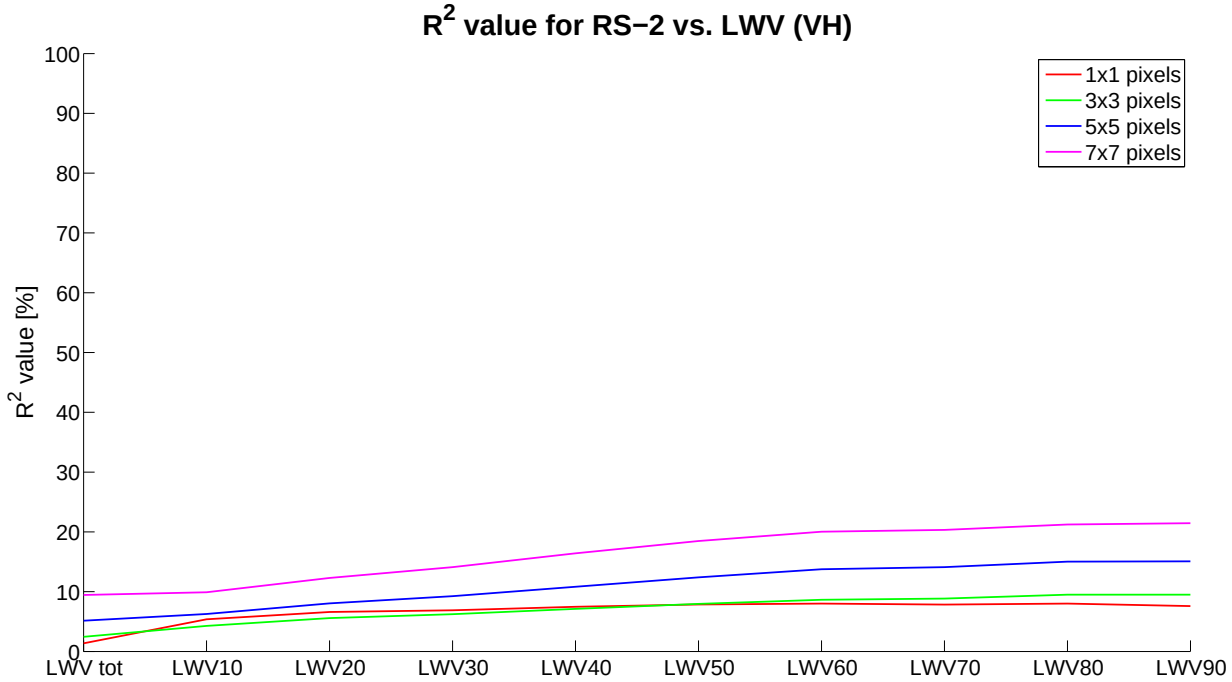

(b) R^2

Figure 5.16: Correlation coefficient and R^2 for RS-2 (VH)

6. Discussion

This section consists of a discussion of the LRW and snow detection algorithms used as well as the results presented in the previous section, following the structure from section 5. The results are discussed regarding their plausibility by comparing them to the available scientific literature. The limitations in terms of data quality and availability are shown. The section ends with suggestions for improvement.

6.1. Discussion of results

6.1.1. Analysis of LRW calculation

Due to Switzerland's mountainous terrain causing geometrical distortions and shadowing, the usability of RTC scenes for the derivation of physical parameters is diminished. To overcome these limitations, as well as to improve the spatial resolution of the SAR scene, LRW composites can be calculated, using multiple scenes with differing orbits. Although LRWs represent a useful extension of the GTC and RTC products, the approach has some limitations, especially for short-lived processes such as snow melt. As investigated by Caves et al. (1999), "the usefulness of this [LRW] approach is limited by the temporal lag between the ascending and descending passes which is latitude dependent". Regarding the snow melt case for Switzerland, this temporal lag should not exceed seven to ten days in order to minimize mixture of wet and dry/no snow signals in the combined image. Even though this requirement could be fulfilled for most of the year 2012 where a dense time-series was available, this was not the case for most of the years 2007–2011 (see figures B.1a to B.1d on pages 103–106), inducing an uncertainty in the wet snow classification of more than 5% for the Swiss Alps region compared to a classification using single SAR scenes (Schaub, 2011). These uncertainties could be found as well in this study (see sections 5.1/6.1.3).
Although the temporal constraints limit the use of LRWs to dense time-series or slow-processes, for which a temporal lag does not constitute a problem, the approach can also be used for the generation of reference scenes needed for wet snow detection approach from Nagler & Rott (2000) in order to overcome the absence of longer dry and cold periods (Schaub, 2011). Therefore, single dry scenes from multiple years can be merged using the LRW approach. It was used for this study to calculate yearly reference LRWs, using scenes from dry and cold periods between mid December and mid February.
Furthermore, given a dense time-series of overlapping, RTC SAR scenes, the LRW approach provides a solid basis for wet snow mapping even in mountainous terrain.

6.1.2. Analysis of the wet snow detection algorithm

Like the LRW calculation, the wet snow detection algorithm from Nagler & Rott (2000) showed its strengths and weaknesses, previously presented by Caves et al. (1999), during the course of this thesis. The algorithm implementation was fairly easy and, as a result of the fixed threshold of -3 dB, usable in a wide range of terrains, given RTC images. As mentioned above, the constraints regarding the missing coverage and geometric distortions induced by the terrain could be addressed using LRW composites. Other influences were of physical nature and are thus harder to handle. First of all, since the radar cannot detect both *wet* and *dry snow*, it was not possible to draw conclusions regarding the melting process' depth within the snow pack. This was because snow melting processes occurring on the surface had the same signature as a layer of wet snow within the snow pack, given the same LWC of the layer. This presented a big drawback, as the snow melting process was influenced by the terrain's aspect: satellite passes that take place in the morning were more likely to detect surface melting processes on easterly facing slopes (and evening passes on westerly facing slopes), due to thawing caused by the morning/evening sun. Additionally, since the area of dry snow could not be detected directly using SAR, but only either inferred using wet snow maps from previous years (Nagler et al., 1998) or by assuming that areas above the wet snow line were covered by dry snow, and therefore adding uncertainties (Storvold & Malnes, 2004; Storvold et al., 2006), the statistical comparison to optical products could only yield the user's accuracy for the wet snow classification, not the overall accuracy (see section 4.4).

6.1.3. Classification accuracy of SAR wet snow mapping against optical products

The results of the comparison of snow cover data derived from optical remote sensing and wet snow cover maps created from SAR LRW composites underlined the advantage of LRWs created from scenes with differing orbit configurations in terms of classification accuracy as well as consistency of the outcomes. This was not only true when averaging all results, but also for the individual comparisons between SAR derived wet snow maps and optical snow cover products. When looking at the two cases individually (with and without overlap between scenes from different orbit configurations), the results were as expected: for the overlapping LRWs, there was a general trend towards higher user's accuracies for composites with a shorter temporal integration time (five or seven days), whereas the classification accuracy deteriorated with longer temporal baselines. This fact can be explained by the mixture of different snow wetness states within a single LRW, caused by bigger temporal differences (Schaub, 2011; Piesbergen et al., 1995).

While the trend towards better classification accuracy for shorter temporal tolerances was relatively distinct for the LRWs with overlaps between the different orbit configurations, it was not as clear for the non-overlapping case. As seen in section 5.1.1 the highest accuracy was reached for 7 day LRWs (LS 7/MODIS) and 5 day LRWs (AVHRR) respectively. The fact that these LRWs were created from images of the same orbit configuration allows to conclude that for these cases and with the given temporal density of the time series, a time window of seven days was necessary in order to integrate enough scenes for the LRW approach to work, thus minimizing the topographic effects. As mentioned earlier, a two week time span seemed to increase the noise from multiple snow wetness states, thus deteriorating the classification accuracy.

As a result of the few comparisons possible for the RS-2 case and the big variation between the different cases, the ASAR findings could neither be accepted nor refused. While all RS-2 scenes seemed to perform well against the AVHRR product, this was not true for the MODIS case, with a high accuracy for the single scene based comparison and only moderate results for the two based on the RS-2 LRW.

A comparison of the accuracies reached in this study and the ones found in the scientific literature was difficult, as the latter only reports overall accuracies, thus including the statistically derived dry snow cover (see section 6.1.2), reportedly overestimating the snow covered area for areas above 1 500 m altitude (Caves et al., 1999). However, when comparing the results of this thesis with the findings from Hindberg et al. (2014), the outcomes seem to match well. Hindberg et al. (2014) presented three user's accuracies for wet snow detection in Lofoten (Norway) and compared RS-2 with Landsat 8. All three snow detection methods were based on a -3 dB thresholding. For the first case, the co-polarized channel, for the second case, both the co- and cross-polarized channel and for the third case, either the co- or cross-polarized channel had to be lower than the -3 dB limit to classify a pixel as wet snow. While the first case was relevant for the single-pol ASAR LRW composites, the second approach was applied to dual-pol RS-2 scenes. The user's accuracies reported for the Lofoten area were 82.26% for the first and 76.26% for the second requirement. The corresponding accuracies from this thesis were between 76% and 90% for the ASAR LRW–LS 7 FSC comparison (depending on the temporal window) and 89% for the RS-2–LS 7 case. Even though the other optical products exhibited large differences in terms of spatial resolution, the agreement of the comparisons regarding the user's accuracy were quite good, thus showing the potential of wet snow detection using SAR LRW composites even in rugged, mountainous terrain.

6.1.4. Analysis of external influencing factors on wet snow classification accuracy

This section follows the structure of sections 5.2.1 and 5.2.2. Given the similarity of the results between ASAR and RS-2, the analysis was combined for both data sources.

Slope

As shown in sections 5.2.1 on page 51 and 5.2.2 on page 58, areas with no or small gradients up to 10° were generally overrepresented in the totality of misclassified pixels when compared to the expected distribution of these slopes, independent of the SAR data source or the optical reference product. When looking at both, flat (see figure 6.2) and mountainous regions of Switzerland (as in figure 6.1), the reasons for these misclassifications became clearer. Firstly, the topography of the Swiss Plateau, accounting for more than 30% of Switzerland's total surface area (Carol & Senn, 1950), is predominantly flat at an altitude of around 400-600 m and therefore seldom covered by snow. As visible in figure 6.2, a lot of isolated pixels were classified as wet in the flat areas. Some reasons for these misclassifications were listed by Caves et al. (1999), such as agricultural activity, flooding/precipitation or wind roughing of open water. Although the first issue should generally be solved using a mask for the agricultural areas, the second one might have constituted a problem that would explain part of the misclassifications. The third issue can be seen multiple times in figure 6.2, with the most prominent occurrence in the Lake Überlingen. Although a lake mask for water bodies with a surface of more than 0.4 km² was applied during the wet snow classification, this part of Lake Constance was not part of the data set, as it lies outside of Switzerland's borders. But not only the Lake Überlingen constituted a source of misclassifications, but also the many small lakes as well as rivers and bogs. Examples could be seen in the Saas and Matter Valley, where the misclassified pixels followed the course of the rivers, as well as east of Brig, where misclassifications occurred close to an within lakes. It seems reasonable to assume that the changes in surface roughness of lakes and rivers at least partly explain the overrepresentation of flat and nearly-flat surfaces, especially if these were located in the Swiss Plateau, since these areas usually do not lie within the snow cover extents from the optical products.

The underrepresentation of gradients between 10° and 30° and partly 30°-40° in the totality of misclassified pixels was more difficult to explain. One reason might be due to the location of these gradients, as they mostly occur in the alpine and pre-alpine parts of Switzerland and were therefore more likely to be within the snow cover extent of the optical reference products, resulting in fewer misclassified pixels. The accurate representation of slopes above 40° when compared to the expected distribution was most probably due to the overall small cover percentage of those slopes: 40°-50° slopes only account for roughly 6% of Switzerland's total

area, slopes above 50° only about 2.5%. In combination with the high probability of snow cover during winter and spring due to their location in the pre-alpine and alpine regions, an under- or overrepresentation of these slopes was unlikely.
Even though systematic under- and overrepresentations were detected for all of the comparisons (for both, RS-2 and ASAR), no evidence could be found in the scientific literature of terrain slope influencing the classification accuracy – except for its influence on geometric distortions within the scenes, which were minimized using the LRW approach. Additionally, since the curve progression of under- and overrepresentation can be explained logically, the effect of slope seems not to be of significance.

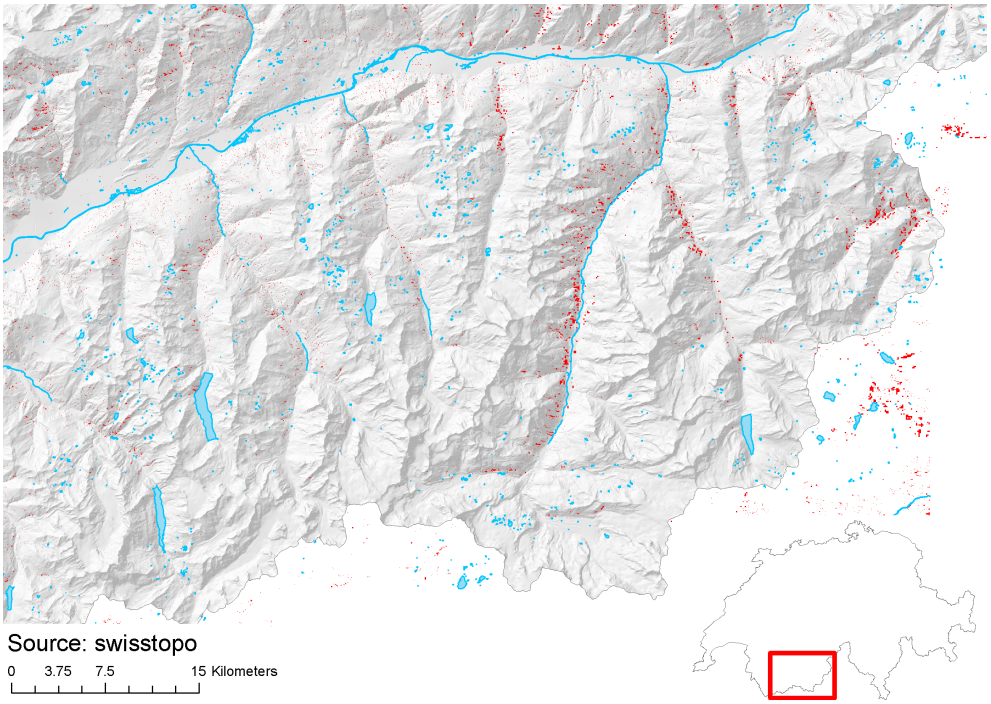

Figure 6.1: Distribution of misclassified pixels (red) in the Valais region (Envisat ASAR LRW–LS 7, 2011-03-23)

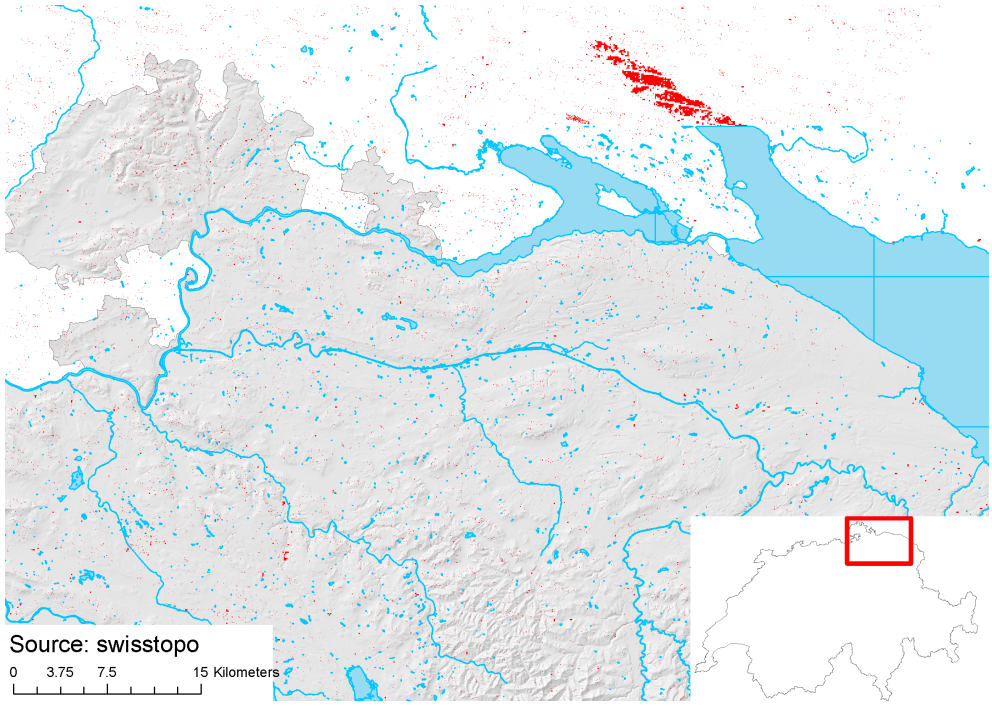

Figure 6.2: Distribution of misclassified pixels (red) in Eastern Switzerland (Envisat ASAR LRW–LS 7, 2011-03-23)

Terrain aspect

Regarding the terrain aspect, the agreement from the comparisons with different optical snow extent sources was not as concordant as for the terrain's slope. While the easterly facing slopes were overrepresented and westerly exposures underrepresented in all comparisons, it is also visible that the differences between expected and actual distribution was significantly stronger for the LRW composites without areal overlaps. When looking at figure 6.3, created from two LRW composites integrating either only ascending (green pixels) or only descending pixels (red pixels) with MODIS, the green pixels are located predominantly on the easterly facing slopes, whereas the red pixels are in majority located on the westerly exposed areas. Thus, for both cases, the misclassifications can be found predominantly on the side facing away from the sensor. This has two potential implications: first of all, the local resolution was worse for these pixels, and secondly, the high incidence angle caused part of the radar waves to be reflected away from the sensor, thus lowering the radar backscatter from these areas. A lower radar backscatter directly influenced the outcome of the wet snow classification approach by increasing the gap in backscatter between dry reference and the wet snow scene.

Even though the snow cover reference products generally showed the usual snow cover distribution with less snow in westerly and south-westerly exposed slopes due to solar irradiation and prevailing winds (Ehrler et al., 1997) and would thus cause an overrepresentation of misclassified

pixels on these slopes, the proportion of scenes from ascending and descending orbits seems to influence the statistics more.
Since LRWs with an areal overlap between scenes with differing orbit configurations do not only improve the local resolution but also deliver more accurate backscatter values for areas facing away from the sensor, the differences between expected and actual distribution of misclassified should result in a more accurate classification of the wet snow distribution. Even though this can be seen in figures 5.5 and 5.8 to a certain extent, the differences were still relatively large. This could partly be explained with the definition of "LRWs with overlap", since already a single pixel with coverage from both, an ascending and a descending scene, was sufficient for the LRW to be classified as "overlapping". When looking at examples with an areal overlap of almost 100% (e.g. the RS-2 LRW composite from 2010-04-26/2010-04-27), the differences between expected and actual distribution of misclassified pixels were further diminished, in the RS-2 example to about 3% for the easterly and westerly exposed slopes (see figure 5.8).
Given the above results, an influence of the aspect on the classification accuracy of wet snow could not be ruled out, even though different aspects caused misclassifications mainly due to their influence on the imaging geometry. This effect can be minimized effectively by using LRW composites with different viewing directions and a temporal baseline that is as small as possible.

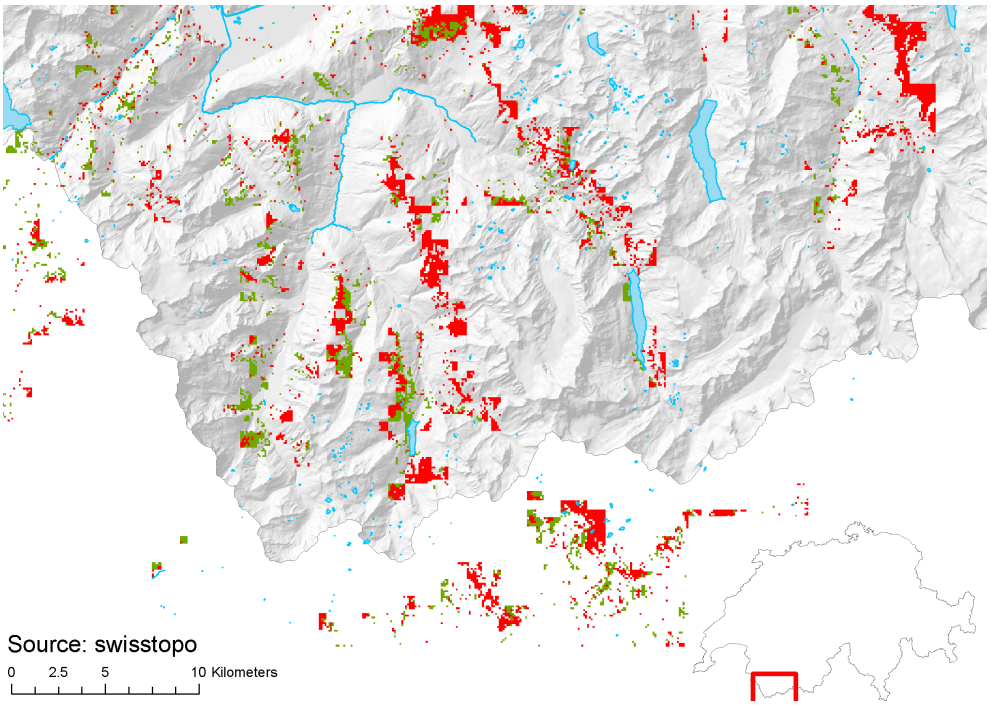

Figure 6.3: Distribution of misclassified pixels in the Valais region for the comparison between Envisat ASAR LRWs and MODIS. Green: ASAR LRW from 2010-04-12 (composite of ascending scenes), red: ASAR LRW from 2010-04-26 (composite of descending scenes)

Underlying soil cover

For the last of the assessed external factors, underlying soil cover, the agreement between the comparisons with different optical references was again very high. For all three different soil cover types (*bedrock*, *detritus*, and *glacier*), fewer pixels were misclassified than would be expected from the distribution of the respective soil covers (see figures 5.6 on page 57 and 5.9 on page 61), although for *bedrock* and *glacier* the deviations were only relatively small.
For the explanation of the differences between the expected and actual distribution of misclassified pixels three causes are thinkable:

1. The underlying soil directly influences the (backscatter) properties of the snow cover,
2. the spatial distribution of soil cover types influences snow cover,
3. the misclassifications are not caused by soil itself, but soil cover distribution is dependent on other factors (spurious correlation).

Regarding the first case, the underrepresentation could be caused by the influence of the ground cover type on the drainage properties. Given a good drainage of the soil (as with e.g. detritus, Hiller et al., 2005), not only the drainage of the soil itself, but also the snow's drainage is improved, which can decrease the LWC in the lower parts of the snow pack. A decrease in LWC will increase the radar backscatter (given the snow in the upper part of the snow pack is dry or almost dry and can thus be penetrated), reducing the chance of a pixel being classified as *wet* and therefore shifting the cover percentage difference towards an underrepresentation compared to the expected misclassification distribution.
While the first explanation looks at the influence the soil cover has on the snow pack, the second one concentrates on the possibility that the spatial distribution of a soil cover influences the statistics. When looking at the altitudinal distribution of all three soil cover types, *glaciers* have a lower limit of about 2 000 m with the majority of the glaciated areas ranging from 2 500 m and 3 500 m (see figure 6.6a on page 80). Since snow cover is highly likely even in the spring season for this altitude, thus covering almost the whole extent of *glaciers*, only single pixels at the *glacier's* edge might be classified wrongly, therefore inducing an underrepresentation. The same is true for the soil cover type *detritus*, with areas predominantly located between 2 000 m and 3 000 m of altitude (see figure 6.5a). In difference to *glaciers*, *detritus* covered ground can also be found at lower altitudes, therefore increasing the chance of misclassifications. Since the *detritus* covered areas located at lower altitudes only constitute a small part of the whole area, there will be fewer pixels wrongly classified as *wet* than would be expected based on the total area of *detritus* pixels classified as wet snow. The same applies for Switzerland's areas covered by *bedrock*, even though the altitudinal distribution of those areas is more widespread, with about 25% of the pixels at elevations below 2 000 (see figure 6.4a on the next page), thus possibly resulting in a minor underrepresentation of misclassified pixels.

Even though it was possible to at least partly explain the differences in cover percentage with the first two cases, the possibility of a spurious correlation is thinkable as well. This would mean that even though we see certain similarities between the areal patterns of snow occurrence and the soil cover type, the latter is actually influenced by another external factor. In terms of soil cover, the external influencing factor could be the terrain's slope, as the occurrence of *bedrock*, *detritus*, and *glaciers* is limited to certain slope values (see figures 6.4b/6.5b/6.6b).
Due to the interdependence of the explanatory approaches and the external influencing factors as well as the limitations regarding the availability of optical reference scenes, no statements can be made to the influence of the soil cover types on the classification accuracy of wet snow using SAR.

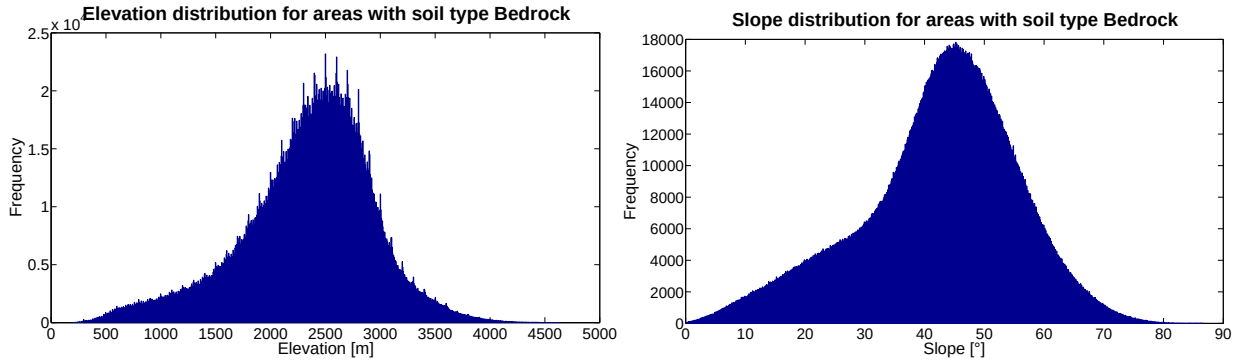

(a) Elevation distribution **(b)** Slope distribution

Figure 6.4: Distribution of elevation and slope for ground cover type bedrock in Switzerland

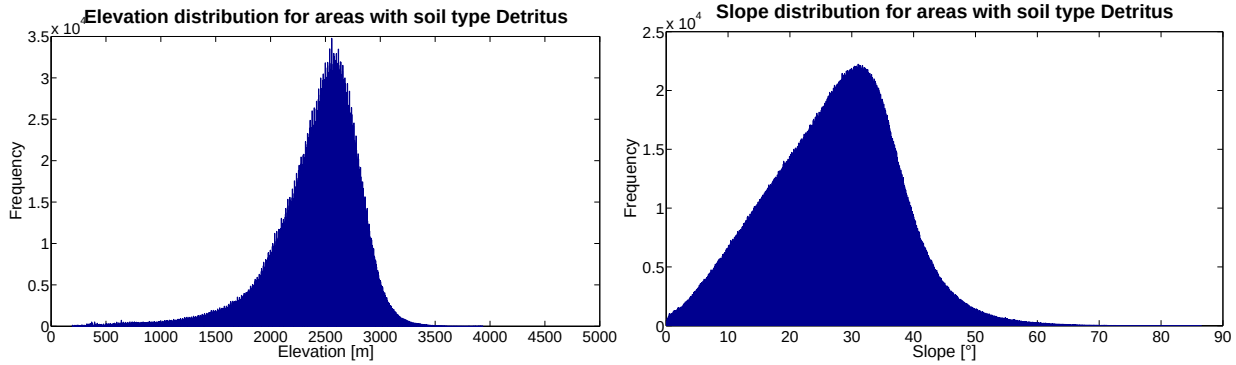

(a) Elevation distribution **(b)** Slope distribution

Figure 6.5: Distribution of elevation and slope for ground cover type detritus in Switzerland

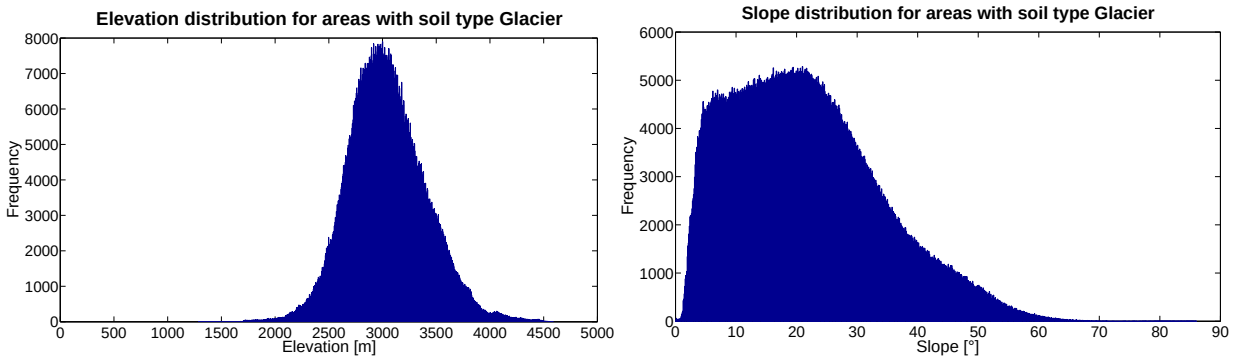

(a) Elevation distribution **(b)** Slope distribution

Figure 6.6: Distribution of elevation and slope for ground cover type glacier in Switzerland

6.1.5. Analysis of SAR wet snow mapping results in comparison to IMIS station data

The interpretation of the comparison between the SAR based snow classification and the ground reference from SNOWPACK was difficult. As presented in section 5.3 on page 60, the user's accuracy for the *snow height* parameter was very high, and relatively high for the producer's accuracy. Even though the results of these accuracy assessments in combination with the fact that the values mostly react as expected to changes in SAR footprint size and temporal baseline indicated the applicability and accuracy of the algorithm, the explanatory power was somewhat limited. First of all, the IMIS stations were selected based on their predominantly flat topography. Therefore, variations in snow cover due to topography or exposition were not reflected in the statistics. Additionally, since only the spring time melting season (1 February – 31 July) was included in the SNOWPACK data set, the occurrence of snow free conditions was limited to about 4% of all cases for comparisons against ASAR LRW composites and did not occur at all for the RS-2 image acquisitions. This restriction was particularly influencing the user's accuracy values, limiting the results to values between 96% and 100%. The producer's accuracy was not directly influenced, as its calculation was based on the about 400 snow free situations according to SNOWPACK.

For the comparison of the SAR scenes with LWC data modeled by SNOWPACK, the restrictions regarding the missing snow free conditions did not apply, as only the snow wetness was investigated. Using the 3% LWC threshold, 45% – 47% of all the snow packs for the ASAR and 82% for the RS-2 image acquisition dates were classified as *wet* based on their modeled SNOWPACK LWC. With overall accuracies of 70% and 76% the accuracy was reasonably high, showing the practicability of the wet snow detection algorithm (see figure 5.12 on page 64). Using an improved model incorporating the penetration depth of the radar waves into the snow

pack could possibly improve the accuracy of this comparison. The limitations regarding the interpretation of the accuracy values calculated for RS-2 (see section 5.3) impedes a meaningful assessment of the results.

6.1.6. Analysis of SAR wet snow mapping results in comparison to the liquid water volume (LWV)

The statistical evaluation of the comparison between SAR backscatter and LWV values derived from layered SNOWPACK data showed consistent results for both the linear regression as well as the correlation analysis. This consistency could be seen for both, variations of the temporal tolerance of the LRW calculation and the pixel area, for which the backscatter was calculated. The pattern of the results with respect to the correlation coefficient as well as a the R^2 value was as expected: smaller temporal baselines and larger pixel areas generally improved the statistical evaluations, longer temporal integration windows and smaller areas lead to a deterioration of the values. Once again, this can be explained with the mixture of different snow states when integrating multiple scenes over longer periods, and the noise reducing effect of larger areas.
The moderate, negative correlations and low R^2 values met the expectations. First of all, SAR backscatter decreases with increasing wetness of snow due to an increase of the dielectric constant (Nagler & Rott, 2000; Baghdadi et al., 1997; Woodhouse, 2006), causing a negative correlation. Secondly, due to the limited penetration depth of C-band SAR in wet snow (see section 2.1.3), only the topmost portion of the whole wet snow pack had an influence on the backscattered signal, causing variations of LWV values for a given SAR backscatter. These variations resulted in the moderately negative correlation coefficients and the low R^2 values shown in section 6.1.6. This finding regarding the negligible influence of liquid water in the lower portions of the snow pack was supported by the flat curve progression of figures 5.13–5.16 for different integration depths of wet snow layers as well as numerous scientific publications (e.g. Brogioni et al., 2006; Longépé et al., 2009).

6.2. Synthesis

While this thesis' main goal was the investigation of the relation between modeled LWC values and Envisat ASAR backscatter for a mountainous terrain like Switzerland, it was first necessary to investigate the accuracy of the wet snow detection algorithm. This algorithm, introduced by Nagler & Rott (2000) and Piesbergen et al. (1995) – even though sometimes altered to fulfill the specific requirements of authors (e.g. Besic et al. (2015)) – is still the only means to reliably detect wet snow using SAR scenes. Its reliability has been proven in numerous publications (e.g.

Malnes & Guneriussen, 2002; Hindberg et al., 2014), although predominantly for flat terrains due to the restrictions regarding geometrical distortions. To overcome these limitations, this thesis employed the LRW approach, taking advantage of the dense ASAR time series available for Switzerland in 2012. The resulting accuracies for the wet snow detection were in accordance with the scientific literature and showed the advantage of LRWs calculated from scenes with differing orbit configurations. Additionally, the dependency regarding the temporal lag for the LRW calculation could be detected as well. Regarding the external factors, this thesis did found any evidence for the direct influence of different slopes on the classification result; although it might influence the accuracy of wet snow detection due to the interdependence with underlying soil cover types. With regard to the terrain's aspect, the differences in the distribution of misclassified pixels were most probably caused by differences in the imaging geometry as well as the diurnal temperature variations, of which the former problem could be reduced significantly using overlapping scenes from different orbit configurations.
While the accordance between optical snow extent products and SAR based wet snow classifications was good, the comparison against snow height values derived from SNOWPACK was more difficult to interpret. As a result of the concentration on the spring melting season, almost no snow free reference measurements (snow height <11 cm) were available, thus dramatically reducing the range of possible user's accuracy values. For the producer's accuracy based on approximately 400 comparisons the values reached about 75% to 90%. With an overall accuracy of about 70%–75%, the comparison against LWC values derived from SNOWPACK showed a fair accordance as well.
Even though this thesis has successfully shown the applicability of the wet snow detection algorithm in mountainous terrain, the analysis found only a moderately negative correlation between the modeled wetness of the snow pack and the SAR backscatter. Given the dielectric properties of wet snow and its ramifications for the penetration depth of C-band SAR (outlined in section 2.3.2), these results are well in accordance with the theoretical expectations.

6.3. Limitations

Several limitations influenced the application or interpretation of the results. This was caused either because of limitations of the available data or on the basis of considerations regarding the integrity of the data sets.
One of the biggest uncertainties was caused by the representation of the data sets as vector and raster. For the IMIS/SNOWPACK data sets, the parameters were measured and modeled at a single point. With the spatial heterogeneity of the snow cover, this value can differ significantly over short distances due to changes in the underlying soil or the topography. Conversely, raster representations such as the remotely sensed data sets average the values over the whole

area of a pixel. This leads to an inclusion of signals from unwanted features such as lakes or anthropogenic features, causing noise in the data. This was especially true for Envisat ASAR due to its pixel spacing of 100 m, thus averaging the backscattered signal over 1 ha, and for AVHRR with a pixel area of 1 km². It is therefore difficult to accurately represent small scale features using raster cells and features with a big extent using point measurements. This was the main reason, why this thesis only used a selection of the available measurement stations, as only some had similar conditions over an extent of multiple ASAR pixels, let alone AVHRR.
A second limitation results from the fact that certain data sets used for masking were not up-to-date. As it is not possible to reliably detect wet snow cover in forested areas (Baghdadi et al., 1997; Caves et al., 1999; Piesbergen, 2001), they were masked out together with settlements, water bodies, and agricultural areas. While the latter three categories are both, slowly evolving and included in relatively recent data sets, this was not the case for the forest cover data set, therefore inducing uncertainties regarding the classification of wet snow.
Furthermore, the applicability of the wet snow detection in mountainous terrain using LRW is strongly dependent on the availability of a dense time series, if possible with both ascending and descending orbits. For the case of longer temporal lags, the signals from different snow states are mixed, causing incorrect values. Due to the requirement regarding the dense time-series, part of the analysis could only be carried out for 2012, since for the other years LRWs with a small temporal lag and big areal overlaps were not available on a regular basis. Unfortunately, caused by the loss of contact with ASAR, the peak of snow melt could not be observed for 2012. Therefore, the outcome of the analyses was heavily relying on the climatic conditions until May 2012, possibly biasing the outcome.
Another limitation of this study was the limited availability of optical snow cover extent products, especially from sensors with a high resolution such as LS 7. The small number of scenes in combination with the sometimes small areal overlap between the optical and SAR scenes resulted in only relatively few possible comparisons for the wet snow detection algorithm.
Lastly, the big differences in pixel spacing (25 m for RS-2 and 1 km for AVHRR) of the satellite products might have influenced the classification accuracy, making a meaningful comparison challenging.

6.4. Suggestions for improvement

In order to overcome the problem regarding the small number of publications allowing a comparison of the wet snow detection's user's accuracy, the areas covered with dry snow need to be estimated according to the approaches from Nagler et al. (1998), Storvold & Malnes (2004), and Storvold et al. (2006). With the application of this approach, the overall accuracy can be calculated. Since this value is reported in a variety of publications (e.g. Nagler & Rott, 2000;

Storvold & Malnes, 2004), it could then be used to assess the differences between single scene based wet snow classifications and those based on LRW composites. Since the estimation of the area covered by dry snow is adding uncertainties to the result (Storvold & Malnes, 2004; Storvold et al., 2006), this approach was not used in this thesis.
For more up-to-date data sets needed for masking, optical satellite images could be used to classify the extent of e.g. forests or water bodies. Using these data sets, the uncertainties caused by the algorithm's inability to detect snow in forested areas, could be minimized. Unfortunately, the given time frame of this thesis did not allow such a land cover classification from optical remote sensing.
In order to improve the availability of LRW composites available for wet snow detection, dense time-series as the one from 2012 are desirable. Having such frequent scenes available not only increases the accuracy of the wet snow detection, but also allows more accurate investigations regarding the starting and ending point of snow melt. Additionally, an increase in spatial resolution of both optical and radar data not only helps to better capture the spatial heterogeneity of snow and snow parameters, but also improves the comparability of point and raster based measurements.
Furthermore, the inclusion of additional optical snow cover extent data sets (especially from Landsat 7/8 or other highly resolved products) would allow additional evaluations and thus improve the interpretability of influencing factors.
Given the dense time series of 2012, the application of the algorithm proposed by Koskinen & Hallikainen (1997) might be possible, allowing to assess the detection of wet snow even in forested areas, which is of interest for snow hydrological purposes. Given the already small number of available user's accuracy values for wet snow classification in the scientific literature, the application of this algorithm would have decreased this number even further, as almost all articles mask out forested areas, therefore this approach had to be abandoned.
Lastly, the implementation of a dynamic LWC threshold, based on the layered LWC values from SNOWPACK, would more closely reflect penetration properties of the radar signal and thus potentially improve the fixed thresholding used in this study. This approach could even improve the correlation between the water content of the snow pack and the detected SAR backscatter, although a prediction of SWE or LWV values for the whole snow pack will most likely not be possible due to the constraints presented in section 6.1.6.

7. Conclusion

In this thesis, the usability of wet snow detection in mountainous regions and the influence of different external factors on the classification accuracy was analyzed. Additionally, the relation between modeled snow wetness information to C-band SAR backscatter was investigated. In this section, the research questions stated in the Introduction are answered.

1 *What different ways of retrieving snow wetness information from satellite radar data are there and how do they differ*
a) in terms of accuracy?
b) in terms of complexity?
c) in terms of inputs?

Although wet snow detection with SAR sensors using the thresholding method has been researched for well over ten years, the algorithm's basis remained the same. Some efforts were made regarding a dynamic definition of the wet snow threshold as well as improving the classification accuracy in forested areas and mountainous terrain. The biggest differences in the application of the algorithm can be seen regarding the post-processing of the input wet snow and dry reference scenes, as not all topographies perform equally well with GTC or RTC scenes, thus requiring the use of composites. This thesis showed the applicability and accuracy of the wet snow detection algorithm for the Swiss Alps using Local Resolution Weighting (LRW) composites. Therefore, a high temporal resolution of LRW input scenes is necessary to prevent a mixture of the fast changing snow conditions in the signal. Additionally, the performance of the wet snow detection algorithm is improved when calculating the LRW composite from input scenes with both, ascending and descending orbits.

2 *Which parameters influence the SAR based wet snow retrieval and what is the relative sensitivity to each?*

As outlined in section 6, the accuracy of the wet snow detection is influenced by numerous factors. Changes in the surface characteristics – often occurring in agricultural areas and on water surfaces – are known to cause misclassifications. Wet snow classification in densely forested areas is difficult, since backscattering from the trees is dominating, hindering the detection of wet snow cover of the ground. Furthermore, both, the terrain's slope and its aspect, as well as the underlying soil cover can influence the accuracy of the wet snow detection. Due to interdependencies between the different factors, the sensitivity of the classification to the factors could not be quantified.

3 Is it possible to retrieve information about the sensitivity of the SAR backscatter to snow pack based information on the locally known depth of the melting process?

Based on the statistical analysis of multiple thousand comparisons between the backscatter values from SAR LRW composites and layered LWV values derived from SLF's SNOWPACK model, only a moderate correlation could be found, unaffected of the number of pixels included from the vicinity of the station. The moderate correlation is caused by the limited penetration depth of C-band SAR with only a few centimeters even for low LWCs. Hence, only the topmost portion of the wet snow pack interacts with the radar wave, independent of the amount of liquid water in the lower portions of the snow pack. Additionally, since dry snow cannot be detected by C-band SAR, an estimation of LWV or SWE is not possible from C-band SAR alone.

8. Outlook

To improve the accuracy of wet snow classification and to expand the range of snow hydrological products, certain requirements need to be fulfilled in the future. These requirements as well as promising developments are presented in this section.
In order to diminish the uncertainties regarding the snow's state in forested areas, a refinement of the present approaches (e.g. Koskinen & Hallikainen, 1997) is necessary and should be expanded in order to include additional input data sets such as meteorological parameters and optical data sets.
Currently, multiple satellites with C-band SAR instruments have been launched or are planned to be launched within the next years. This should help to improve the availability of C-band SAR scenes and possibly allow an operational wet snow detection using LRW composites with a small temporal lag. For reasons of continuity, both, ESA and Canadian Space Agency (CSA) plan the following two C-band SAR missions

- *Sentinel-1A/B*: With Sentinel-1A, the first of the two identical, polar-orbiting satellites was launched on 3 April 2014 and is currently in the commissioning phase. With the planned launch of Sentinel-1B in 2016, the constellation will have a revisit time of six days with a resolution of 20×40 m in the extra wide swath mode (European Space Agency, 2014b,c; Malenovský et al., 2012)

- *RADARSAT Constellation*: This constellation mission is planned to be launched by the Canadian Space Agency in 2018, ensuring C-band data continuity regarding the RS-2 end of life. It consists of three satellites, resulting in a revisit time of only four days with a minimal resolution of 100×100 m and a swath width of 500 km (Canadian Space Agency, 2014).

In addition to C-band, the applicability of the wet snow detection algorithm from Nagler & Rott (2000) and Piesbergen et al. (1995) for X-band SAR was shown by e.g. Mätzler & Schanda (1984), Schellenberger et al. (2012) and Besic et al. (2015). The use of the current and upcoming satellites such as COSMO-SkyMed or TerraSAR-X might additionally help to ensure the availability of wet snow products with a high spatial and temporal resolution.
Lastly, the theoretical framework was devised for the retrieval of both, snow cover extent as well as SWE, using dual-frequency (X-/Ku-band), dual-polarization (VV/VH) SAR (Rott et al., 2011, 2012a). The algorithm was planned to be used operationally with the Cold Regions Hydrology high-resolution Observatory ($CoReH_2O$) mission within the ESA Living Planet program. Since the $CoReH_2O$ mission was finally not selected by ESA and the framework is currently not used operationally. It remains to be seen whether future missions will benefit from the preliminary work done in this field.

Acknowledgments

I would like to thank several people for their support during the development of my master's thesis. First of all, I would like to thank Dr. David Small and Dr. Tobias Jonas for their dedicated supervision and expert advice during the last year, Dr. Hendrik Wulf, Dr. Stefan Wunderle, and Dr. Fabia Hüsler for the provision of the optical reference data sets. Furthermore, I would like to express my gratitude to Dr. Daniel Henke and Daniel Kükenbrink for their valued inputs and suggestions.

Additionally, I would like to thank several institutions and agencies: The European Space Agency (ESA) for providing the Envisat ASAR time-series. Canadian Space Agency (CSA)/ MacDonald, Dettwiler and Associates Ltd. (MDA) for the provision of the RADARSAT-2 data. The WSL Institute for Snow and Avalanche Research (SLF) for the provision of the IMIS/SNOWPACK data. The National Aeronautics and Space Administration (NASA) for providing the Landsat 7 and MODIS data sets. The National Oceanic and Atmospheric Administration (NOAA) for the provision of the AVHRR data. The Federal Office of Topography (swisstopo) for providing the DHM25, swissBoundaries^{3D}, swissALTI^{3D}, SWISSIMAGE, and VECTOR25 data sets. The Federal Office of Meteorology and Climatology (MeteoSwiss) for the provision of the CLIMAP data. The European Environment Agency (EEA) for providing the CORINE data. The Federal Statistical Office (BFS) for the provision of the forest type classification (WMG1992).

Special thanks go to Annina Brügger for the statistical support, Stefanie Keiser for the inputs on and off the bike and to my fellow students, Luca Heim, Martin Schmid, and Ursina Stoll, for making the countless weekends and nights at the university bearable. Last but not least, I want to thank my parents for their support during my studies.

Bibliography

Baghdadi, N., Gauthier, Y., & Bernier, M. (1997). Capability of multitemporal ERS-1 SAR data for wet-snow mapping. *Remote Sensing of Environment*, *60*(2), 174–186. doi: 10.1016/S0034-4257(96)00180-0.

Bernier, M. (1991). *Evaluation des données d'un radar à antenne synthetique (RAS), en bandes C et X, pour la surveillance du couvert de neige*. Dissertation, Université du Québec, Québec (Canada).

Besic, N., Vasile, G., Dedieu, J.-P., Chanussot, J., & Stankovic, S. (2015). Stochastic Approach in Wet Snow Detection Using Multitemporal SAR Data. *IEEE Geoscience and Remote Sensing Letters*, *12*(2), 244–248. doi: 10.1109/LGRS.2014.2334355.

Brogioni, M., Macelloni, G., Paloscia, S., Pampaloni, P., Pettinato, S., & Santi, E. (2006). Monitoring Snow Cover Characteristics with Multifrequency Active and Passive Microwave Sensors. In *Proceedings of International Geoscience and Remote Sensing Symposium IGARSS 2006*. Denver (USA), pp. 2167–2170. doi: 10.1109/IGARSS.2006.560.

Canadian Space Agency (2014). RADARSAT Constellation.
URL http://www.asc-csa.gc.ca/eng/satellites/radarsat/, accessed 24.09.2014.

Carol, H., & Senn, U. (1950). Jura, Mittelland und Alpen: Ihr Anteil an Fläche und Bevölkerung der Schweiz. *Geographica Helvetica*, *5*(1), 129–136. doi: 10.5194/gh-5-129-1950.

Caves, R., Quegan, S., & Nagler, T. (1999). Geometric and Physical Constraints on Recovering Snow Covered Area from SAR. In *CEOS WGCV SAR Calibration & Validation Workshop*. Toulouse (France): CEOS, pp. 449–454.

Curlander, J. C., & McDonough, R. N. (1991). *Synthetic aperture radar: Systems and signal processing*. Wiley series in remote sensing. New York (USA): John Wiley & Sons.

DeWalle, D. R., & Rango, A. (2008). *Principles of snow hydrology*. Cambridge (UK) and New York (USA): Cambridge University Press.

Ehrler, C., Seidel, K., & Martinec, J. (1997). Advanced analysis of snow cover based on satellite remote sensing for the assessment of water resources. *Proceedings of the Rabat Symposium, 5th Scientific Assembly of the International Association of Hydrological Sciences*, *242*, 93–101.

Elachi, C., & van Zyl, J. (2006). *Introduction to the physics and techniques of remote sensing*. Wiley series in remote sensing. Hoboken (USA): Wiley-Interscience, 2nd ed.

European Environment Agency (2007). CLC2006 technical guidelines. doi: 10.2800/12134.
URL http://www.eea.europa.eu/publications/technical_report_2007_17/, accessed 27.07.2014.

European Space Agency (2007). ASAR Product Handbook.
URL http://earth.esa.int/pub/ESA_DOC/ENVISAT/ASAR/asar.ProductHandbook.2_2.pdf, accessed 15.07.2014.

European Space Agency (2012). ESA declares end of mission for Envisat.
URL http://www.esa.int/Our_Activities/Observing_the_Earth/Envisat/ESA_declares_end_

of_mission_for_Envisat, accessed 02.07.2014.

European Space Agency (2014a). Envisat.
URL https://earth.esa.int/web/guest/missions/esa-operational-eo-missions/envisat/, accessed 25.09.2014.

European Space Agency (2014b). Sentinel-1.
URL https://sentinel.esa.int/web/sentinel/missions/sentinel-1, accessed 24.09.2014.

European Space Agency (2014c). Sentinel-1.
URL http://www.esa.int/Our_Activities/Observing_the_Earth/Copernicus/Sentinel-1, accessed 24.09.2014.

European Space Agency (2014d). The ASAR User Guide.
URL https://earth.esa.int/handbooks/asar/CNTR1-1-2.htm, accessed 13.07.2014.

Fily, M., Dedieu, J.-P., & Surdyk, S. (1995). A SAR image study of a snow-covered area in the French Alps. *Remote Sensing of Environment*, *51*(2), 253–262. doi: 10.1016/0034-4257(94)00049-S.

Hall, D. K., Riggs, G. A., & Salomonson, V. V. S. (2006). MODIS/Terra Snow Cover Daily L3 Global 500m Grid V005.
URL http://nsidc.org/data/docs/daac/modis_v5/mod10a1_modis_terra_snow_daily_global_500m_grid.gd.html, accessed 25.09.2014.

Hiller, B., Nuebel, A., Broll, G., & Holtmeier, F.-K. (2005). Snowbeds on Silicate Rocks in the Upper Engadine (Central Alps, Switzerland)—Pedogenesis and Interactions among Soil, Vegetation, and Snow Cover. *Arctic, Antarctic, and Alpine Research*, *37*(4), 465–476. doi: 10.1657/1523-0430(2005)037[0465:SOSRIT]2.0.CO;2.

Hillman, A., Rolland, P., Periard, R., Luscombe, A., Chabot, M., Chen, C., & Martens, N. (2009). RADARSAT-2 initial system operations and performance. In *Proceedings of International Geoscience and Remote Sensing Symposium IGARSS 2009*. Cape Town (South Africa): IEEE, pp. II–753–II–756. doi: 10.1109/IGARSS.2009.5418200.

Hindberg, H., Malnes, E., & Larsen, H. E. (2014). Towards Pan-European wet snow mapping using SAR. In European Association Remote Sensing Laboratories (Ed.), *7th EARSeL workshop on Land Ice and Snow*, Bern (Switzerland).
URL http://www.earsel.org/SIG/Snow-Ice/files/oral_ws2014/Hindberg_2014_EARSeL.pdf, accessed 14.09.2014.

Hüsler, F., Jonas, T., Riffler, M., Musial, J. P., & Wunderle, S. (2014). A satellite-based snow cover climatology (1985–2011) for the European Alps derived from AVHRR data. *The Cryosphere*, *8*(1), 73–90. doi: 10.5194/tc-8-73-2014.

Jonas, T. (2012). Monitoring von Schneewasserressourcen in der Schweiz. In Swiss Federal Institute for Forest, Snow and Landscape Research (Ed.), *Forum für Wissen 2012*. Forum für Wissen 2013, pp. 7–12.

Kellndorfer, J. M., Pierce, L. E., Dobson, M. C., & Ulaby, F. T. (1998). Toward consistent regional-to-global-scale vegetation characterization using orbital SAR systems. *IEEE Transactions on*

Geoscience and Remote Sensing, *36*(5), 1396–1411. doi: 10.1109/36.718844.

König, M., Winther, J.-G., & Isaksson, E. (2001). Measuring snow and glacier ice properties from satellite. *Reviews of Geophysics*, *39*(1), 1–27. doi: 10.1029/1999RG000076.

Koskinen, J., & Hallikainen, M. T. (1997). The use of ERS-1 SAR data for snow melt detection. *Physics and Chemistry of the Earth*, *22*(3-4), 285–289. doi: 10.1016/S0079-1946(97)00145-6.

Koskinen, J., Pulliainen, J. T., & Hallikainen, M. T. (2000). Effect of snow wetness to C-band backscatter: A modeling approach. In *Proceedings of International Geoscience and Remote Sensing Symposium IGARSS 2000*. Honolulu (USA), pp. 1754–1756. doi: 10.1109/IGARSS.2000.857335.

Lehning, M., Bartelt, P., Brown, B., Fierz, C., & Satyawali, P. (2002). A physical SNOWPACK model for the Swiss avalanche warning. *Cold Regions Science and Technology*, *35*(3), 123–184.

Lehning, M., Bartelt, P., Brown, B., Russi, T., Stöckli, U., & Zimmerli, M. (1999). SNOWPACK model calculations for avalanche warning based upon a new network of weather and snow stations. *Cold Regions Science and Technology*, *30*(1–3), 145–157. doi: 10.1016/S0165-232X(99)00022-1.

Lillesand, T. M., Kiefer, R. W., & Chipman, J. W. (2008). *Remote sensing and image interpretation*. Hoboken (USA): Wiley, 6th ed.

Linlor, W. I. (1980). Permittivity and attenuation of wet snow between 4 and 12 GHz. *Journal of Applied Physics*, *51*(5), 2811–2816. doi: 10.1063/1.327947.

Loew, A., & Mauser, W. (2007). Generation of geometrically and radiometrically terrain corrected SAR image products. *Remote Sensing of Environment*, *106*(3), 337–349. doi: 10.1016/j.rse.2006.09.002.

Longépé, N., Allain, S., Ferro-Famil, L., Pottier, E., & Durand, Y. (2009). Snowpack Characterization in Mountainous Regions Using C-Band SAR Data and a Meteorological Model. *IEEE Transactions on Geoscience and Remote Sensing*, *47*(2), 406–418. doi: 10.1109/TGRS.2008.2006048.

Luojus, K., Pulliainen, J. T., Metsamaki, S., & Hallikainen, M. T. (2009). Enhanced SAR-Based Snow-Covered Area Estimation Method for Boreal Forest Zone. *IEEE Transactions on Geoscience and Remote Sensing*, *47*(3), 922–935. doi: 10.1109/TGRS.2008.2006047.

MacDonald, Dettwiler and Associates Ltd. (2011). RADARSAT-2 Product Description (Issue 1/9).
URL http://gs.mdacorporation.com/includes/documents/52-1238_RS2_Product_Description_v1-11.pdf, accessed 29.10.2013.

MacDonald, Dettwiler and Associates Ltd. (2014). RADARSAT-2: Features.
URL http://gs.mdacorporation.com/SatelliteData/Radarsat2/Features.aspx, accessed 03.07.2014.

Malenovský, Z., Rott, H., Cihlar, J., Schaepman, M. E., García-Santos, G., Fernandes, R., & Berger, M. (2012). Sentinels for science: Potential of Sentinel-1, -2, and -3 missions for scientific observations of ocean, cryosphere, and land. *Remote Sensing of Environment*, *120*, 91–101. doi: 10.1016/j.rse.2011.09.026.

Malnes, E., & Guneriussen, T. (2002). Mapping of snow covered area with Radarsat in Norway. In *IEEE International Geoscience and Remote Sensing Symposium 2002*. pp. 683–685. doi: 10.1109/IGARSS.2002.1025145.

Massonnet, D., & Souyris, J.-C. (2008). *Imaging with synthetic aperture radar*. Engineering sciences. Electrical engineering. Lausanne (Switzerland): EPFL Press, 1st ed. doi: 10.1201/9781439808139.

Mätzler, C. (1987). *Applications of the interaction of microwaves with the natural snow cover*, vol. vol. 2, issue 2 of *Remote sensing reviews*. Newark (USA): Harwood Academic Publishers.

Mätzler, C., & Schanda, E. (1984). Snow mapping with active microwave sensors. *International Journal of Remote Sensing*, *5*(2), 409–422. doi: 10.1080/01431168408948816.

Meier, E. (1989). *Geometrische Korrektur von Bildern orbitgestützter SAR-Systeme*. Dissertation, University of Zurich, Zurich (Switzerland).

MeteoSwiss (2011). MeteoSwiss Grid-Data Products: Documentation for Users. URL http://www.meteoschweiz.admin.ch/web/en/services/data_portal/gridded_datasets.Par.0006.DownloadFile.tmp/proddoc.pdf, accessed 24.09.2013.

Mitterer, C., Techel, F., Fierz, C., & Schweizer, J. (2013). An operational supporting tool for assessing wet-snow avalanche danger. In F. Naaim-Bouvet, Y. Durand, & R. Lambert (Eds.), *Proceedings of International Snow Science Workshop ISSW 2013*. Grenoble (France): ANENA, IRSTEA, Météo-France, pp. 334–338.

Nagler, T., & Rott, H. (2000). Retrieval of wet snow by means of multitemporal SAR data. *IEEE Transactions on Geoscience and Remote Sensing*, *38*(2), 754–765. doi: 10.1109/36.842004.

Nagler, T., & Rott, H. (2005). Snow classification algorithm for Envisat ASAR. In *Proceedings Envisat & ERS Symposium 2004*. Noordwijk (Netherlands): ESA, ESA SP-572.

Nagler, T., Rott, H., & Glendinning, G. (1998). SAR-based snow cover retrievals for runoff modelling. In *Proceedings of Second International Workshop on Retrieval of Bio- & Geo-physical Parameters from SAR Data for Land Applications*, Noordwijk (Netherlands): ESA, ESA SP-441.

Piesbergen, J. (2001). *ERS-1 SAR-Verarbeitungs- und Datenfusionsmethoden zur Schneekartierung im Hochgebirge*. Dissertation, University of Zurich, Zurich (Switzerland).

Piesbergen, J., Holecz, F., & Haefner, H. (1995). Snow cover monitoring using multitemporal ERS-1 SAR data. In *Proceedings of International Geoscience and Remote Sensing Symposium IGARSS 1995*. Firenze (Italy): IEEE, pp. 1750–1752. doi: 10.1109/IGARSS.1995.524015.

Piesbergen, J., Holecz, F., & Haefner, H. (1997). Multi-source snow cover monitoring in Eastern Switzerland. In *ESA ERS Symposium*. Florence (Italy): ESA, pp. 871–875. .

Reddy, M. A. (2008). *Textbook of remote sensing and geographical Information systems*. Hyderabad (India): BS Publications, 3rd ed.

Rees, G. (2006). *Remote sensing of snow and ice*. Boca Raton (USA): CRC Press.

Rosich, B., & Meadows, P. (2004). Absolute calibration of ASAR level 1 products generated with PF-ASAR.

URL https://earth.esa.int/c/document_library/get_file?folderId=38042&name=DLFE-661.pdf, accessed 16.07.2014.

Rott, H., Cline, D. W., Duguay, C., Essery, R., Etchevers, P., Hajnsek, I., Kern, M., Macelloni, G., Malnes, E., Pulliainen, J. T., & Yueh, S. H. (2011). CoReH2O, a dual frequency radar satellite for COld REgions Hydrology. In *International Geoscience and Remote Sensing Symposium IGARSS*. Vancouver (Canada): IEEE, vol. 25, pp. 2729–2732. doi: 10.1109/IGARSS.2011.6049778.

Rott, H., Cline, D. W., Duguay, C., Essery, R., Etchevers, P., Hajnsek, I., Kern, M., Macelloni, G., Malnes, E., Pulliainen, J. T., & Yueh, S. H. (2012a). CoReH2O, a dual frequency radar mission for snow and ice observations. In *Proceedings of International Geoscience and Remote Sensing Symposium IGARSS 2012*. Munich (Germany): IEEE, pp. 5550–5553. doi: 10.1109/IGARSS.2012.6352348.

Rott, H., Nagler, T., Voglmeier, K., Kern, M., Macelloni, G., & Gai, M. (2012b). Algorithm for Retrieval of Snow Mass from Ku- and X-band Radar Backscatter Measurements. In *Proceedings of International Geoscience and Remote Sensing Symposium IGARSS 2012*. Munich (Germany): IEEE, pp. 135–138. doi: 10.1109/IGARSS.2012.6350911.

Rott, H., Yueh, S. H., Cline, D. W., Duguay, C., Essery, R., Haas, C., Hélière, F., Kern, M., Macelloni, G., Malnes, E., Nagler, T., Pulliainen, J. T., Rebhan, H., & Thompson, A. (2010). Cold Regions Hydrology High-Resolution Observatory for Snow and Cold Land Processes. *Proceedings of the IEEE*, *98*(5), 752–765. doi: 10.1109/JPROC.2009.2038947.

Schaub, R. (2011). *Validation of wet snow maps from Envisat/ASAR-Data*. Master's thesis, University of Zurich, Zurich (Switzerland).

Schellenberger, T., Ventura, B., Zebisch, M., & Notarnicola, C. (2012). Wet Snow Cover Mapping Algorithm Based on Multitemporal COSMO-SkyMed X-Band SAR Images. *IEEE Journal of Selected Topics in Applied Earth Observations and Remote Sensing*, *5*(3), 1045–1053. doi: 10.1109/JSTARS.2012.2190720.

Seidel, K., & Martinec, J. (2004). *Remote sensing in snow hydrology: Runoff modelling, effect of climate change*. Springer-Praxis books in geophysical sciences. Berlin (Germany): Springer.

Shi, J., Dozier, J., & Rott, H. (1993). Deriving snow liquid water content using C-band polarimetric SAR. In *Proceedings of International Geoscience and Remote Sensing Symposium IGARSS 1993*. Tokyo (Japan): IEEE, pp. 1038–1041. doi: 10.1109/IGARSS.1993.322643.

Singh, P., & Singh, V. P. (2001). *Snow and glacier hydrology*, vol. 37 of *Water science and technology library*. Dordrecht (Netherlands): Kluwer Academic Publishers.

Small, D. (2011). Flattening Gamma: Radiometric Terrain Correction for SAR Imagery. *IEEE Transactions on Geoscience and Remote Sensing*, *49*(8), 3081–3093. doi: 10.1109/TGRS.2011.2120616.

Small, D. (2012). SAR backscatter multitemporal compositing via local resolution weighting. In *Proceedings of International Geoscience and Remote Sensing Symposium IGARSS 2012*. Munich (Germany): IEEE, pp. 4521–4524. doi: 10.1109/IGARSS.2012.6350465.

Small, D., Jehle, M., Meier, E., & Nüesch, D. (2004). Radiometric Terrain Correction Incorporating Local Antenna Gain. In *Proceedings EUSAR 2004*. pp. 929–932.

Small, D., Miranda, N., Zuberbühler, L., Schubert, A., & Meier, E. (2010). Terrain-corrected Gamma: Improved thematic land-cover retrieval for SAR with robust radiometric terrain correction. In *ESA Living Planet Symposium*. Bergen (Norway): ESA, vol. 686. .

Small, D., Schubert, A., Rosich, B., & Meier, E. (2007). Geometric and radiometric correction of ESA SAR products. In *Proceedings Envisat Symposium 2007*. Noordwijk (Netherlands): ESA, ESA SP-636. doi: 10.5167/uzh-77977.

Stebler, O., Nüesch, D., Frey, O., & Meier, E. (2008). *Einführung in die Radar-Fernerkundung*. Zurich (Switzerland): Department of Geography, University of Zurich, 3rd ed.

Stiles, W. H., & Ulaby, F. T. (1981). *Dielectric Properties of Snow: Tech. Rep. 527-1*. Lawrence (USA): Remote Sensing Laboratory, University of Kansas Center for Research.

Storvold, R., & Malnes, E. (2004). Snow covered area retrieval using ENVISAT ASAR wideswath in mountainous areas. In *Proceedings of IEEE International Geoscience and Remote Sensing Symposium 2004*. vol. 3, pp. 1845–1848. doi: 10.1109/IGARSS.2004.1370697.

Storvold, R., Malnes, E., Larsen, Y., Høgda, K. A., Hamran, S. E., Müller, K., & Langley, K. A. (2006). Sar Remote Sensing of Snow Parameters in Norwegian Areas — Current Status and Future Perspective. *Journal of Electromagnetic Waves and Applications*, *20*(13), 1751–1759. doi: 10.1163/156939306779292192.

Strozzi, T. (1996). *Backscattering measurements of snowcovers at 5.3 and 35 GHz*. Dissertation, University of Bern, Bern.

Swiss Federal Institute for Forest, Snow and Landscape Research (2013). Operational Snow-Hydrological Service.
URL http://www.wsl.ch/fe/gebirgshydrologie/schnee_hydro/oshd/index_EN, accessed 26.09.2013.

Swiss Federal Office of Topography (2004). DHM25: The digital height model of Switzerland: Product information.
URL http://www.swisstopo.admin.ch/internet/swisstopo/en/home/products/height/dhm25.parsysrelated1.44518.downloadList.76700.DownloadFile.tmp/dhm25infoen.pdf, accessed 25.09.2014.

Swiss Federal Office of Topography (2007). VECTOR25: Das digitale Landschaftsmodell der Schweiz: Produkteinformation.
URL http://www.swisstopo.admin.ch/internet/swisstopo/de/home/products/landscape/vector25.parsysrelated1.47641.downloadList.43533.DownloadFile.tmp/vector25infode.pdf, accessed 25.09.2014.

Swiss Federal Office of Topography (2010). SWISSIMAGE: Das digitale Farborthophotomosaik der Schweiz: Produktinformation.
URL http://www.swisstopo.admin.ch/internet/swisstopo/de/home/products/

images/ortho/swissimage.parsysrelated1.76752.downloadList.50684.DownloadFile.tmp/infosi201003deu.pdf, accessed 25.09.2014.

Swiss Federal Office of Topography (2013a). swissALTI3D.
URL http://www.swisstopo.admin.ch/internet/swisstopo/en/home/products/height/swissALTI3D.html, accessed 12.08.2014.

Swiss Federal Office of Topography (2013b). swissBoundaries3D: Grenzen Schweizweit in 3D: Produkteinformation.
URL http://www.swisstopo.admin.ch/internet/swisstopo/de/home/products/landscape/swissBOUNDARIES3D.parsysrelated1.18958.downloadList.85348.DownloadFile.tmp/201302sboundinfod.pdf, accessed 25.09.2014.

Swiss Federal Statistical Office (2004). Waldmischungsgrad der Schweiz.
URL http://www.bfs.admin.ch/bfs/portal/de/index/dienstleistungen/geostat/datenbeschreibung/waldmischungsgrad.parsys.0003.downloadList.00031.DownloadFile.tmp/dh404.pdf, accessed 25.09.2014.

Ulaby, F. T., Moore, R. K., & Fung, A. K. (1982). *Radar Remote Sensing and Surface Scattering and Emission Theory*, vol. 2 of *Microwave Remote Sensing: Active and Passive*. Reading (USA): Addison-Wesley.

Ulaby, F. T., Moore, R. K., & Fung, A. K. (1986). *From Theory to Applications*, vol. 3 of *Microwave Remote Sensing: Active and Passive*. Dedham (USA): Artech House.

Veitinger, J. (2010). *Methods for the derivation of snow covered area from Envisat/ASAR-Data*. Master's thesis, University of Zurich, Zurich (Switzerland).

Woodhouse, I. H. (2006). *Introduction to microwave remote sensing*. Boca Raton (USA): CRC Press.

A. Location of IMIS stations

Table A.1: IMIS station coordinates, selected stations written in bold

Abbrev.	Locality	Location	Elev. [m]	Easting [m]	Northing [m]
1ALI2	Allieres	Chenau	1 716	565 804	148 686
1CHA2	Chaussy	Pierres Fendues	2 220	578 868	136 218
1ELS2	Elsige	Elsige	2 140	615 575	153 165
1FAE2	Färmel	Muri	1 970	604 347	152 127
1FIR2	First	Schmidigen-Bidmeren	2 110	647 887	168 807
1FIS2	Fisi	Fisi	2 160	618 067	146 711
1GAD2	Gadmen	Gschletteregg	2 060	673 273	177 447
1GUT2	Guttannen	Homad	2 110	665 114	170 140
1JAU2	Jaun	Fochsen	1 716	587 469	164 670
1LAU2	Lauenen	Trüttlisbergpass	1 970	595 482	141 634
1LHO2	Lauberhorn	Russisprung	2 166	638 716	159 182
1OBM2	Ober Meiel	Gross Stand	2 110	582 680	141 181
1OTT2	Ottere	Ottere	2 020	609 436	154 275
1ROA2	Rotschalp	Schneestation	1 870	642 415	180 503
1ROA3	Rotschalp	Giebelegg	1 700	647 285	181 205
1ROA4	Rotschalp	Tanngrindel	1 838	643 573	180 626
1SCH2	Schilthorn	Schneestation	2 360	630 365	158 479
1SHE2	Sieben Hengste	Schibe	1 850	628 564	177 584
1STH2	Stockhorn	Vorderstocken	1 780	606 199	170 095
1SWM2	Lauterbrunnen	Dirlocherhorn	2 260	636 952	152 206
2MEI2	Meiental	Laucheren	2 210	685 004	177 554
2MUO2	Muotathal	Rupperslaui	2 083	699 515	199 400
2RNZ2	Rienzenstock	Rienzenstock	2 400	690 893	171 170
2SCA2	Schächental	Seewli	2 030	697 589	185 441
2SCA3	Schächental	Alpler Tor	2 330	702 186	194 253
2SCB2	Schönbüel	Bidmer	1 770	650 769	181 126
2URS2	Urseren	Giltnasen	2 170	682 404	160 067
2YBR2	Ybrig	Wannen	1 701	705 399	210 310
3AMD2	Amden	Bärenfall	1 610	729 501	225 836
3ELM2	Elm	Chüebodensee	2 050	729 279	199 679
3GLA2	Glärnisch	Guppen	1 630	721 610	206 302

Continued on next page

Table A.1 Continued: IMIS station coordinates, selected stations written in bold

Abbrev.	Locality	Location	Elev. [m]	Easting [m]	Northing [m]
3MUT2	Muttsee	Mutten	2 474	720 390	190 947
3ORT2	Ortstock	Matt	1 830	715 769	197 453
3TAM2	Taminatal	Wildsee	2 460	748 557	203 768
3TAM3	Taminatal	Schaftäli	2 170	753 893	195 303
4ANV2	Anniviers	Orzival	2 630	607 468	115 206
4ANV3	Anniviers	Tracuit	2 590	616 833	107 765
4ARO2	Arolla	Les Fontanesses	2 850	600 525	97 564
4ARO3	Arolla	Breona	2 610	609 545	103 996
4BAG1	Val de Bagnes	Col du Creblet	2 659	586 673	105 636
4BEL2	Belalp	Lengi Egga	2 556	641 190	138 305
4BOR2	Bortel	Bortelseewji	2 520	651 682	126 789
4BOV2	Boveire	Pointe de Toules	2 700	584 389	92 601
4CON2	Conthey	Etang de Trente Pas	2 230	587 328	126 495
4FNH2	Finhaut	L'Ecreuleuse	2 240	563 301	105 585
4FOU2	La Fouly	Glacier de Saleina	2 972	568 349	91 267
4FUL2	Fully	Grand Cor	2 610	573 059	115 975
4GAN2	Gandegg	Schneestation	2 717	624 748	142 043
4GOM2	Goms	Ernergalen	2 450	661 030	141 321
4GOM3	Goms	Galmihorn	2 430	660 649	148 952
4GRA2	Grammont	Loz	1 984	549 568	132 953
4ILI2	Val d'Illiez	Les Collines	2 020	552 841	115 726
4MUN2	Mund	Chiematte	2 210	637 466	131 414
4NEN2	Nendaz	Essertse	2 325	594 345	111 656
4OBW2	Oberwald	Jostsee	2 430	667 290	155 257
4OBW3	Oberwald	Mällige	2 200	670 267	151 138
4SAA2	Saas	Seetal	2 480	634 036	113 470
4SAA3	Saas	Schwarzmies	2 810	641 400	108 199
4SAA4	Saas	Gibidum	2 680	636 089	108 215
4SLFM1	SLFMiet1	Combartseline	2 204	592 000	110 148
4SPN2	Simplon	Alpjer	2 620	650 575	119 632
4SPN3	Simplon	Wenghorn	2 420	646 836	114 240
4STN2	St. Niklaus	Oberer Stelligletscher	2 910	624 090	112 974
4TRU2	Trubelboden	Schneestation	2 480	611 306	135 518

Continued on next page

Table A.1 Continued: IMIS station coordinates, selected stations written in bold

Abbrev.	Locality	Location	Elev. [m]	Easting [m]	Northing [m]
4VDS2	Vallee de la Sionne	Donin du Jour	2 390	594 522	130 017
4ZER2	Zermatt	Triftchumme	2 750	622 353	99 003
4ZER4	Zermatt	Alp Hermetje	2 380	621 261	93 900
5DAV2	Davos	Bärentälli	2 560	782 061	174 726
5DAV3	Davos	Hanengretji	2 450	778 291	184 617
5DAV4	Davos	Frauentobel	2 330	779 042	184 210
5DAV5	Davos	Grüeniberg	2 300	779 505	184 971
5ELA2	Ela	Tschitta	2 725	774 403	162 547
5ELA3	Ela	Muot	2 306	778 578	163 961
5FLU2	Flüela	Flüela Hospiz	2 390	791 582	181 009
5HTR2	Hinterrhein	Alp Piänetsch	2 150	735 434	156 310
5HTR3	Hinterrhein	Unter Surettasee	2 200	746 500	155 699
5JUL2	Julier	Vairana	2 430	773 048	149 948
5KLO2	Klosters	Madrisa	2 140	785 499	198 214
5KLO3	Klosters	Gatschiefer	2 310	790 140	190 814
5LUK2	Lukmanier	Lai Verd	2 550	703 000	162 315
5LUM2	Lumpegna	Gesamtstation	2 388	708 749	176 585
5PAR2	Parsenn	Kreuzweg	2 290	780 431	191 674
5PUZ2	Puzzetta	Schneestation	2 195	709 050	164 874
5ROT2	Rothorn	Totälpli	2 700	765 100	179 738
5SLF2	SLF	Flüelastrasse	1 560	783 879	187 447
5TUJ2	Tujetsch	Culmatsch	2 270	698 313	171 102
5TUJ3	Tujetsch	Nual	2 220	699 639	167 026
5TUM2	Tumpiv	Val Miez	2 195	720 869	182 319
5VLS2	Vals	Alp Calasa	2 070	735 200	170 779
5VMA2	Val Madris	Schwarzseen	2 530	755 780	143 191
6BED2	Bedretto	Cavanna	2 450	682 250	154 199
6BED3	Bedretto	Cassinello	2 100	683 168	149 446
6BOG2	Bosco Gurin	Hendar Furggu	2 310	679 538	131 902
6BOG3	Bosco Gurin	Pizzo Bombögn	2 179	681 070	128 855
6CAM2	Campolungo	Fontane	2 220	698 229	146 845
6DTR2	Dötra	Preda	2 060	709 714	155 619
6FRA2	Frasco	Efra	2 100	708 905	132 853

Continued on next page

Table A.1 Continued: IMIS station coordinates, selected stations written in bold

Abbrev.	Locality	Location	Elev. [m]	Easting [m]	Northing [m]
6FRA3	Frasco	Costa	2 170	706 180	134 331
6FUS2	Fusio	Alpe di Röd	2 390	690 802	143 502
6MES2	Mesocco	Pian Grand	2 380	732 362	141 747
6NAR2	Nara	Schneestation	2 070	709 823	147 852
6SIM2	Simano	Schneestation	2 450	718 448	147 401
6VAL2	Vallascia	Schneestation	2 270	690 125	155 980
7BER2	Bernina	Motta Bianco	2 450	799 122	144 311
7BER3	Bernina	Puoz Bass	2 620	790 343	146 290
7BEV2	Bever	Valetta	2 510	783 957	157 061
7KES2	Kesch	Porta d'Es-cha	2 725	788 351	166 290
7LAG2	Piz Lagrev	Schneestation	2 730	777 150	147 050
7LAG3	Piz Lagrev	Materdell	2 300	773 641	143 964
7LAV1	Lavin	Gonda-Cotschna	2 405	804 130	184 940
7OFE2	Ofenpass	Murtaröl	2 360	818 233	168 461
7SMN2	Samnaun	Ravaischer Salaas	2 520	820 670	204 666
7VIN2	Vinadi	Alpetta	2 730	828 725	202 233
7ZNZ2	Zernez	Pülschezza	2 680	797 312	175 077

B. ASAR LRW areal statistics

This page is intentionally left blank

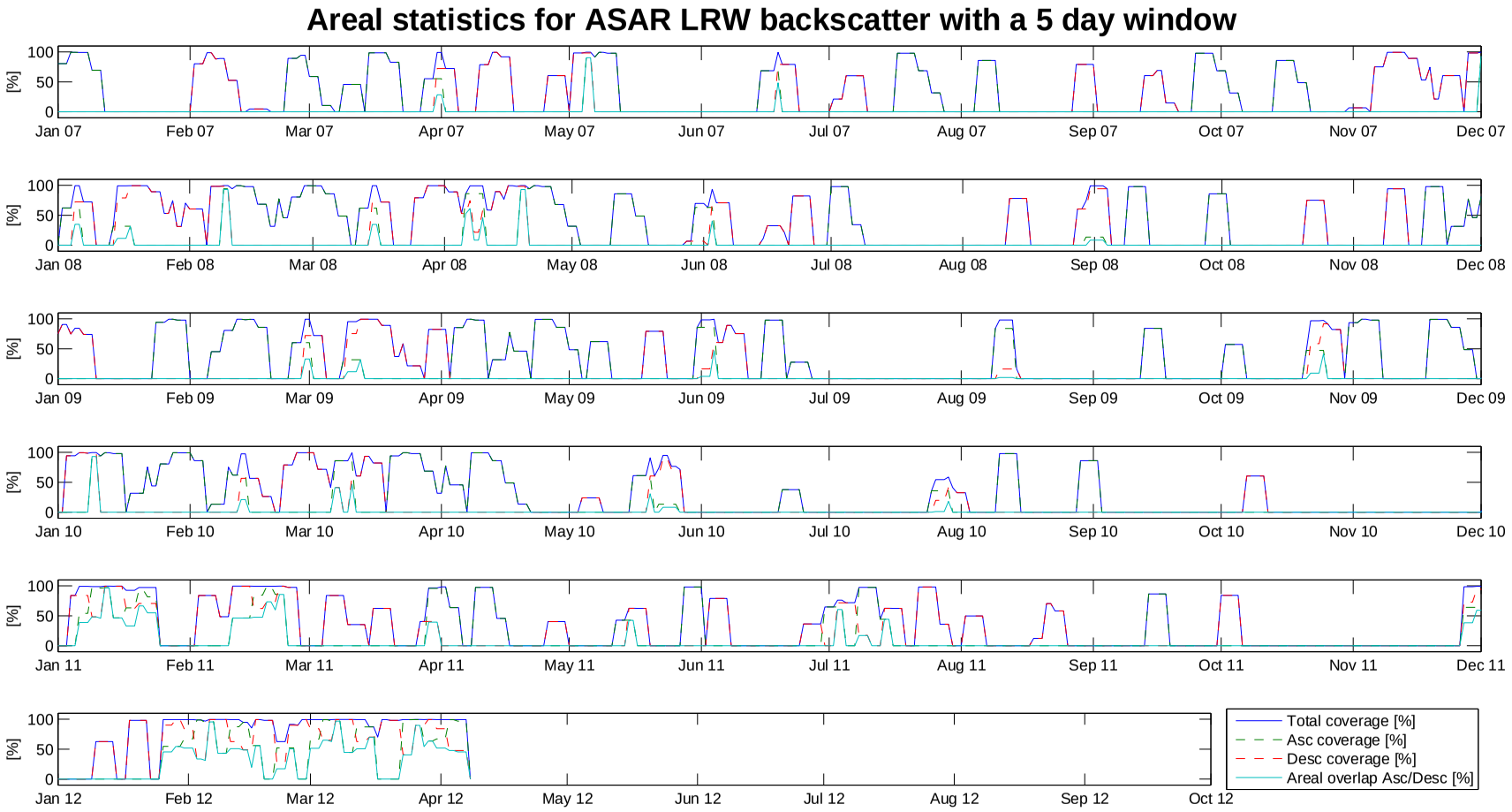

(a) 5 day search window

Figure B.1: Areal statistics for ASAR LRW composites with different temporal windows

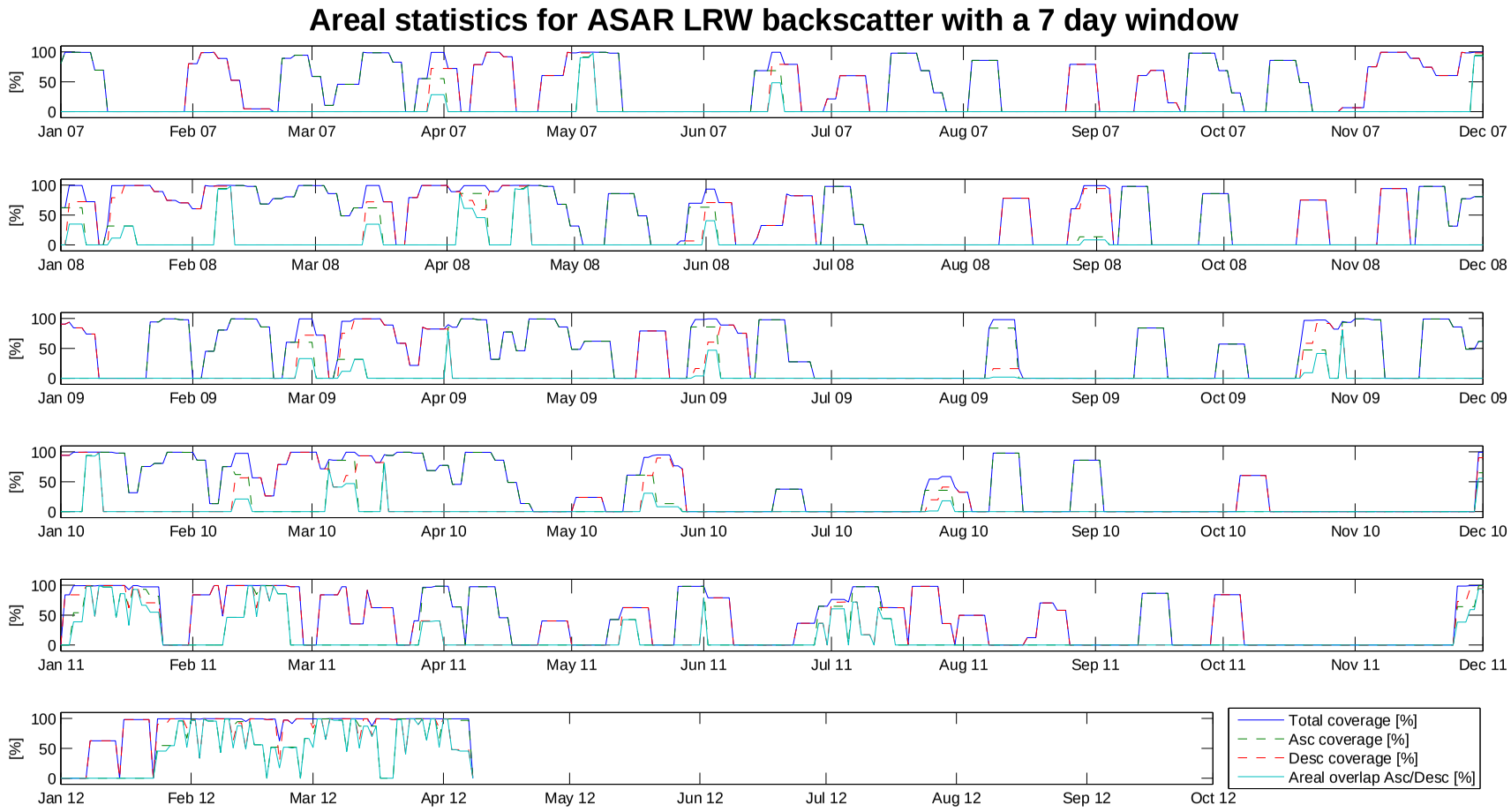

(b) 7 day search window

Figure B.1: Areal statistics for ASAR LRW composites with different temporal windows (cont.)

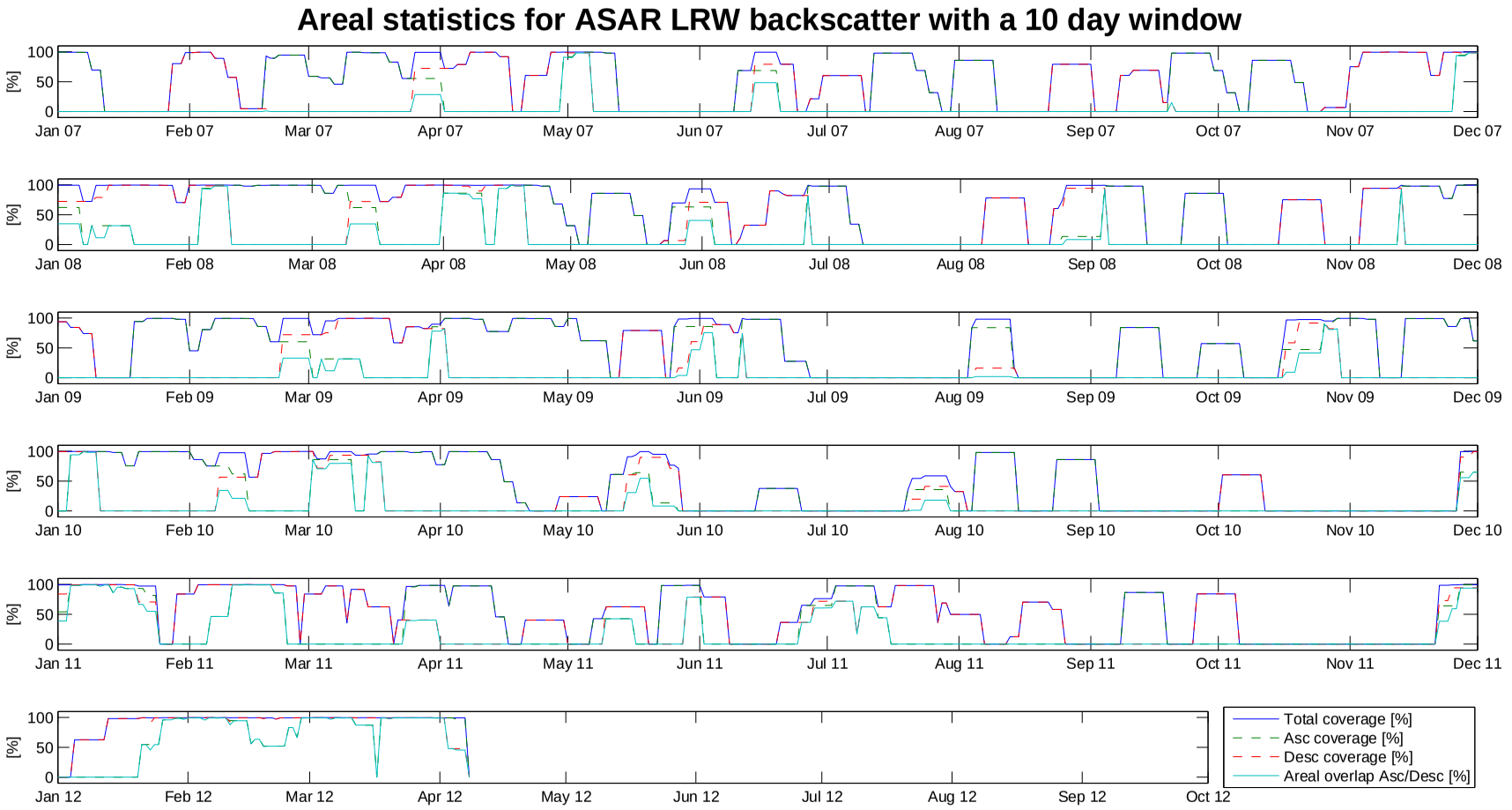

(c) 10 day search window

Figure B.1: Areal statistics for ASAR LRW composites with different temporal windows (cont.)

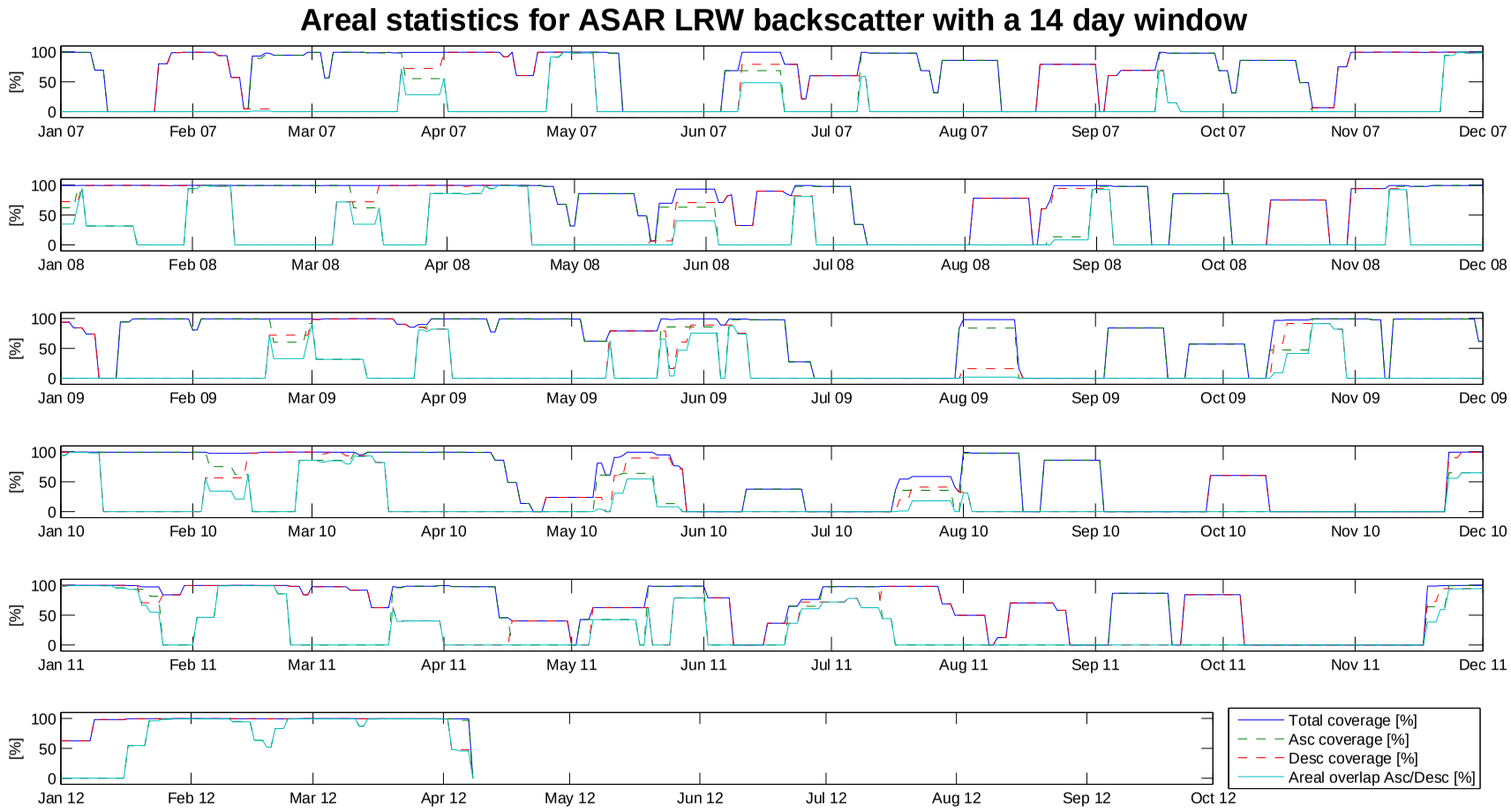

(d) 14 day search window

Figure B.1: Areal statistics for ASAR LRW composites with different temporal windows (cont.)

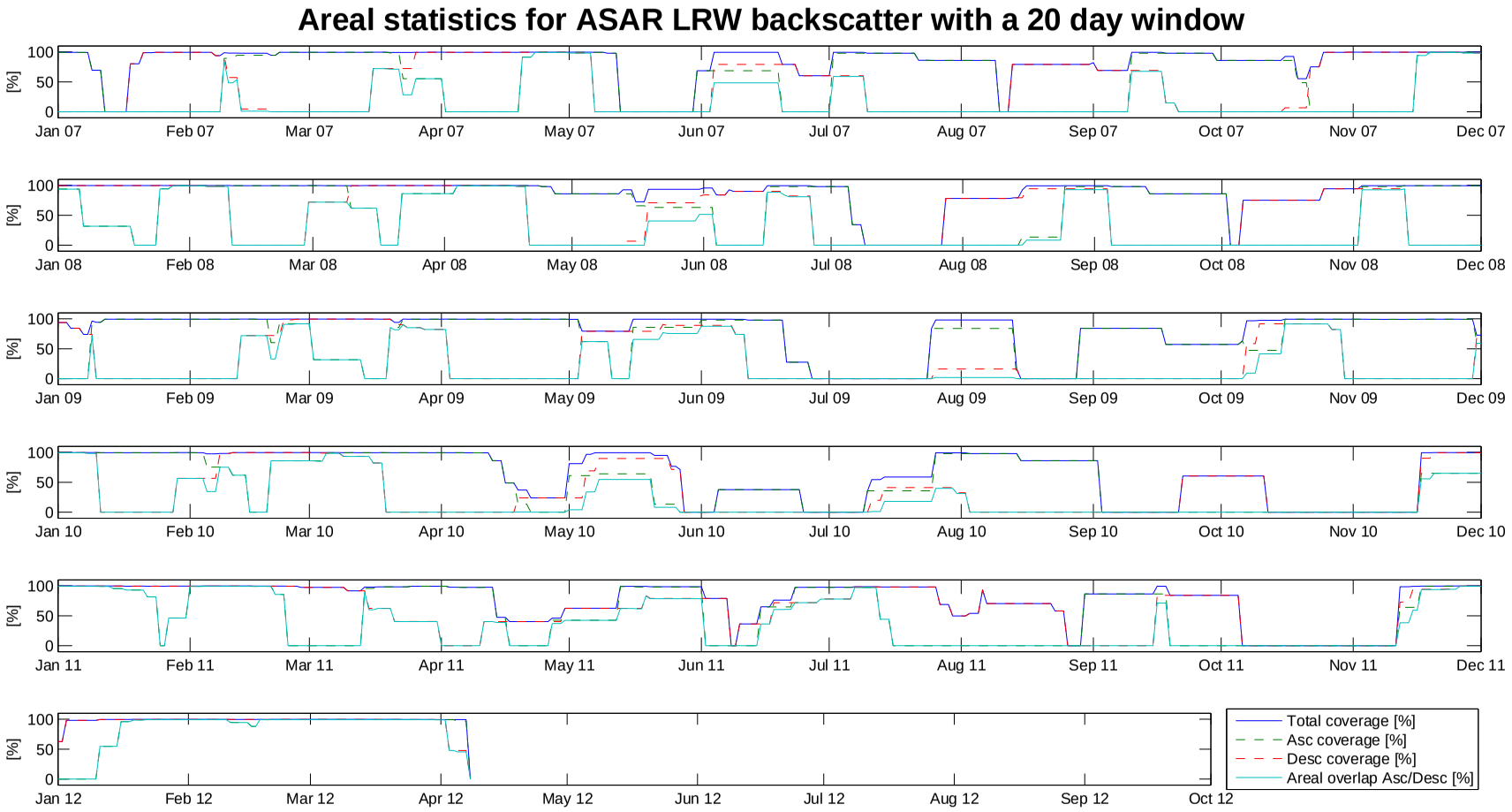

(e) 20 day search window

Figure B.1: Areal statistics for ASAR LRW composites with different temporal windows (cont.)

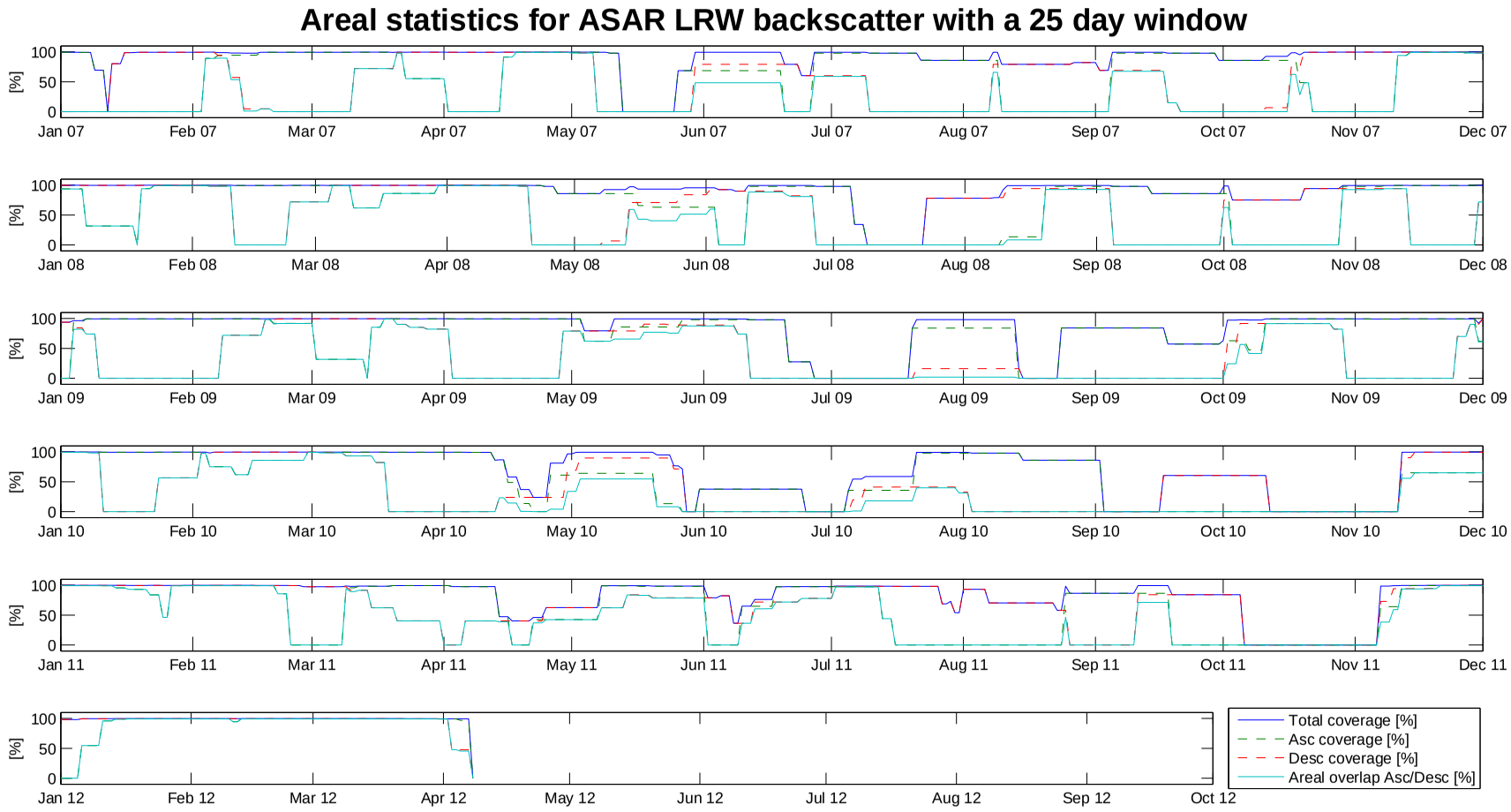

(f) 25 day search window

Figure B.1: Areal statistics for ASAR LRW composites with different temporal windows (cont.)

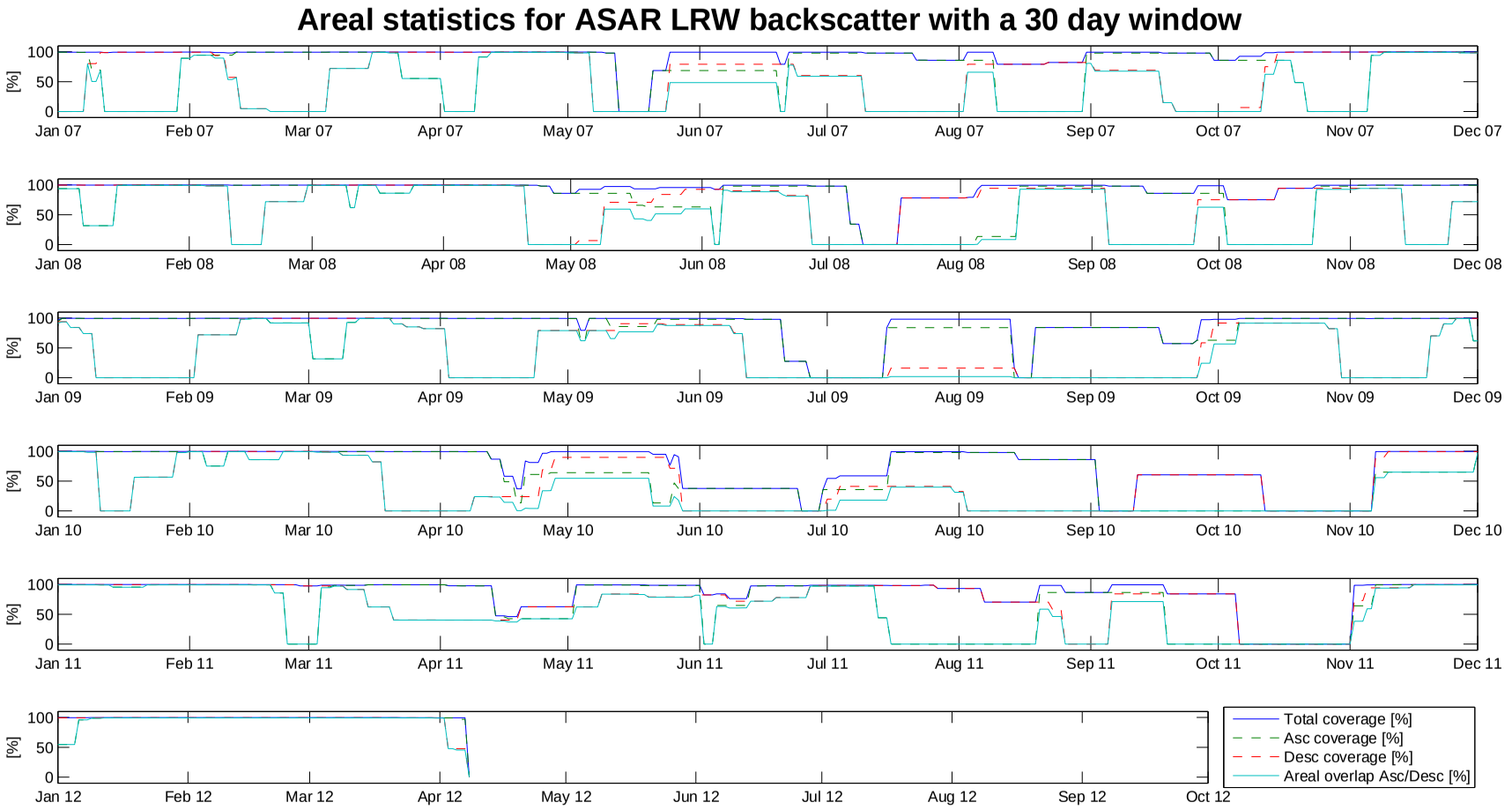

(g) 30 day search window

Figure B.1: Areal statistics for ASAR LRW composites with different temporal windows (cont.)

C. Confusion matrices

C.1. Envisat ASAR LRW wet snow classification vs. IMIS snow height

5 Day ASAR LRW (1×1 pixels) vs. Snow Height			
		SNOWPACK Snow Height (HS)	
		Snow (HS≥11cm)	No snow (HS<11cm)
ASAR	Wet Snow	1 093	24
	No wet snow	2 100	96
		User's accuracy	98.42%

(a) 1×1 pixels

5 Day ASAR LRW (3×3 pixels) vs. Snow Height			
		SNOWPACK Snow Height (HS)	
		Snow (HS≥11cm)	No snow (HS<11cm)
ASAR	Wet Snow	1 071	21
	No wet snow	2 122	99
		User's accuracy	98.08%

(b) 3×3 pixels

5 Day ASAR LRW (5×5 pixels) vs. Snow Height			
		SNOWPACK Snow Height (HS)	
		Snow (HS≥11cm)	No snow (HS<11cm)
ASAR	Wet Snow	966	17
	No wet snow	2 227	103
		User's accuracy	98.27%

(c) 5×5 pixels

5 Day ASAR LRW (7×7 pixels) vs. Snow Height			
		SNOWPACK Snow Height (HS)	
		Snow (HS≥11cm)	No snow (HS<11cm)
ASAR	Wet Snow	931	15
	No wet snow	2 262	105
		User's accuracy	98.41%

(d) 7×7 pixels

Table C.1: Assessment of 5 day ASAR LRW wet snow classification with IMIS snow height values

7 Day ASAR LRW (1×1 pixels) vs. Snow Height			
		SNOWPACK Snow Height (HS)	
		Snow (HS≥11cm)	No snow (HS<11cm)
ASAR	Wet Snow	1 591	35
	No wet snow	2 984	114
		User's accuracy	97.85%

(a) 1×1 pixels

7 Day ASAR LRW (3×3 pixels) vs. Snow Height			
		SNOWPACK Snow Height (HS)	
		Snow (HS≥11cm)	No snow (HS<11cm)
ASAR	Wet Snow	1 538	31
	No wet snow	3 037	118
		User's accuracy	98.02%

(b) 3×3 pixels

7 Day ASAR LRW (5×5 pixels) vs. Snow Height			
		SNOWPACK Snow Height (HS)	
		Snow (HS≥11cm)	No snow (HS<11cm)
ASAR	Wet Snow	1 392	23
	No wet snow	3 183	126
		User's accuracy	98.37%

(c) 5×5 pixels

7 Day ASAR LRW (7×7 pixels) vs. Snow Height			
		SNOWPACK Snow Height (HS)	
		Snow (HS≥11cm)	No snow (HS<11cm)
ASAR	Wet Snow	1 343	21
	No wet snow	3 232	128
		User's accuracy	98.46%

(d) 7×7 pixels

Table C.2: Assessment of 7 day ASAR LRW wet snow classification with IMIS snow height values

10 Day ASAR LRW (1×1 pixels) vs. Snow Height			
		SNOWPACK Snow Height (HS)	
		Snow (HS≥11cm)	No snow (HS<11cm)
ASAR	Wet Snow	2 274	61
	No wet snow	4 692	231
		User's accuracy	97.39%

(a) 1×1 pixels

10 Day ASAR LRW (3×3 pixels) vs. Snow Height			
		SNOWPACK Snow Height (HS)	
		Snow (HS≥11cm)	No snow (HS<11cm)
ASAR	Wet Snow	2 209	50
	No wet snow	4 757	242
		User's accuracy	97.79%

(b) 3×3 pixels

10 Day ASAR LRW (5×5 pixels) vs. Snow Height			
		SNOWPACK Snow Height (HS)	
		Snow (HS≥11cm)	No snow (HS<11cm)
ASAR	Wet Snow	1 997	32
	No wet snow	4 969	260
		User's accuracy	98.42%

(c) 5×5 pixels

10 Day ASAR LRW (7×7 pixels) vs. Snow Height			
		SNOWPACK Snow Height (HS)	
		Snow (HS≥11cm)	No snow (HS<11cm)
ASAR	Wet Snow	1 899	29
	No wet snow	5 067	263
		User's accuracy	98.50%

(d) 7×7 pixels

Table C.3: Assessment of 10 day ASAR LRW wet snow classification with IMIS snow height values

14 Day ASAR LRW (1×1 pixels) vs. Snow Height			
		SNOWPACK Snow Height (HS)	
		Snow (HS≥11cm)	No snow (HS<11cm)
ASAR	Wet Snow	3 287	90
	No wet snow	6 680	306
		User's accuracy	97.33%

(a) 1×1 pixels

14 Day ASAR LRW (3×3 pixels) vs. Snow Height			
		SNOWPACK Snow Height (HS)	
		Snow (HS≥11cm)	No snow (HS<11cm)
ASAR	Wet Snow	3 237	70
	No wet snow	6 730	326
		User's accuracy	97.88%

(b) 3×3 pixels

14 Day ASAR LRW (5×5 pixels) vs. Snow Height			
		SNOWPACK Snow Height (HS)	
		Snow (HS≥11cm)	No snow (HS<11cm)
ASAR	Wet Snow	2 910	52
	No wet snow	7 057	344
		User's accuracy	98.24%

(c) 5×5 pixels

14 Day ASAR LRW (7×7 pixels) vs. Snow Height			
		SNOWPACK Snow Height (HS)	
		Snow (HS≥11cm)	No snow (HS<11cm)
ASAR	Wet Snow	2 802	45
	No wet snow	7 165	351
		User's accuracy	98.42%

(d) 7×7 pixels

Table C.4: Assessment of 14 day ASAR LRW wet snow classification with IMIS snow height values

C.2. RADARSAT-2 wet snow classification vs. IMIS snow height

RS-2 (1×1 pixels) vs. Snow Height			
		SNOWPACK Snow Height (HS)	
		Snow (HS≥11cm)	No snow (HS<11cm)
RS-2	Wet Snow	37	0
	No wet snow	35	0
	User's accuracy	100.00%	

(a) 1×1 pixels

RS-2 (3×3 pixels) vs. Snow Height			
		SNOWPACK Snow Height (HS)	
		Snow (HS≥11cm)	No snow (HS<11cm)
RS-2	Wet Snow	36	0
	No wet snow	36	0
	User's accuracy	100.00%	

(b) 3×3 pixels

RS-2 (5×5 pixels) vs. Snow Height			
		SNOWPACK Snow Height (HS)	
		Snow (HS≥11cm)	No snow (HS<11cm)
RS-2	Wet Snow	36	0
	No wet snow	36	0
	User's accuracy	100.00%	

(c) 5×5 pixels

RS-2 (7×7 pixels) vs. Snow Height			
		SNOWPACK Snow Height (HS)	
		Snow (HS≥11cm)	No snow (HS<11cm)
RS-2	Wet Snow	38	0
	No wet snow	34	0
	User's accuracy	100.00%	

(d) 7×7 pixels

Table C.5: Assessment of RS-2 wet snow classification with IMIS snow height values

C.3. Envisat ASAR LRW wet snow classification vs. IMIS LWC

5 Day ASAR LRW (1×1 pixels) vs. LWC			
		SNOWPACK LWC	
		Max LWC≥3%	Avg LWC<3%
ASAR	Wet Snow	515	598
	No wet snow	367	1 803
	Overall accuracy	70.61%	

(a) 1×1 pixels

5 Day ASAR LRW (3×3 pixels) vs. LWC			
		SNOWPACK LWC	
		Max LWC≥3%	Avg LWC<3%
ASAR	Wet Snow	519	568
	No wet snow	363	1 833
	Overall accuracy	71.64%	

(b) 3×3 pixels

5 Day ASAR LRW (5×5 pixels) vs. LWC			
		SNOWPACK LWC	
		Max LWC≥3%	Avg LWC<3%
ASAR	Wet Snow	494	484
	No wet snow	388	1 917
	Overall accuracy	73.44%	

(c) 5×5 pixels

5 Day ASAR LRW (7×7 pixels) vs. LWC			
		SNOWPACK LWC	
		Max LWC≥3%	Avg LWC<3%
ASAR	Wet Snow	489	452
	No wet snow	393	1 949
	Overall accuracy	74.26%	

(d) 7×7 pixels

Table C.6: Assessment of 5 day ASAR LRW wet snow classification with IMIS LWC values

7 Day ASAR LRW (1×1 pixels) vs. LWC			
		SNOWPACK LWC	
		Max LWC≥3%	Avg LWC<3%
ASAR	Wet Snow	809	808
	No wet snow	523	2 537
	Overall accuracy	71.54%	

(a) 1×1 pixels

7 Day ASAR LRW (3×3 pixels) vs. LWC			
		SNOWPACK LWC	
		Max LWC≥3%	Avg LWC<3%
ASAR	Wet Snow	808	751
	No wet snow	524	2 594
	Overall accuracy	72.74%	

(b) 3×3 pixels

7 Day ASAR LRW (5×5 pixels) vs. LWC			
		SNOWPACK LWC	
		Max LWC≥3%	Avg LWC<3%
ASAR	Wet Snow	772	633
	No wet snow	560	2 712
	Overall accuracy	74.49%	

(c) 5×5 pixels

7 Day ASAR LRW (7×7 pixels) vs. LWC			
		SNOWPACK LWC	
		Max LWC≥3%	Avg LWC<3%
ASAR	Wet Snow	756	598
	No wet snow	576	2 747
	Overall accuracy	74.90%	

(d) 7×7 pixels

Table C.7: Assessment of 7 day ASAR LRW wet snow classification with IMIS LWC values

10 Day ASAR LRW (1×1 pixels) vs. LWC			
		SNOWPACK LWC	
		Max LWC≥3%	Avg LWC<3%
ASAR	Wet Snow	1 178	1 143
	No wet snow	823	4 042
		Overall accuracy	72.64%

(a) 1×1 pixels

10 Day ASAR LRW (3×3 pixels) vs. LWC			
		SNOWPACK LWC	
		Max LWC≥3%	Avg LWC<3%
ASAR	Wet Snow	1 162	1 083
	No wet snow	839	4 102
		Overall accuracy	73.25%

(b) 3×3 pixels

10 Day ASAR LRW (5×5 pixels) vs. LWC			
		SNOWPACK LWC	
		Max LWC≥3%	Avg LWC<3%
ASAR	Wet Snow	1 101	914
	No wet snow	900	4 271
		Overall accuracy	74.76%

(c) 5×5 pixels

10 Day ASAR LRW (7×7 pixels) vs. LWC			
		SNOWPACK LWC	
		Max LWC≥3%	Avg LWC<3%
ASAR	Wet Snow	1 059	856
	No wet snow	942	4 329
		Overall accuracy	74.98%

(d) 7×7 pixels

Table C.8: Assessment of 10 day ASAR LRW wet snow classification with IMIS LWC values

14 Day ASAR LRW (1×1 pixels) vs. LWC			
		SNOWPACK LWC	
		Max LWC≥3%	Avg LWC<3%
ASAR	Wet Snow	1 797	1 558
	No wet snow	1 169	5 735
	Overall accuracy	73.42%	

(a) 1×1 pixels

14 Day ASAR LRW (3$\times$3 pixels) vs. LWC			
		SNOWPACK LWC	
		Max LWC≥3%	Avg LWC<3%
ASAR	Wet Snow	1 784	1 508
	No wet snow	1 182	5 785
	Overall accuracy	73.78%	

(b) 3×3 pixels

14 Day ASAR LRW (5×5 pixels) vs. LWC			
		SNOWPACK LWC	
		Max LWC≥3%	Avg LWC<3%
ASAR	Wet Snow	1 677	1 268
	No wet snow	1 289	6 025
	Overall accuracy	75.08%	

(c) 5×5 pixels

14 Day ASAR LRW (7×7 pixels) vs. LWC			
		SNOWPACK LWC	
		Max LWC≥3%	Avg LWC<3%
ASAR	Wet Snow	1 646	1 185
	No wet snow	1 320	6 108
	Overall accuracy	75.58%	

(d) 7×7 pixels

Table C.9: Assessment of 14 day ASAR LRW wet snow classification with IMIS LWC values

C.4. RADARSAT-2 wet snow classification vs. IMIS LWC

RS-2 (1×1 pixels) vs. LWC			
		SNOWPACK LWC	
		Max LWC≥3%	Avg LWC<3%
RS-2	Wet Snow	37	0
	No wet snow	22	13
		Overall accuracy	69.44%

(a) 1×1 pixels

RS-2 (3×3 pixels) vs. LWC			
		SNOWPACK LWC	
		Max LWC≥3%	Avg LWC<3%
RS-2	Wet Snow	36	0
	No wet snow	23	13
		Overall accuracy	68.06%

(b) 3×3 pixels

RS-2 (5×5 pixels) vs. LWC			
		SNOWPACK LWC	
		Max LWC≥3%	Avg LWC<3%
RS-2	Wet Snow	35	1
	No wet snow	24	12
		Overall accuracy	65.28%

(c) 5×5 pixels

RS-2 (7×7 pixels) vs. LWC			
		SNOWPACK LWC	
		Max LWC≥3%	Avg LWC<3%
RS-2	Wet Snow	38	0
	No wet snow	21	13
		Overall accuracy	70.83%

(d) 7×7 pixels

Table C.10: Assessment of RS-2 wet snow classification with IMIS LWC values

D. Statistical analysis plots

Envisat ASAR LRW

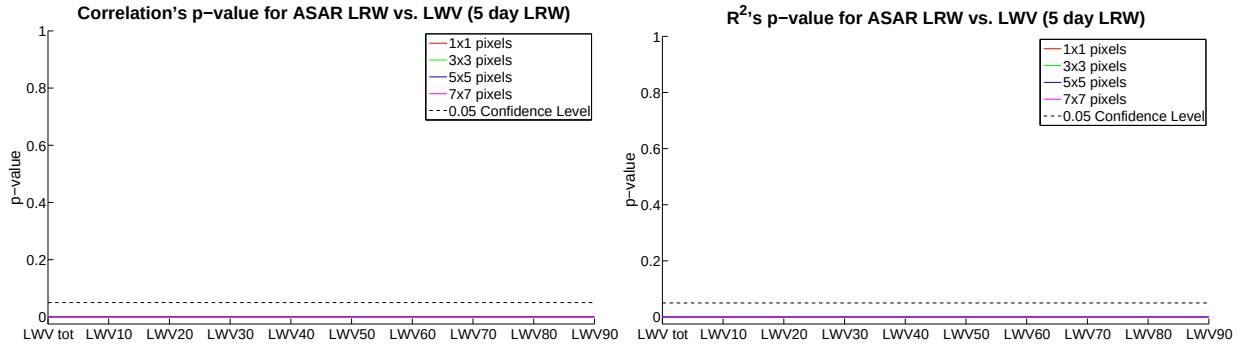

(a) p-values for Spearman's Rho **(b)** p-values for R²

Figure D.1: 5 day ASAR LRW vs. LWV

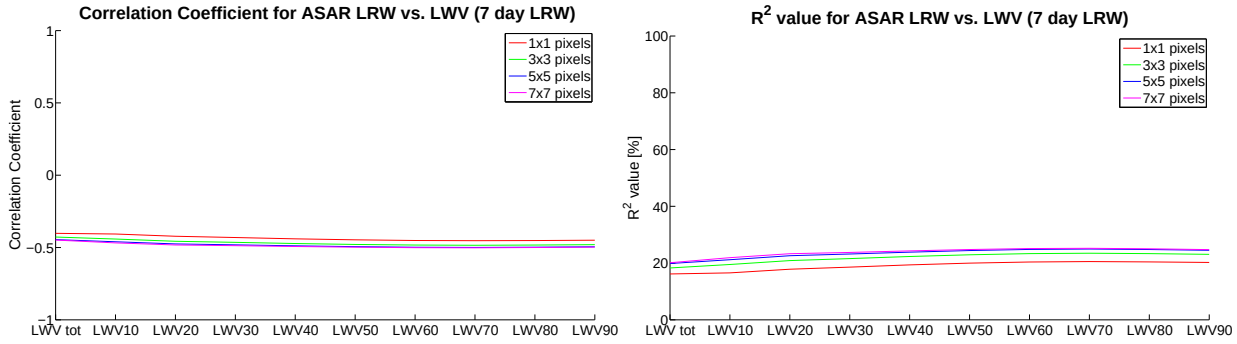

(a) Spearman's Rho **(b)** R² values

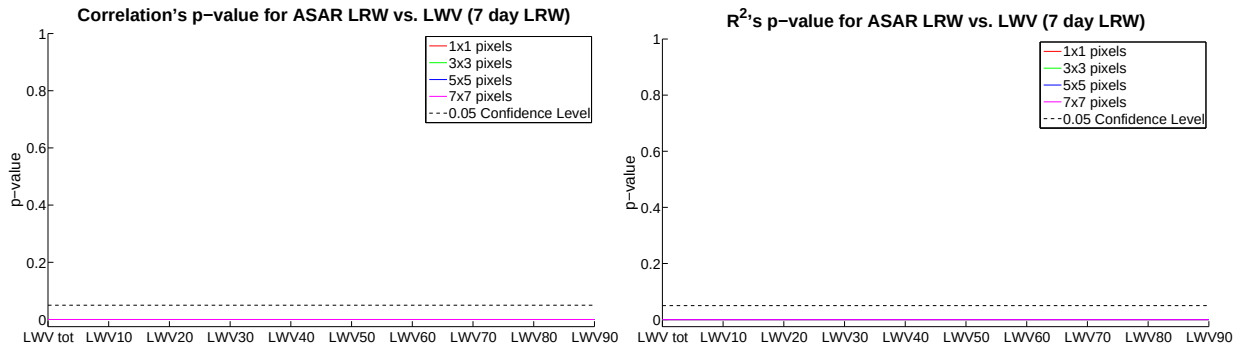

(c) p-values for Spearman's Rho **(d)** p-values for R²

Figure D.2: 7 day ASAR LRW vs. LWV

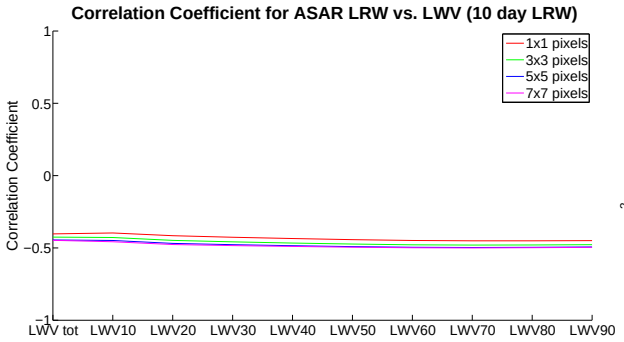

(a) Spearman's Rho

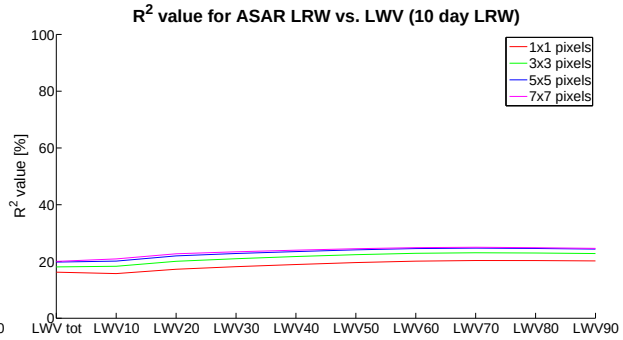

(b) R² values

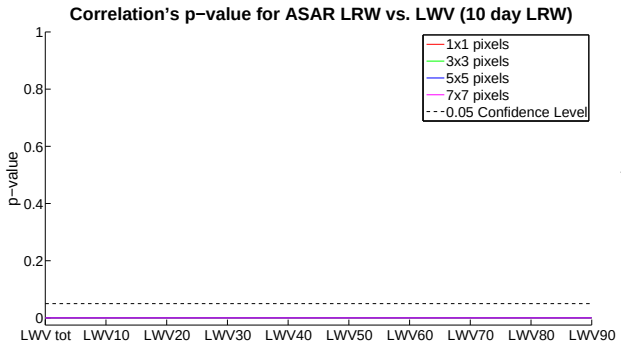

(c) p-values for Spearman's Rho

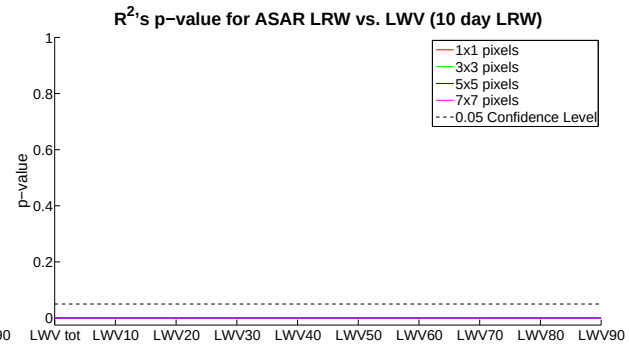

(d) p-values for R²

Figure D.3: 10 day ASAR LRW vs. LWV

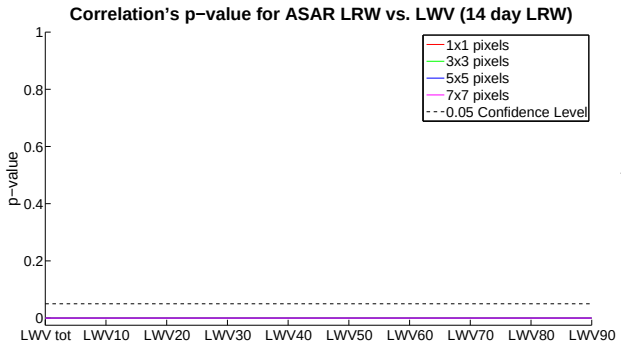

(a) p-values for Spearman's Rho

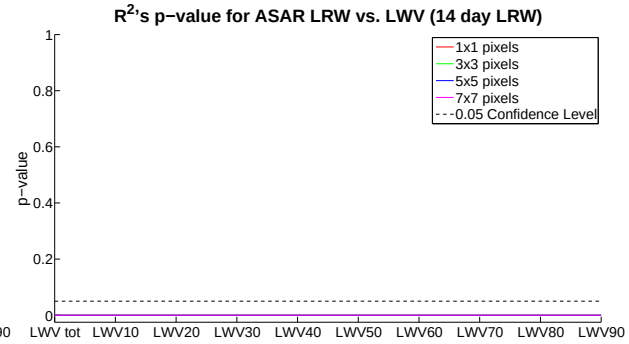

(b) p-values for R²

Figure D.4: 14 day ASAR LRW vs. LWV

RS-2

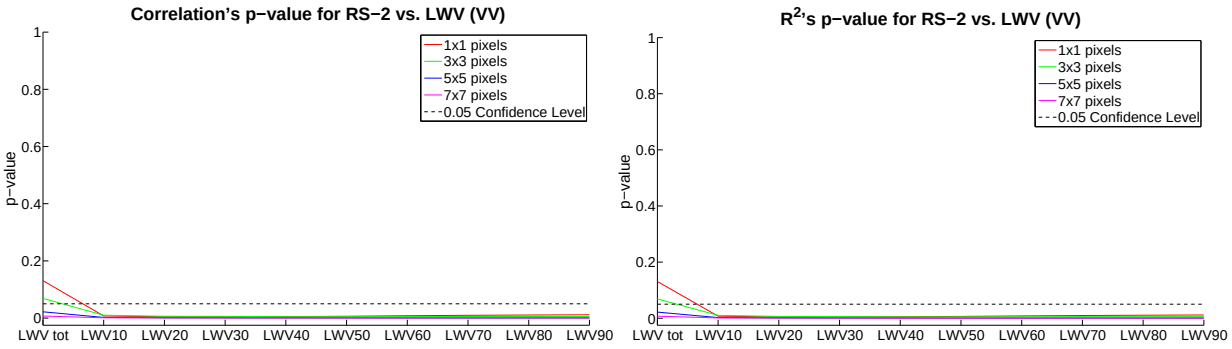

(a) p-values for Spearman's Rho **(b)** p-values for R^2

Figure D.5: RS-2 (VV) vs. LWV

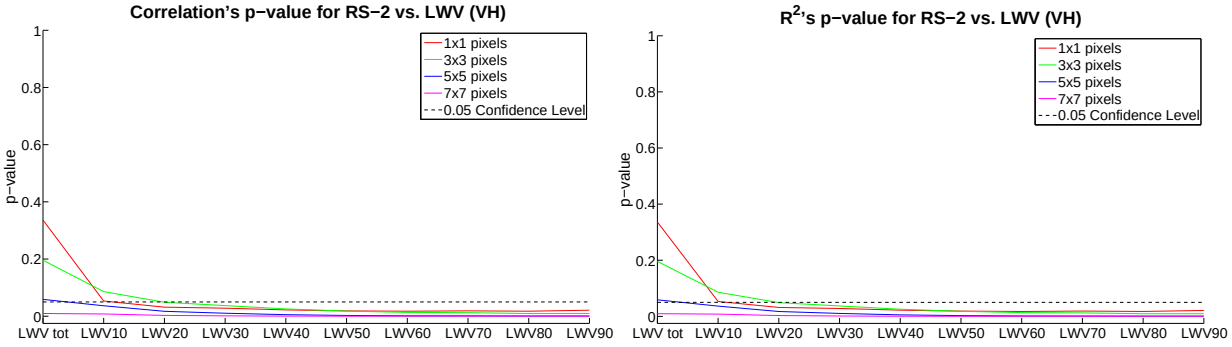

(a) p-values for Spearman's Rho **(b)** p-values for R^2

Figure D.6: RS-2 (VH) vs. LWV

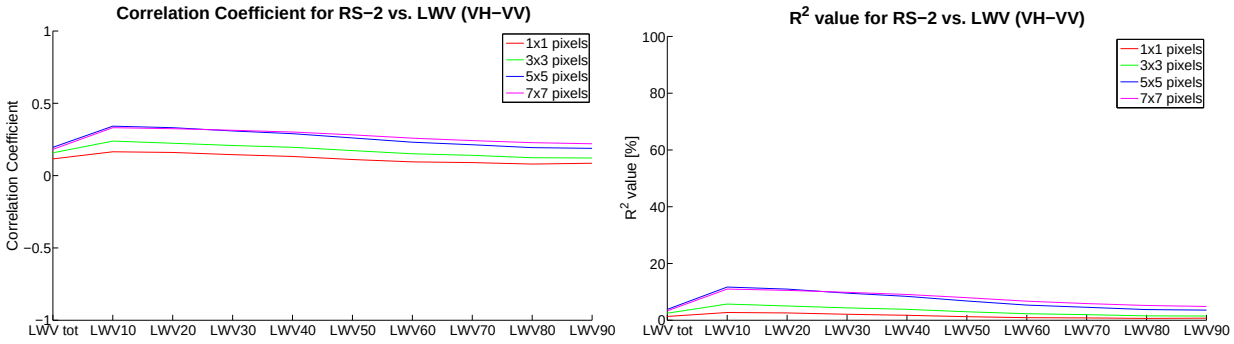

(a) Spearman's Rho **(b)** R² values

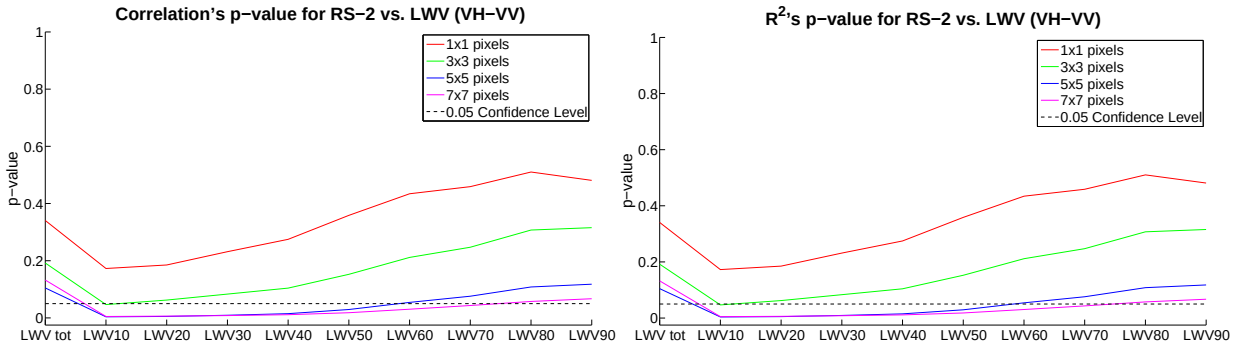

(c) p-values for Spearman's Rho **(d)** p-values for R²

Figure D.7: RS-2 (VH-VV) vs. LWV

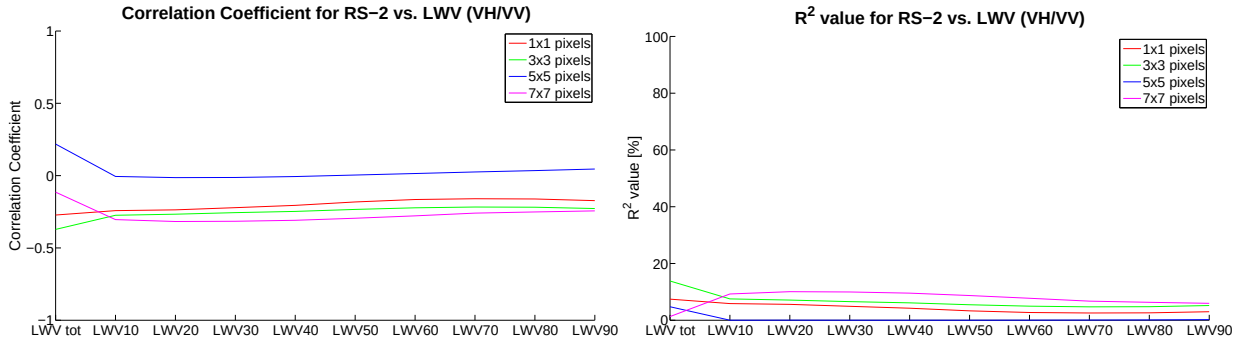

(a) Spearman's Rho

(b) R² values

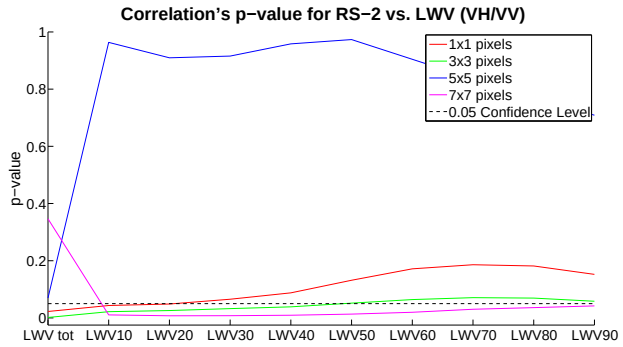

(c) p-values for Spearman's Rho

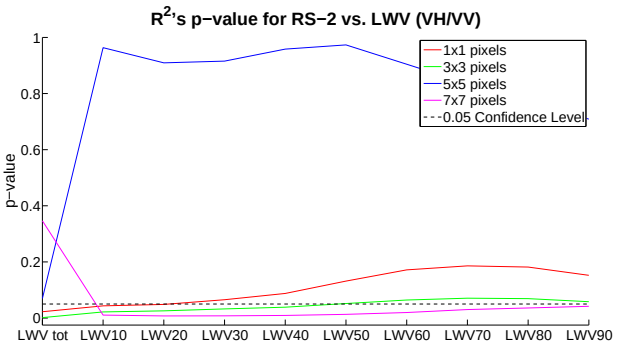

(d) p-values for R²

Figure D.8: RS-2 (VH/VV) vs. LWV

E. Declaration of Originality

Personal declaration: I hereby declare that the submitted thesis is the result of my own, independent work. All external sources are explicitly acknowledged in the thesis.

_____

Date, Place

_____

Signatory